ABSTRACT

Title of Dissertation:	DEVELOPMENT OF SINGLE-CELL MASS SPECTROMETRY TOOLS TO INVESTIGATE METABOLIC REORGANIZATION DURING EARLY EMBRYOGENESIS
	Erika Paola Portero, Doctor of Philosophy, 2020
Dissertation directed by:	Dr. Peter Nemes, Department of Chemistry and Biochemistry

Measurement of metabolism in single cells holds the potential to advance our understanding of fundamental biological processes during cell differentiation and development. However, to characterize the metabolic state of single cells, further technological advances are still required. This dissertation discusses the development and application of single-cell mass spectrometry (MS) technologies to investigate metabolism and its role during tissue induction in the early developing vertebrate (frog) embryo. The work presented herein illustrates the strategies devised to advance single-cell analysis using capillary electrophoresis (CE)-MS. Additionally, this work features several contributions to our understanding of cell heterogeneity and the role of small molecules during tissue specification in the vertebrate embryo, providing new information to advance cell and developmental biology.

Chapter 1 overviews the current state of metabolomics for cell and developmental biology, as well as the research significance and motivations.

Chapter 2 describes the fundamental concepts of CE and the current state of single-cell metabolomics by CE-MS. This chapter also discusses the development of a minimally invasive microprobe sampling technique designed for the *Xenopus laevis* embryo.

Chapter 3 presents the development of a CE-MS approach that enables dual cationic and anionic analysis of metabolites from the same single embryonic cell to deepen the detectable coverage of metabolism.

Chapter 4 discusses a stable-isotope labeling strategy and single-cell CE-MS to uncover metabolic pathways involved in cell differentiation.

Chapter 5 details the application of our custom-built microprobe sampling technique to investigate spatial cell heterogeneity in the same vertebrate embryo. This chapter examines cell-to-cell communication and small molecule transport between adjacent cells. Moreover, dual-fluorescent cell lineage tracing reveals cell fate changes induced by small molecule transport.

Chapter 6 summarizes the results generated from this dissertation work and reflects on technical challenges and potential advancements needed to drive the field of MS-based single-cell metabolomics forward.

DEVELOPMENT OF SINGLE-CELL MASS SPECTROMETRY TOOLS TO INVESTIGATE METABOLIC REORGANIZATION DURING EARLY EMBRYOGENESIS

by

Erika Paola Portero

Dissertation submitted to the Faculty of the Graduate School of the
University of Maryland, College Park, in partial fulfillment
of the requirements for the degree of
Doctor of Philosophy
2020

Advisory Committee:
Associate Professor Peter Nemes, Chair
Professor Lisa A. Taneyhill, Dean's Representative
Distinguished University Professor Catherine Fenselau
Professor Lai-Xi Wang
Professor Neil V. Blough

Acknowledgements

I would like to express my immense appreciation and gratitude to my academic advisor, Prof. Peter Nemes, for allowing me to join his research group. I am very grateful for the experience and knowledge I gained under his mentorship. Thank you for your patience, for teaching me how to formulate scientific questions, and most importantly, for sharing your love and passion for science. Your continuous support and guidance has shaped me into a better individual, leader, and scientist.

I would like to express my gratitude to Prof. Lisa Taneyhill, Prof. Catherine Fenselau, Prof. Lai-Xi Wang, and Prof. Neil Blough for serving on my dissertation committee. I am also grateful to Prof. Sally Moody for imparting her knowledge and passion for cell and developmental biology, as well as her fondness for *Xenopus laevis*.

I am very thankful to past and current members of the Nemes lab, for sharing many meaningful conversations, memories, and plenty of snacks during group meetings. Many thanks to Dr. Camille Lombard-Banek, Sam Choi, Aparna Baxi, Vi Quach, Jie Li, Aleena Andrews, Leena Pade, Steven Woolford, and Nelson Pinto for taking the time to review my abstracts, sharing your feedback, and your patience during countless presentation rehearsals. I am profoundly thankful to Dr. Rosemary Onjiko, with whom I share a great friendship and many fruitful collaborations. Thank you for your mentorship, patience, and encouraging words over the years. I would also like to thank Prof. Efrain Rodriguez, Diane Canter, and Melanna Mills from the Chemistry and Biochemistry Department at the University of Maryland for helping me navigate the administrative path towards graduation.

I am forever thankful to my family and close friends for their constant love and support during this journey. To my parents, Edgar and Elizabeth, thank you for the unconditional love, encouragement, and sacrifice. I dedicate the following to you: “Soñábamos, pero nunca imaginé que la vida me iba a llevar tan lejos. Nunca llegué a soñar todo lo que me iba a pasar en la vida”. To my brother, Efrain “Matt”, thank you for being a source of inspiration and my lifetime role model. To Diana De Leon and Marc Porter, thank you for bringing joy to my life when it was much needed. My sincere gratitude to my best friend, my partner, Bryan Medina, who was my support system and source of strength through the hard times. Thank you for always cheering me on, for sharing many adventures with me and our beloved pets Doraemon and Moe, and supporting me unconditionally. I am also thankful to Jenny Portero for always believing in my ability to succeed and for supporting me from the very beginning. To my close friends Dr. Diana Ainembabazi and Jonnestor Mojica, thank you for the countless nights of counsel and advice. Finally, many thanks to the women who mentored and urged me to pursue this degree: Mrs. Nadia Makar and Dr. Mary-Ann Pearsall. Thank you both for helping me realize that a young lady from Ecuador can also dream and achieve big goals.

I am grateful to the funding sources that supported this work and myself over the past several years: The National Institutes of Health (award no. 7R03CA211635), the National Science Foundation (award no. IOS-1832968), the Dupont Young Professor award, and the Cosmos Club Foundation Scholar Grant.

Table of Contents

List of Tables

Chapter 3

Chapter 4

Chapter 5

List of Figures

Chapter 1

Chapter 2

Chapter 3

Chapter 4

Chapter 5

List of Abbreviations

CE	Capillary electrophoresis
CID	Collision-induced dissociation
D11	Dorsal-animal midline
EIC	Extracted ion chromatogram
EOF	Electroosmotic flow
ESI	Electrospray ionization
FD	Fluorescent dye
GFP	Green fluorescent protein
GJC	Gap junctional communication
GC	Gas chromatography
IM	Ion mobility
LC	Liquid chromatography
MBT	Midblastula transition
Met	Methionine
Met*	$^{13}C_5$,^{15}N-L-methionine
MS	Mass spectrometry
m/z	Mass-to-charge ratio
TOF	Time-of-flight
Thr	Threonine
Thr*	$^{13}C_4$,^{15}N-L-threonine
RFP	Red fluorescent protein
V11	Ventral-animal midline
X. laevis	*Xenopus laevis*

Chapter 1: Introduction

1.1 Single-cell multi-omics

Detection of all the molecules (multi-omics) in single cells promises to revolutionize our understanding of complex biochemical events in the cell. A cell's state is affected by downstream processes of its genome, transcriptome, proteome, and metabolome, thus yielding a vast molecular complexity that is yet to be uncovered. For instance, the human genome contains ~20,300 protein-coding genes,[1] which produce ~20,000 proteins spanning a 7–10 log-order concentration range.[2] The Human Metabolome Database[3] currently reports ~114,200 small molecules with concentrations covering a similar broad dynamic range, which corresponds to only a small fraction of the total metabolites present in the cell. With the technological advances developed in the last decade, genome-scale molecular information at the resolution of single cells has yielded unprecedented power for systematic investigation of cellular heterogeneity in DNA,[4-6] RNA,[7-8] proteins,[9-11] and metabolites.[12-14]

Single-cell sequencing technologies recently enabled the direct sequencing of DNA and RNA under the same experimental conditions generating an unbiased readout of the cell's genotype and phenotype. For example, using parallel DNA-mRNA (or DR-seq),[15] the DNA and mRNA material of single mouse embryonic stem cells was amplified without physically separating the nucleic acids before amplification, yielding lower sample losses. The application of DR-seq also detected variations in DNA copy numbers and transcript counts, suggesting that copy number

variations may drive variability in gene expression among individual cells. Additionally, advances in single-cell transcriptomics using microfluidic devices[7, 16] have improved measurement throughput by enabling the barcoding and detection of 4,000–12,000 individual cells per hour. Although the genome and transcriptome of a cell captures valuable information regarding the cell's state, much of the function of the cell is determined by their downstream products.[17]

The single-cell proteome and metabolome provide complementary information into the cell's molecular state. Characterization of the cell's proteome and metabolome promises to deepen our understanding of cellular behaviors and phenotypic identities.[18] However, without molecular amplification of the entire proteome and metabolome, it has been technologically challenging to characterize molecular events downstream of gene transcription with adequate molecular coverage, sensitivity, or scalability. Currently, mass spectrometry (MS) is the technology of choice for the detection of proteins in single cells. By developing a custom-built capillary electrophoresis (CE)- electrospray ionization (ESI) platform, the Nemes lab was able to detect and quantify ~600–800 protein groups from ~5 ng of total protein content in live embryonic cells.[9, 19] Additionally, single-cell proteomics by MS (SCoPE-MS)[20] was able to achieve adequate ion signal for peptide sequencing and quantification in mammalian cells by combining isobaric tandem mass tags (TMT)[21] and "single-cell augmented samples" comprised of ~200 carrier cells. Overall, single-cell proteomics technologies coupled to separation-based techniques (e.g., liquid chromatography (LC), capillary electrophoresis (CE), etc.)

have enabled the analysis of protein production in single eggs,[9-10, 19] small tissues,[22] and small populations of cells[23] isolated from frog or human[24] embryos.

The metabolome is viewed as the ultimate descriptor of a cell's molecular phenotype. The metabolome amasses downstream products of intrinsic events, such as transcription, translation, and changing phases of the cell cycle, as well as extrinsic influences, including chemical, physical, and biological cues. Therefore, the single-cell metabolome provides a sensitive and effective descriptor of the cell's molecular state. Emerging single-cell MS technologies have facilitated the analysis of metabolites in a neuron,[14, 25] whole embryos,[13, 26] tissues,[27] and single-cells.[12, 28-31] However, single-cell metabolomic MS methods are faced with several analytical challenges. For example, the metabolome encompasses an extensive number of metabolites with rapid turnover rates (milliseconds–seconds), a broad concentration range, and diverse physiochemical properties. Therefore, at present there is no single approach amenable to characterize the entire suite of metabolites in the cell. Yet, single-cell metabolomics raises the potential to identify cell-to-cell expression signatures during normal or pathological processes, such as during embryogenesis. For example, small biomolecules such as folic acid,[32] coenzyme A (CoA),[33] and amino acids[12] (e.g., methionine, threonine) have been recently identified to mediate essential metabolic pathways/metabolism that regulate embryogenesis in the vertebrate *Xenopus laevis* embryo.

In what follows, I discuss the applications of MS and metabolomics for cell and developmental biology to put in perspective the work presented in this dissertation. Moreover, this chapter surveys current MS approaches for the detection

of metabolites in embryonic models, including the South African clawed frog (*Xenopus laevis*), which is the animal model used in this work. Finally, the scientific significance and motivations behind the present dissertation work are discussed.

1.2 Metabolite analysis for cell and developmental biology

1.2.1 Metabolomics by mass spectrometry

Mass spectrometry (MS) is the analytical technology of choice for detecting and quantifying metabolites due to its high sensitivity, specificity, and label-free detection. MS-based metabolomics workflows can be streamlined to deliver high reproducibility (e.g., quantitative error <5% relative standard deviation),[12] allowing for both absolute and relative quantification. Currently, two complementary approaches are used for the analysis of metabolites by MS: metabolite profiling (or targeted) and discovery (or untargeted) analysis. Metabolic profiling targets a subgroup of metabolites, which are typically related to a specific metabolic pathway. Therefore, targeted metabolomics-MS approaches are effective and routinely utilized in the discovery of therapeutic and toxicant (pollutant) biomarkers.[34] On the other hand, a discovery or untargeted metabolic analysis aims to compare metabolite composition between samples by measuring as many metabolites as possible. In general, single-cell metabolomics (targeted or untargeted) follows rigorous experimental design to ensure high-quality results. Key steps of the workflow include cell identification, isolation, detection, metabolite identification, quantification, and data interpretation (see Figure 1.1). Specific considerations for single-cell metabolomics are discussed in detail in Chapter 2.

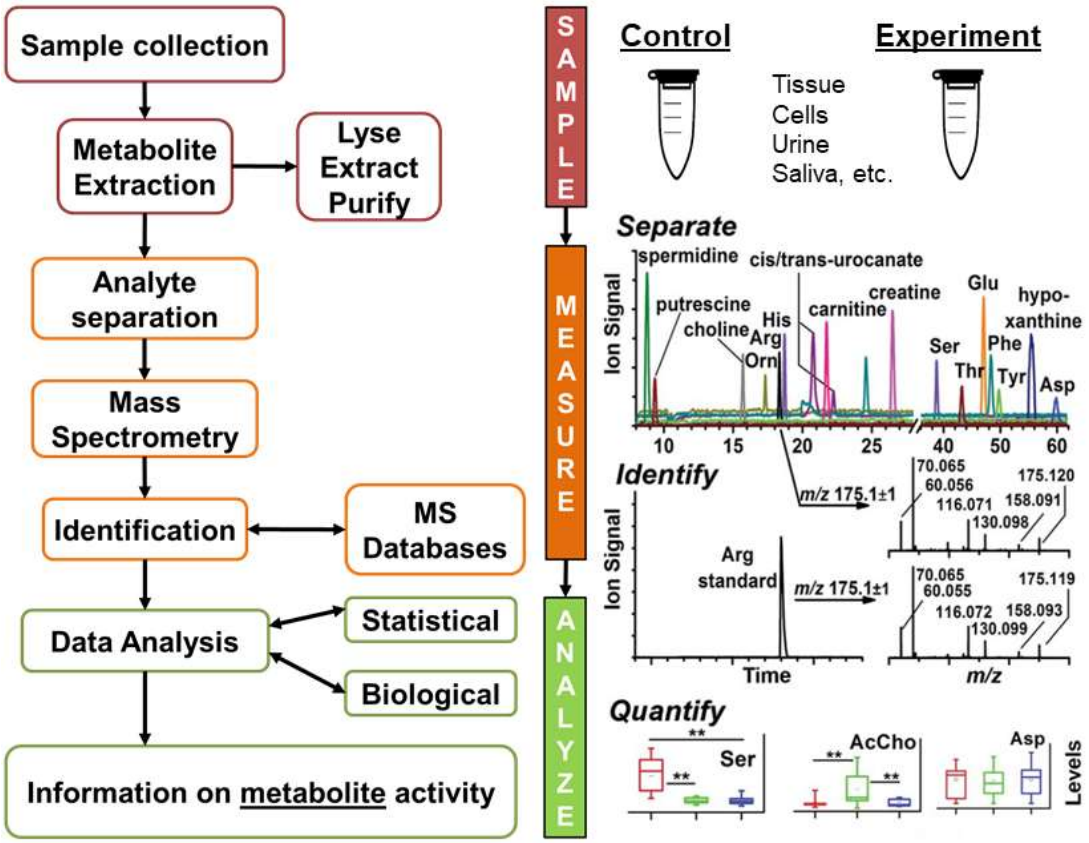

Figure 1.1 General MS-based metabolomics workflow for the detection of metabolites in biological samples. Adapted with permission from ref. 53.

To facilitate the analysis of different types of metabolites in biological samples, it is advisable to couple MS with a chemical-based separation method, such as gas chromatography (GC), LC, and CE. For example, the advantages of using GC-MS include high separation efficiency and reproducible retention times. However, a notable disadvantage of metabolomic analysis with GC-MS is the need to perform chemical derivatization (e.g., silylation[35]) to analyze polar metabolites, which limits molecular coverage. For LC-MS, a variety of methods have been developed based on the nature of the metabolites of interest. Reversed-phase (RP)-LC methods are

routinely utilized in the analysis of metabolites[36-37] and lipids.[38] Additionally, hydrophilic interaction chromatography (HILIC) methods[39-40] are preferentially used in the analysis of polar metabolites. Moreover, CE-MS is an emerging technology able to achieve high separation efficiency of metabolites from low-volume samples.[41] Another key aspect to consider when conducting metabolomics experiments is metabolite identification. A major challenge for the identification of metabolites using MS is that a single mass-to-charge ratio (*m/z*) value can yield hundreds of possible chemical compound matches. To address this concern, a set of minimum requirements for reporting chemical analysis and metabolite identifications in metabolomic studies has been recently suggested, known as the Metabolomics Standards Initiative (MSI).[42] Moreover, by combining chemical-based separation technologies, higher resolution mass spectrometers, smart "mass analysis" algorithms, and comprehensive databases (e.g., Metlin,[43] Human Metabolome Database,[3] mzCloud (https://www.mzcloud.org/), etc.), it is now possible to confidently and rapidly identify numerous metabolites via MS.

1.2.2 Metabolomics for cell and developmental biology

Recent mass spectrometry technologies have enabled the detection of hundreds of metabolites and lipids in vertebrate embryonic models, facilitating the assessment of spatial and temporal metabolic and lipidomic changes during embryonic development. For example, ambient ionization techniques[44-45] coupled to MS are capable of detecting metabolites and lipids in mouse,[46] bovine,[47] porcine,[48] zebrafish,[49] and frog[27, 50] whole embryos without prior sample preparation, providing

rapid analysis times. Chemical characterization of metabolites and lipids from mouse (Figure 1.2A) and bovine embryos using desorption electrospray ionization (DESI)-MS[46-47] resulted in a detailed annotation of metabolic and lipid profiles from oocytes and blastocysts. Additionally, metabolites and lipids from *X. laevis* frog embryos were characterized using laser ablation electrospray ionization (LAESI)-MS[50] (Figure 1.2B), which uncovered heterogeneity across the animal–vegetal axis. A total of 52 metabolites including amino acids and ~90 lipids were putatively identified and compared between the animal–vegetal poles. Recently, nanostructure initiator MS (NIMS)[51] enabled the detection of several metabolites and lipids in the mouse embryo (Figure 1.2C). By utilizing tightly focused beams of electrons, monoatomic, or polyatomic ions (e.g., C^{+}_{60} or Au^{+}_{3}) to sputter metabolites with 10–100 nm resolution, time-of-flight secondary ionization MS (TOF-SIMS)[52] uncovered heterogeneous lipid distribution in zygotes and embryos of *X. laevis* (Figure 1.2D). The high-resolution molecular images captured by TOF-SIMS show potential egg-sperm lipid fusion sites and reorganization of the membrane in the cleavage-stage embryo.[53] Laser-based ionization techniques provide information on the metabolic and lipid composition of a thin section and/or surface of the embryo.

Other analytical techniques have focused on the analysis of metabolites from whole embryos,[13] tissues,[54] and single-cells[12, 30-31, 55-56] to deepen the coverage of the metabolome. For example, liquid chromatography (LC) was employed as a separation step coupled with detection by MS to identify metabolites among pooled samples of whole *X. laevis* embryos collected at different developmental stages.[13] Furthermore, using stable-isotope labeling of metabolites to trace central metabolic pathways such

as the citric acid (Krebbs or TCA) cycle, suggested that alanine and aspartate pools serve as energy sources of the developing embryo.

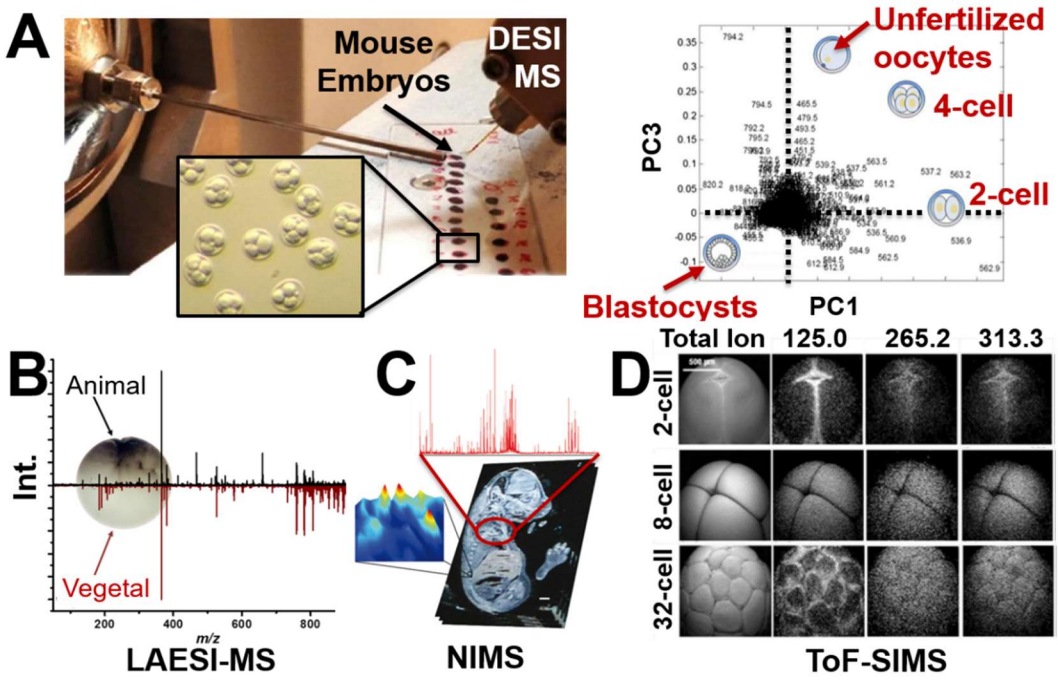

Figure 1.2 Metabolite imaging in developing embryos. (A) Desorption electrospray ionization (DESI). (B) Laser ablation electrospray ionization (LAESI). (C) Nanostructure-initiator MS (NIMS). (D) Time-of-Flight secondary ion MS. Adapted with permission from refs. 50 and 53.

CE offers several advantages for single-cell MS analysis. First, CE is amenable to small sample volumes (<1 nL), which are commonly encountered in single cells. It provides a higher number of theoretical plates as compared to partition chromatography (e.g., LC). Better resolution in separation is important because it enables the separation of metabolites from a complex biological sample. Finally, as a separation step prior to ionization and detection by MS, it provides a unique migration time value for each detected compound, becoming a useful tool for the identification of metabolites. For example, using a custom-built CE-ESI-MS

platform, our lab investigated metabolic heterogeneity among cells located in dorsal–ventral, animal–vegetal,[12] and left–right[57] developmental axes of the 8-, and 16-cell *X. laevis* embryo. About 100 molecular features with unique mass-to-charge ratio (*m/z*) and migration time were identified among 3 distinct cell types. A total of 40 metabolites were identified and combined with chemometric data analysis to determine single-cell heterogeneity across the analyzed developmental axes. An in-depth overview of CE-MS and single-cell metabolomics is presented in Chapter 2.

1.3 Research significance and motivation

To study metabolism in individual embryonic cells during early embryogenesis, the Nemes Lab uses the South African clawed frog (*Xenopus laevis*), a well-established vertebrate model for molecular, cell and developmental biology studies. This animal model offers several advantages, for example: i) embryonic cells of the *X. laevis* are considerably large during early development, which facilitates the development and validation of new bioanalytical technologies, ii) tissue fates have been carefully mapped for every embryonic cell in the 16-[58] and 32-cell[59] embryo, allowing us to test functional significance of our metabolic data on cell fate commitment, and iii) the *X. laevis* frog offers a reliable year-round supply of embryos with rapid external development that agrees with faster experimental protocols.

Recently, our lab characterized metabolites in whole *X. laevis* embryonic cells using CE-ESI-MS[12] and uncovered previously unknown single-cell heterogeneity among cells in the early developing embryo (Figure 1.3A). Comparing metabolic profiles obtained from the dorsal and ventral cell types demonstrated that each cell

has a unique metabolic profile. To test functional significance of the measured metabolite differences across the dorsal–ventral cell types, our lab conducted a series of microinjections containing a mixture of metabolite standards and a fluorescent tracer to investigate likely effects on tissue fate. Remarkably, it was found that altering the native abundance of metabolites in dorsal and ventral cells influenced their tissue fates (Fig. 1.3B). For example, when injecting the animal-dorsal D11 cell at the 16-cell embryo with a mixture of metabolites found to be enriched in the ventral V11 cell, such as acetylcholine and methionine, it was found that the neural-tissue fate of the D11 cell at the larval stage (Figure 1.3B, Top panel) was changed to an epidermal-tissue fate (Figure 1.3B, Bottom panel). However, the underlying molecular mechanisms that link metabolites and their contribution to the phenotypic changes in tissue fate observed in the *X. laevis* embryo remains unknown by us and others in the developmental biology community.

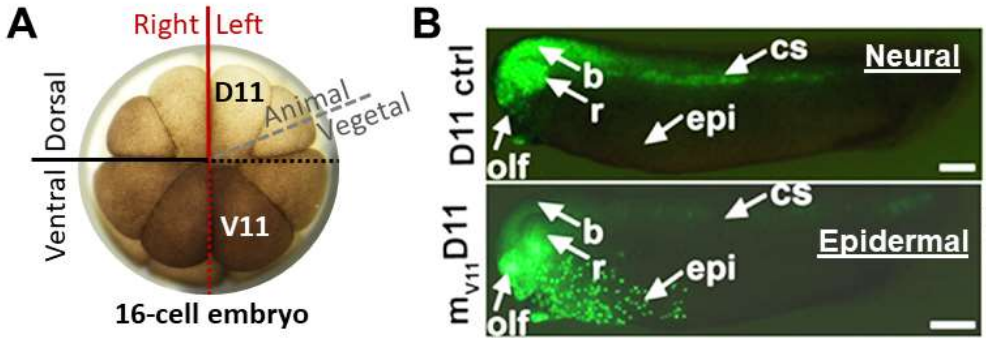

Figure 1.3 Developmental axes and cell fate lineage of the *X. laevis* embryo. Key: b–brain, r–retina, epi–epidermis, cs–central somite, olf–olfactory placode.

In this dissertation work, I developed single-cell analytical tools and applied them to expand metabolomic analysis in *X. laevis* during early embryonic development. To enable single-cell analysis, a new sampling approach to conduct *in situ*, minimally invasive sampling of the *X. laevis* embryo was devised.[55] This approach incorporates a fabricated microprobe to aspirate a small volume (~10 nL) of the cell without damaging or hindering embryonic development, which is discussed among recent technological advances in single-cell CE-MS in **Chapter 2**. Next, a custom-built CE-MS platform was adapted to enable dual analysis of cationic and anionic metabolites from single cells (**Chapter 3**). In **Chapters 4** and **5**, I utilized these technologies to study single-cell metabolic heterogeneity in the early *X. laevis* developing embryo. Finally, **Chapter 6** reflects on the current state of single-cell metabolomics with mass spectrometry, emphasizing existing challenges and emerging methodologies that are needed to continue to push the field onwards.

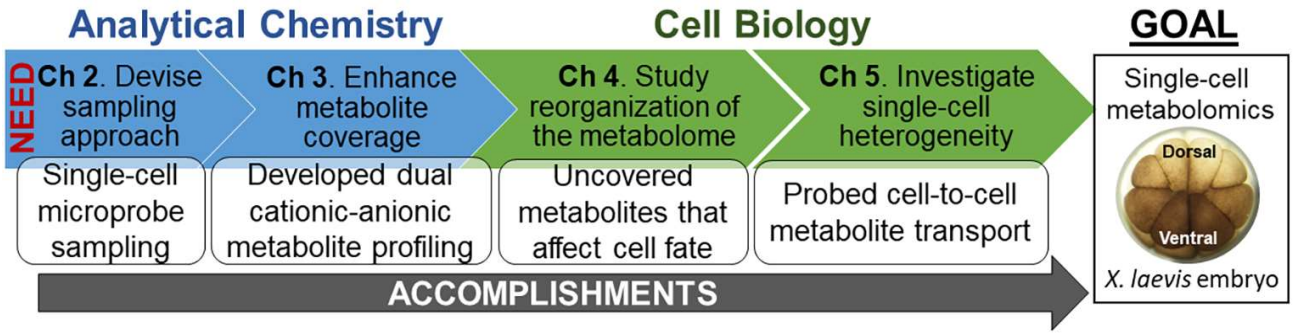

Figure 1.4 Overview of the research strategy executed in this dissertation.

Chapter 2: Current state of single-cell metabolomics with capillary electrophoresis–mass spectrometry

This chapter includes material adapted with permission from:

R.M. Onjiko, E.P. Portero, S.A. Moody, and P. Nemes*, *In situ* microprobe single-cell capillary electrophoresis mass spectrometry: Metabolic reorganization in single differentiating cells in the live vertebrate (*Xenopus laevis*) embryo, Anal. Chem. 2017, 89, 13, 7069–7076. https://doi.org/10.1021/acs.analchem.7b00880

R.M. Onjiko, E.P. Portero, and P. Nemes*, Single-cell metabolomics with capillary electrophoresis- mass spectrometry. Royal Society of Chemistry, 2018, https://doi.org/10.1039/9781788012737-00209

2.1 Fundamentals of capillary electrophoresis

Capillary electrophoresis is a separation method in which a charged analyte migrates inside a thin capillary, under the influence of an electric field. Originally, CE was primarily used for the analysis of biological macromolecules but over the last decades, CE has proven to be useful for the separation of several types of compounds (e.g., amino acids, chiral drugs, vitamins, pesticides, dyes, etc.). The mechanism of separation in CE relies on the differences in ion velocities (v) under the influence of an electric field (E) (see Equation 2.1), and where μ_e corresponds to the constant electrophoretic mobility of the ion.

$$v = \mu_e E \tag{2.1}$$

Since the electrophoretic mobility of an ion depends on its charge-to-radius ratio (q/r) and the viscosity (η) of the buffer, it can be represented as follows (Equation 2.2):

$$\mu_e = \frac{q}{6\pi\eta r} \tag{2.2}$$

Therefore, μ_e depends on the ion's size and charge, as well as the chemical properties of the buffer.[60] For instance, Equation 2.2 establishes that small and highly-charged species will depict higher mobilities compared to their neutral and less charged counterparts.

CE separations are also dependent on the electroosmotic flow (EOF). The EOF is the bulk flow of liquid within the capillary that originates when ions from the solution are present in an applied electric field that encounters a charged solid surface. Moreover, since the charge on the capillary wall is highly dependent on pH, the extent of the EOF can be adjusted by altering several factors including the coating of the capillary wall, ionic strength of the buffer, or pH of the buffer.

During CE separation, a narrow-bore fused-silica capillary (inner diameter <100 μm) is filled with a background electrolyte buffer (BGE), the sample is introduced at the inlet, and the electrical field is applied (Figure 2.1). While small and highly-charged ions move faster than larger ions, solutes also move towards the electrode of opposite charge (e.g., cations migrate towards the cathode, anions towards the anode). However, the ions also move through the capillary in the direction determined by the EOF, regardless of charge. For example, ions moving in opposite direction of the EOF are still flushed to the detector since the EOF exerts more force than their effective electrophoretic mobility. Thus, cations, neutrals, and anions will move in the same direction with the EOF towards detection.

Since the electro-driven force of the EOF is uniformly distributed along the capillary wall, the velocity of the separating ions is nearly identical, resulting in a flat flow velocity profile.[61] The flat flow profile is beneficial because it does not contribute to peak broadening as compared to laminar flow velocity profiles (e.g., in liquid chromatography). In CE, the separation efficiency is expressed in number of theoretical plates (N) (Equation 2.3) where (μ) is the apparent mobility of the ion and (D) is the diffusion coefficient of the solute:

$$N = \frac{\mu E}{2D} \tag{2.3}$$

The theoretical plate numbers in CE are estimated to be ~1 million.[62] Consequently, the theoretical plate height (H), which is a measure of chromatographic efficiency, will result in a small value. For instance, when applying the Van Deemter equation[63] (Equation 2.4) for CE separations, the eddy diffusion (A) and mass-transfer (C) terms are eliminated due to the absence of column packing and solute-wall interactions. Thus, the plate height depends only on the longitudinal diffusion (B) coefficient in CE under ideal conditions.

$$H = A + \frac{B}{u} + Cu \tag{2.4}$$

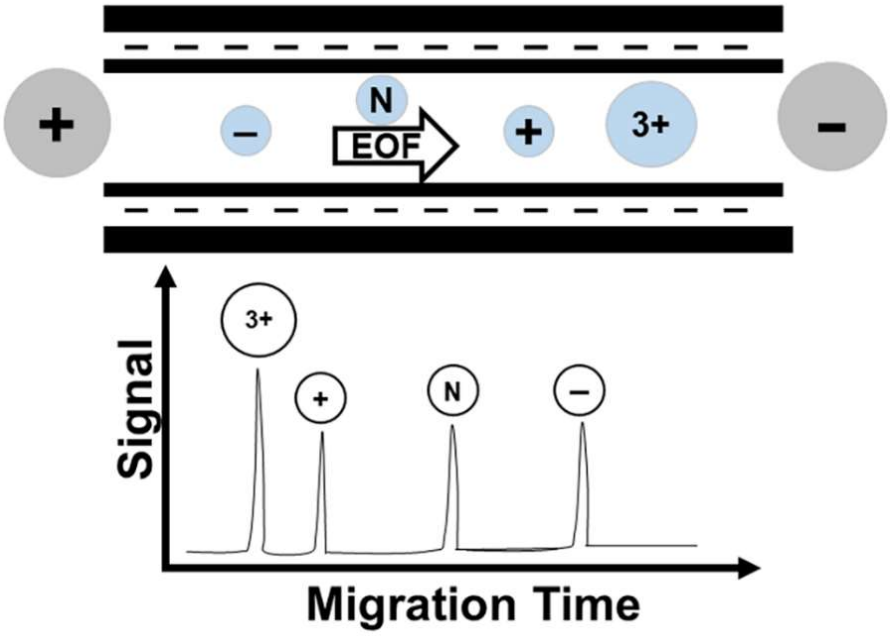

Figure 2.1 Capillary electrophoresis separation depends on the electroosmotic flow (EOF) and electrophoretic mobility of the ionic species. Cationic species migrate from the anode (+) towards the cathode (–) in a fused silica capillary.

2.2 Introduction to single-cell metabolomics with CE-MS

Single-cell analysis promises to be a new frontier in the study of how cells of identical genotype execute molecular programs to acquire important functional differences.[12, 56, 64-66] Molecular analysis with single-cell resolution provides biomolecular insights that would otherwise be masked due to signal averaging by conventional approaches that pool cells for analysis. Characterization of the single-cell metabolome comes with analytical challenges. Metabolites have diverse physicochemical properties (e.g., pKa and hydrophobicity), are highly dynamic, and cover several orders of magnitude in abundance.[64] Compounding these challenges, single cells vary broadly in size across the phyla and even in the same organisms, offering minute amounts of material for detection.[67] Detection of the single-cell

metabolome requires specialized analytical techniques, particularly those capable of low detection limits, high molecular specificity, quantification, and sufficient speed to probe metabolic changes with potentially high turn-over rates.

Single-cell mass spectrometry (MS) is one such technology that enables the characterization of metabolites in single cells. Technologies of single-cell MS employ diverse experimental conditions to provide small-molecule measurements with scalability in molecular coverage, spatial and temporal resolution, and/or operation under denaturing or native conditions. An overview of single-cell MS is available in references[64, 68-73]. A subset of single-cell MS technologies employs some form of separation to advance the detectable coverage of the single-cell metabolome. Liquid-phase separation before electrospray ionization (ESI) MS aids molecular detection by obtaining compound-dependent information, viz. the time a compound spends in separation, and/or by removing interferences during ion generation or spectral detection. Additionally, gas-phase separation in an ion mobility analyzer helps reduce spectral interferences and quantify collision-cross sections as compound-dependent information. This strategy has detected ~400 ion signals and identified 23 metabolites and lipids from single *A. thaliana* cells.[29]

This chapter reviews trace-sensitive CE-MS, which has demonstrated several advantages for single-cell metabolomics.[70] Perhaps most importantly, CE is compatible with the limited sample volumes that are contained by single cells. CE also obtains exquisite separation peak capacity to efficiently reduce the complexity of metabolite mixtures and help distinguish isobaric compounds prior to detection. The Nemes lab[12, 30, 55, 57, 74] and others[31, 56, 65, 75] have coupled CE to electrospray ionization

(ESI) MS and developed specialized workflows to detect hundreds of metabolite features in single cells.

The general approach of single-cell studies is presented in Figure 2.2. The workflow begins with the identification and isolation of cells and is followed by sampling of their content before metabolites are extracted. In CE, extracted metabolites are separated based on differences in electrophoretic mobility, are ionized (usually by ESI), and metabolite ions are detected by MS–MS/MS. With a thoughtful experimental design, it is possible to identify metabolite signals and quantitatively compare their profiles between cells. By quantifying hundreds of metabolite features, CE-ESI-MS has enabled us to distinguished cells and cell types based on metabolic composition, including single neurons in the central nervous system of the giant sea slug (*Aplysia californica*)[14, 65, 76] and embryonic cells of the 8-,[30, 57, 74] 16-,[12, 55] and 32-cell[55] embryo of the South African clawed frog (*Xenopus laevis*). Furthermore, data from these studies have allowed us to design functional experiments that led to the discovery of small molecules capable of altering the normal tissue fate of embryonic cells.[12] The next sections provide an overview of the major steps of the single-cell CE-ESI-MS analytical workflow.

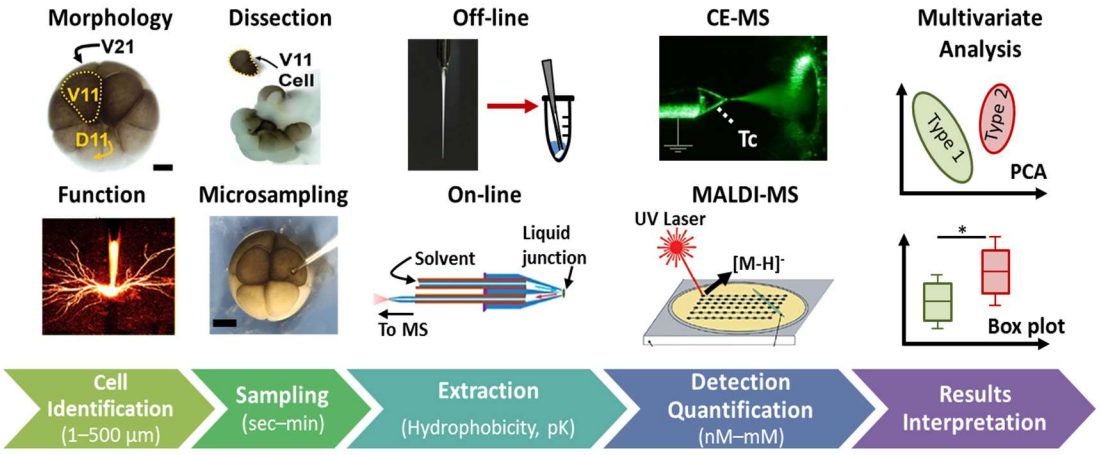

Figure 2.2 Workflow for single-cell metabolomics. Reproduced from ref. 41 with permission from The Royal Society of Chemistry.

2.3 Sampling of single cells

The goal of this step is to collect cellular content from individual cells, providing the "sample" for further processing prior to CE-MS (Figure 2.2). Depending on the purpose of the study, cell sampling may involve an initial step to define cells of a particular phenotype before sampling commences. Morphology and established cell maps have allowed the distinction of cell types in powerful biological models, such as individual neurons in the central nervous system of *Aplysia californica*,[14] crabs,[77-78] and *Drosophila melanogaster* (fruit fly).[79] Likewise, based on cell morphology and cell fate maps,[58-59, 80] we have identified cells occupying the left–right, dorsal–ventral, and animal–vegetal axes of the *X. laevis* embryo and used single-cell CE-ESI-MS to compare their metabolomic composition. These studies revealed that the neural-tissue fated D11 cell, the epidermal-fated V11 cell, and the hindgut-fated V21 cell produced distinct metabolomes in the 16-cell *X. laevis* embryo.[12] Cell types may also be distinguished based on functional studies, such as electrophysiological recordings,

before chemical analysis. For example, metabolites were recently measured in excitatory glutamatergic and inhibitory GABAergic neurons in the rat brain by CE-MS.[56] For cell types that express known molecular markers, high-resolution fluorescence imaging facilitates cell identification. The success of this approach is exemplified by *in situ* hybridization marking neurons in the *A. californica* central nervous system during development, neurogenesis, and metamorphosis.[81] Similarly, molecular markers allow fluorescence or magnetic activated cell sorting (FACS or MACS, resp.) to separate particular cell types in high-throughput from cell suspensions (see reviews in ref.[82-88]). In developing biological systems, optical imaging may be necessary to identify cells in precursor–progenitor relationships. For example, we have used morphology (e.g., pigmentation and size) and fluorescent dyes to track cell clones in the 8-, 16-, 32-, 64-, and 128-cell *X. laevis* embryo before characterizing their small molecules[12, 55, 57, 89] and proteins[9, 19, 90] by CE-ESI-MS. Alternatively, high-throughput imaging by single-cell MALDI MS enables the recognition of cell types based on chemical composition without information of phenotype, morphology, or location, as recently demonstrated for cells in rat pancreatic islets.[31]

To collect a portion of whole cells, different technologies have been developed with scalability in size and collection speed (Figure 2.3). Manual dissection[31, 91] is readily amenable to larger cells. As shown in Figure 2.3A, sharp tungsten needles, fine forceps, or finer tools have been used to isolate 50–500 μm cells from *A. californica*,[14] a mouse ganglion,[56] or *X. laevis embryos*.[12, 57, 92] With a modest throughput, microdissection offers the benefit of preserving information on the spatial

origin of isolated cells, which can add important information to address biological questions, such as signaling molecules expressed in neuronal circuits[14, 56, 76] or metabolites implicated in cell-fate decisions.[12] For smaller cells, which challenge dissection accuracy, approaches capable of finer resolution were introduced. Sharpened or pulled capillaries were found to be able to reproducibly target and aspirate picoliter-to-nanoliter volumes from rat thalamic neurons,[56] tomato trichome cells,[93] and frog embryonic cells,[55] as shown in Figure 2.3A. Capillaries containing dual barrels helped enhance the throughput of these measurements. Figure 2.3B exemplifies how this strategy was able to collect metabolites from multiple *Allium cepa* cells.[94] Fluid force microscopy takes an alternative approach, in which a cantilever is driven by an atomic force microscope to probe subpicoliter volumes from human cervical cancer (HeLa) cells (Figure 2.3C).[95]

Capillary sampling has also been coupled to CE-MS. Representative examples include the metabolic study of single neurons in the rat thalamus[56] and single *X. laevis* cells.[12, 55] In both cases, microsampling allowed the same cell to be sampled multiple times. Surprisingly, *in situ* microsampled cells were found to continue cell division as the embryo developed to the next stage.[55] Alternatively, fluid force microscopy[95] or laser capture microdissection[96] may be used to sample cells. Recently, a combination of MALDI-MS and CE-ESI-MS was used to differentiate single α and β cells from a rat pancreatic islet based on peptide content (Figure 2.3D).[31]

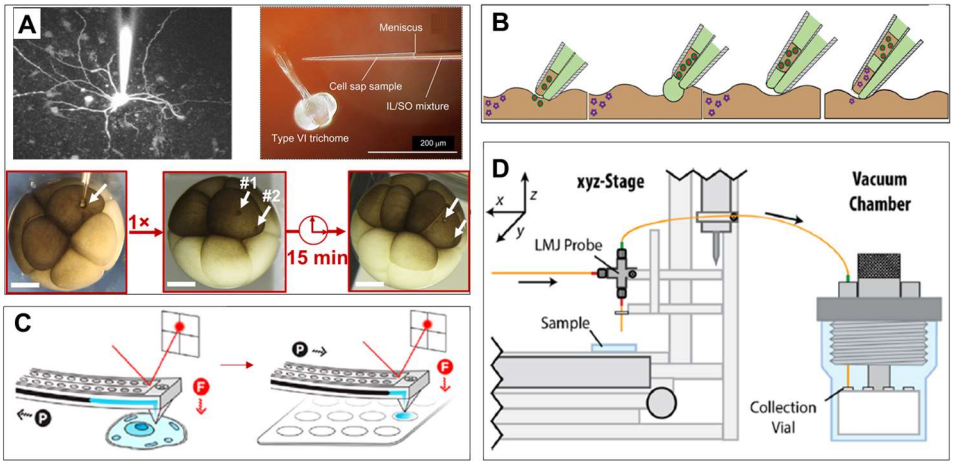

Figure 2.3 Examples of approaches enabling single-cell sampling. (A) Fine-pulled capillaries were used to withdraw the cytoplasm of a single thalamic neuron in the rat brain, a single type VI stalk cell from intact tomato trichomes, and the right ventral-animal (V1) cell in the 8-cell *Xenopus laevis* embryo. (B) A dual-barrel pipette for sampling individual *A. cepa* cells. (C) Fluid force microscopy probe was used to aspirate the cytoplasm from HeLa cells. (D) Using a liquid junction interface, metabolites were extracted from identified cells in a rat pancreatic islet for MALDI. Reproduced from ref. 41 with permission from The Royal Society of Chemistry.

High-fidelity sampling is essential since it can greatly aid with result interpretation in single-cell studies. With sufficiently fine spatial resolution, cross-contamination can be eliminated or, at least, assigned to neighboring cells. Fast sampling can minimize metabolic changes arising from endogenous metabolism, transitions in cell cycle, or metabolic degradation, thus providing a credible snapshot of the cell's metabolic activity state. Using capillary microsampling, we recently aspirated a portion of identified embryonic cells with a 5 s/cell throughput (Figure 2.4A), compared to 5 min/cell by manual dissection. With minimal damage to the cell, capillary microsampling CE-MS significantly lowered oxidative stress during sampling (Figure 2.4B), thus yielding metabolomic data that more closely represent the native state of cells in *X. laevis*.[55]

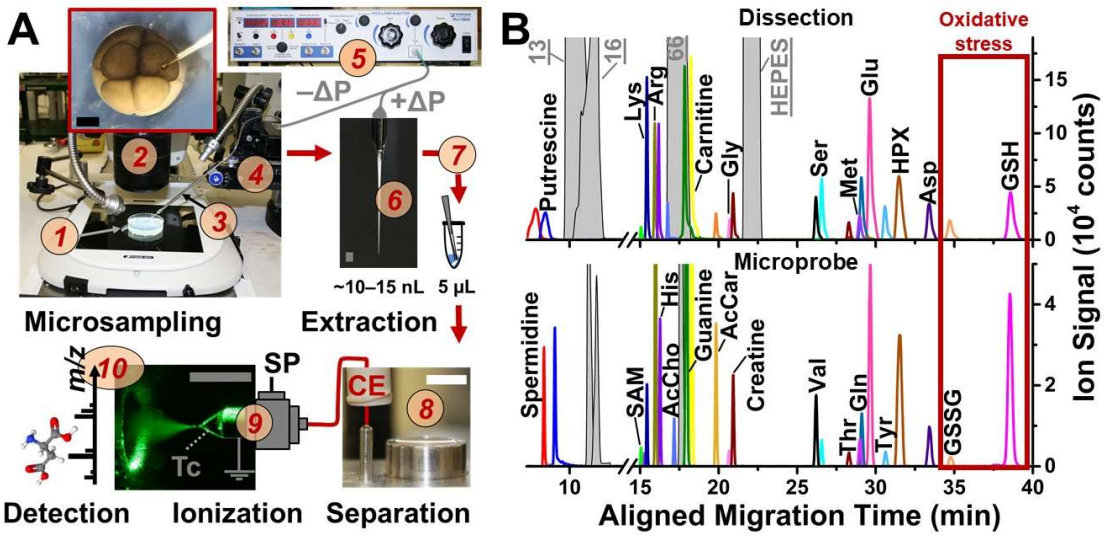

Figure 2.4 Microprobe sampling and metabolite detection by CE-MS. (A) Microprobe CE-MS workflow enables in situ metabolic characterization of live *X. laevis* embryos. (B) Representative electropherograms show a decrease in oxidative stress (GSSG/GSH) by microprobe sampling. Adapted with permission from ref. 55. Copyright 2017 American Chemical Society.

2.4 Metabolite extraction

Immediately after sampling, the whole cell or a collected portion of its content is processed to preserve and extract endogenous metabolites. Enzymes may be deactivated/denatured by inhibitors, chemicals, or temperature-shock.[97-98] We and others have found the combined use of volatile organic acids (e.g., formic/acetic acid), volatile organic solvents (e.g., methanol/acetonitrile mixtures with water), and low temperatures (4 °C) during sample processing to be sufficient to stabilize the extracted metabolites for up to 1 month when the extracts are stored frozen at −80 °C.[12, 55, 57, 99] The chemical stability of the extract may be improved by addition of stabilizing agents. Glycerol, a known cryogenic preservative, has improved the

reproducibility of metabolite quantification by 4-fold in single *A. californica* neurons.[76]

Next, metabolites are extracted from the collected specimen using solvents. To broaden detection coverage, extraction typically exploits a combination of solvents that are tailored to the physicochemical properties of the compound classes of interest (e.g., amino acids, lipids, or sugars). In addition, the pH of the solvent is adjusted to facilitate ionization. The extraction solution may consist of miscible or immiscible solvents with the latter allowing for subsequent fractionation. Because cells can exhibit varying physical properties and chemical compositions, even in the same tissue or organisms, we recommend optimizing and validating the method of extraction using the cells of interest. We found modeling the physicochemical properties to be helpful in guiding the initial design of single-cell experiments. Figure 2.5A shows an example in which the octanol/water distribution coefficients (D) were calculated at different pHs, which helped select a series of polar–apolar solvent mixtures to enhance the extraction of select metabolite classes from single *X. laevis* cells (Figure 2.5B).[57] In addition, we also found the use of chemical standards to be ideal to establish the optimal pH and solvent composition for enhanced quantitative recovery and ionization efficiency, as well as to tune the ESI mass spectrometer for sensitivity.

To enhance the analytical performance of single-cell CE-ESI-MS, extraction may be supplemented with additional steps. Internal standards added to the extraction solvent system or the resulting extract can help with qualitative and quantitative testing of the robustness of sampling, quantitative recovery, and the reproducibility of

CE separation, as well as correcting for fluctuations in ESI-MS performance (e.g., by normalization). An isotopologue of the analyte serves as the internal standard of choice because it has similar physicochemical properties to the metabolite of interest without interference in detection. Depending on endogenous concentration and detection sensitivity, pre-concentration steps (e.g., off-column or on-column) may be necessary to enrich metabolites with low abundances. Desalting or fractionation steps may be performed to reduce sample complexity and matrix interferences, albeit at the risk of analyte losses and/or modifications to the metabolome. We have found simplicity and speed to be efficient guides during the design of our single-cell metabolomic workflows.[12, 57]

Another purpose of extraction is to improve separation by CE and detection by ESI-MS. Extraction has the benefit of simplifying the molecular complexity of the extract, thus removing potential interferences during ion generation by ESI and mass analysis (spectral) by MS. Microprobe CE-ESI-MS, which aspirates small amounts of cellular content (~10 nL), was found to improve the separation and yield a comparable signal-to-noise ratio to whole-cell (~90 nL) dissected samples (Figure 2.4B). The improvement was attributed to the ability of capillary microsampling to collect substantially smaller amounts of salts, buffers, and other additives from the embryo culturing medium, which would otherwise interfere with CE separation and ionization.[55, 57]

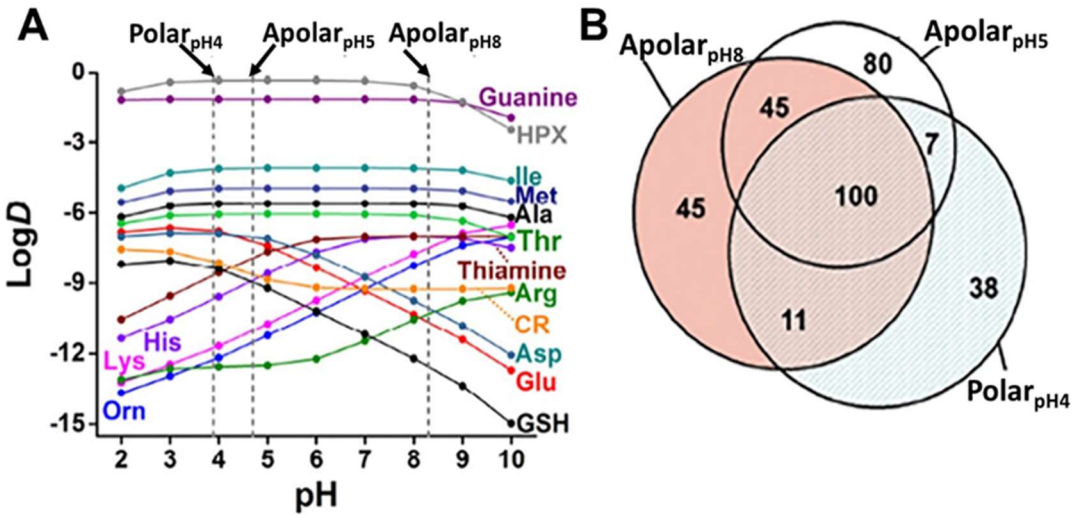

Figure 2.5 Sample processing strategies for improved detection sensitivity in single-cell CE-MS. (A) Modeling of physicochemical properties, such as the distribution coefficient (D), helps guide the selection of extraction solvents. (B) Extraction using solvents with different pH and polarity enhanced metabolic coverage in single *X. laevis* cells. Polar$_{pH4}$, 50% methanol with 0.5% acetic acid; Apolar$_{pH4}$, 40% acetonitrile with 40% methanol; Apolar$_{pH8}$, 40% acetonitrile with 40% methanol at pH 8. Reproduced from ref. 41 with permission from The Royal Society of Chemistry.

2.5 Detection by capillary electrophoresis–mass spectrometry

Next, the cellular aspirate is analyzed by CE-ESI-MS, which entails a subset of tasks: the sample is injected into a separation capillary, metabolites are separated based on differences in their electrophoretic mobility, ionized by ESI, and the generated metabolite ions are mass-analyzed using a mass spectrometer (Figure 2.2). With nano-liters of sample consumption, CE is ideally suited to analyze metabolites in volume limited extracts from single cells. The Sweedler[65, 100] and Nemes[9, 12] laboratories have custom-built single-cell CE-ESI platforms for MS. Construction and operation of these CE ESI-MS platforms follows a prototype published in ref.[100-101] Briefly, as shown in Figure 2.6, the instrument features a manual injection stage

confined within an electrically insulated enclosure equipped with a safety interlock. To load ~10 nL of sample into the separation capillary, a <1 μL portion of the cell extract is deposited into a sample vial where the CE capillary is positioned and then the injection platform is elevated to enable hydrodynamic injections of the sample. CE separation is performed by translating the capillary inlet end into the background electrolyte (BGE) and applying ~20 kV across the ~1 m long capillary.

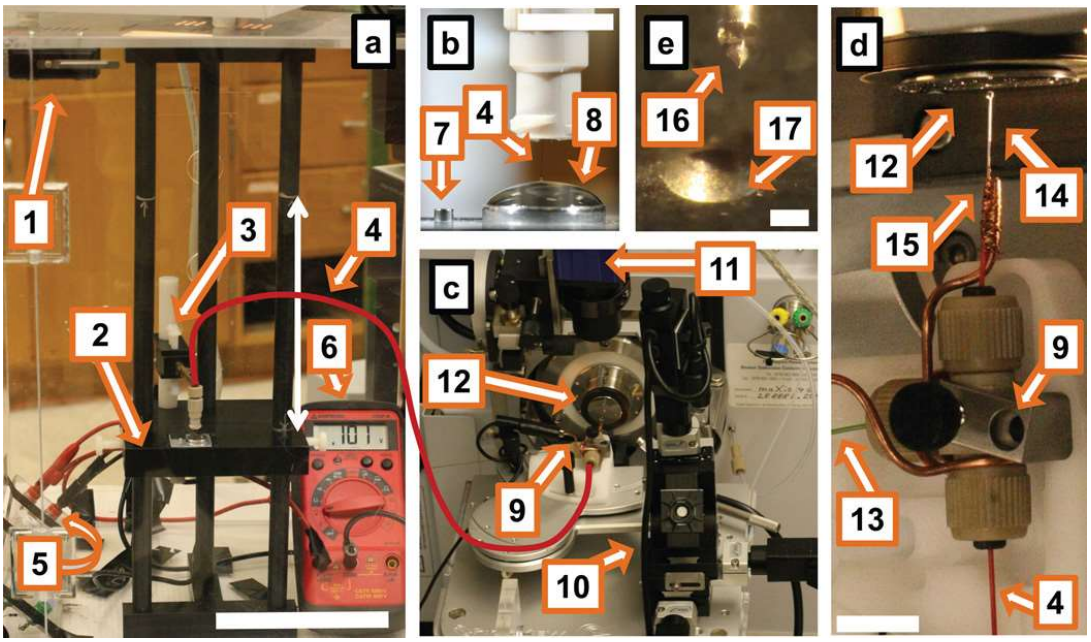

Figure 2.6 A custom-built CE-ESI-MS platform for characterizing metabolites in single-cells. (a) Major components include: (1) a safety-interlock-enabled enclosure, (2) a sample loading platform, (3) a holder for (4) a fused silica separation capillary, (5) a resistor, (6) and a digital multimeter. (b) A close-up view of the sample-loading platform: (7) a sampling vial and (8) background electrolyte vial. (c) The CE-ESI-MS ionization source: (9) the CE-ESI interface on a (10) three-axis translation stage, (11) a camera to monitor the ESI interface, and (12) a mass spectrometer. (d, e) A magnified view of the T-union that connects the (4) separation capillary, (13) secondary capillary supplying sheath solvent, and the (14) metal-emitter for generating the electrospray in the (15,16) cone-jet regime. Reproduced from ref. 41 with permission from The Royal Society of Chemistry.

ESI is the most commonly used technology to ionize CE-separated metabolites for MS detection. CE-ESI interfaces vary greatly in design and performance (see reviews in ref.[102-104]). We apply a modified form of the original co-axial sheath-flow design,[105] which has been found to provide robust operation since inception. In our design, the nebulizer gas is removed to help direct the electrospray plume to the mass spectrometer, the dimensions of the emitter are scaled to the separation capillary to minimize sample dilution in the ion source, and the geometry of the electrospray emitter and the operation parameters are carefully chosen to maintain the electrospray in the stable cone-jet regime, which provides the most efficient ionization.[106] This CE-ESI interface provides a 60 amol lower limit of detection and 4–5 log-order dynamic range for quantification.[12] Furthermore, we have most recently developed a second-generation version of this interface, which uses a tapered-tip emitter to achieve 260 zmol (156 000 copies) sensitivity for peptide standards.[107] These CE-ESI-MS platforms have allowed the detection of hundreds of metabolite signals from single cells that were isolated from *A. californica* neurons[100] and *X. laevis* embryonic cells,[12, 55, 57] including the identification of ∼100 metabolites with significant metabolic differences between cell types. Development and recent commercialization of alternative designs, such as low-flow sheath[108] and sheathless[109] interfaces, raise opportunities to further the sensitivity of CE-ESI for single-cell metabolomics.

Various strategies can be applied to enhance the throughput of single-cell measurements using CE-ESI-MS. For example, capillary batch injection enables multisample measurements and up to 80–100% injection efficiency.[110] To improve

sensitivity for low abundance metabolites, online preconcentration methods, such as sample stacking,[111] can be incorporated into the workflow. Figure 2.7A shows large-volume sample stacking allowing nucleotides to be detected from a 60 μm *A. californica* neuron.[112] For higher throughput, multi-segmented injection offers significant benefits. Figure 2.7B presents one such example, in which human plasma extracts were measured 10-times faster, with ~3 min per sample throughput without compromising identification or quantification.[113]

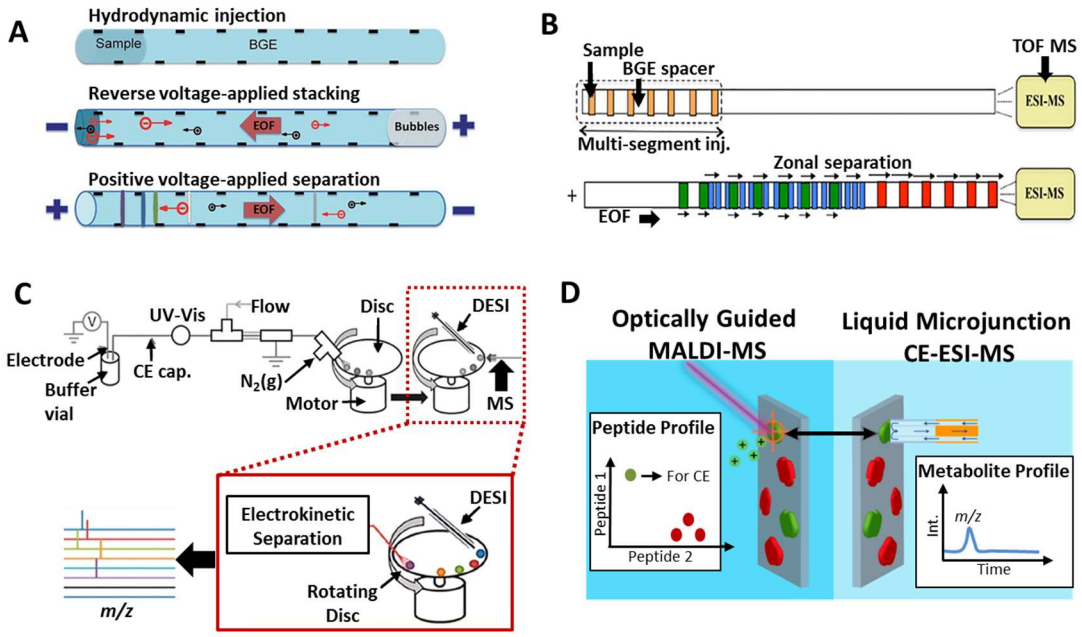

Figure 2.7 Recent advances to enhance CE-MS measurement throughput and sensitivity. (A) Large-volume sample stacking improved detection sensitivity. (B) Multi-segmented injection enhanced throughput to 3 min/sample. (C) CE with desorption electrospray ionization (DESI) minimized ion suppression effects due to salts and detergents. (D) Optically guided MALDI-CE-MS screened large numbers of cells based on peptide and metabolite composition. Reproduced from ref. 41 with permission from The Royal Society of Chemistry.

Other ionization sources provide complementary benefits to single-cell CE-MS. Figure 2.7C shows the hyphenation of CE to desorption electrospray ionization (DESI): the separated compounds are dried onto a rotating teflon disk, whence they are desorbed and ionized by focused charged droplets with improved tolerance for salts and detergents.[114] Figure 2.7D presents another setup in which MALDI was off-line coupled to CE-MS to profile cells in rat pancreatic islets.[31] After α- and β-cell types were distinguished based on their peptide content,[72, 115] the dried samples were microextracted for metabolic analysis by CE-ESI-MS. To broaden the coverage of the metabolome, both negative[112] and positive ionization modes may be used and/or multiple analytical platforms combined.

2.6 Data processing

The last step of the workflow is aimed at identifying and/or quantifying metabolite signals between single cells (Figure 2.2). CE-ESI-MS studies utilize multiple dimensions of information to this end, including accurate *m/z*, migration time, fragmentation, and peak intensity/area. Representative separations are demonstrated for select metabolite signals in Figure 2.8A. Comparison of these orthogonal pieces of information makes confident identification possible for any metabolite that can be obtained as a chemical standard or for which tandem MS information is available in a tandem MS database, such as mzCloud and Metlin.[116] For example, Figure 2.8A shows a signal at *m/z* 175.1188 in the D11 cell from the 16-cell *X. laevis* embryo with identification as arginine based on accurate *m/z* and MS–MS/MS information acquired from standard arginine. Under-the-curve peak areas

provide a proxy for relative quantification, and with the use of external concentration calibration, for absolute quantification. Figure 2.8B exemplifies the quantification of serine in the R15 and left pleural 1 (LPl1) cell of *A. californica* via concentration calibration.[12, 14, 100] Quantification provides a powerful tool for targeted or discovery characterization of cells or cell types, particularly when combined with statistical or multivariate tools, such as hierarchical cluster analysis (HCA), partial least squares discriminant analysis (PLS-DA), or principal component analysis (PCA). For example, Figure 2.8C shows HCA of metabolites with significant enrichment differences between three cell types in the same 16-cell embryo of *X. laevis*. These data analysis tools are available in many publicly available software packages, including XCMS,[117] MetAlign,[118] MSFind, MS-DIAL,[119] MetaboAnalyst,[120] MZmine,[121] and GNPS,[122] for the analysis of single-cell MS data.

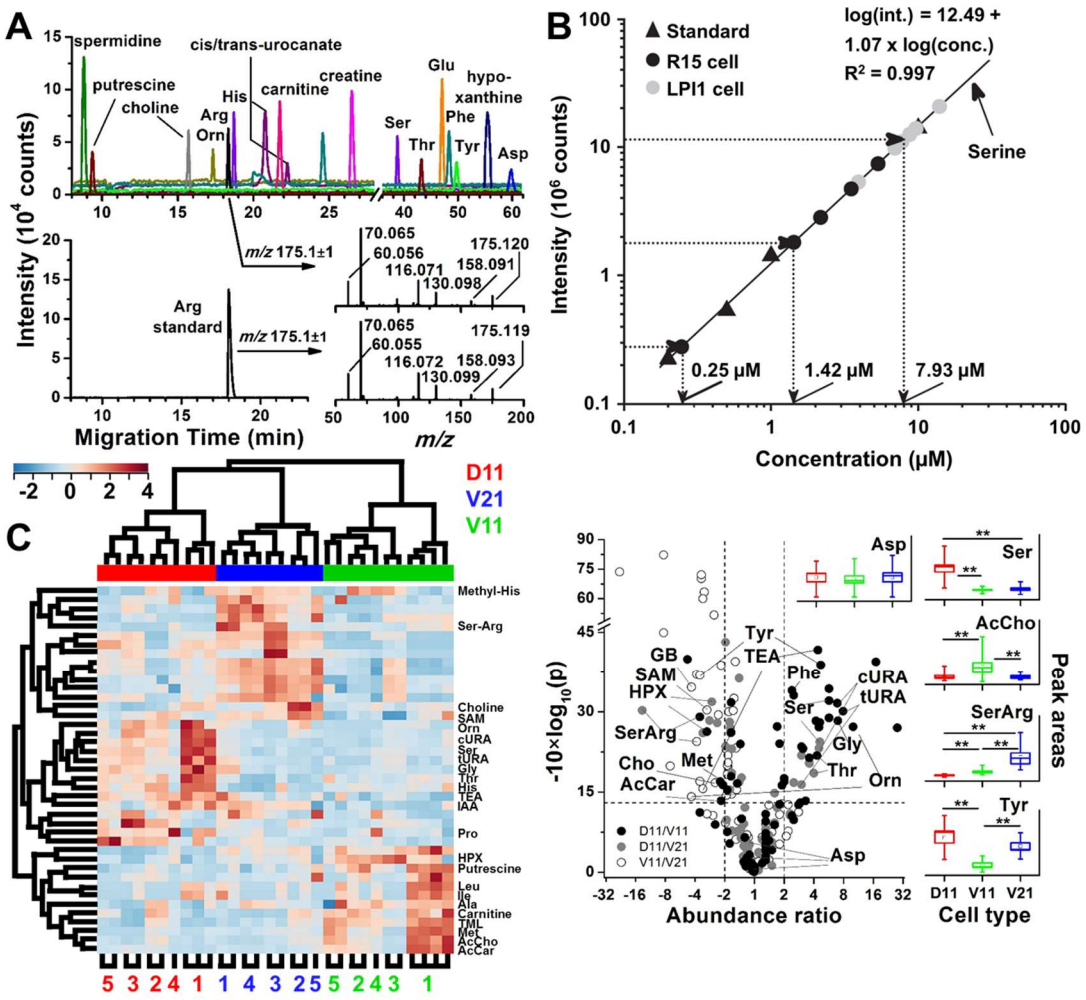

Figure 2.8 Identification and quantification of small molecules in single cells. (A) Electropherogram showing select identified small molecules measured from an individual cell derived from a 16-cell *Xenopus laevis* embryo. Representative identification of a metabolite signal as arginine in a *X. laevis* cell (B) Quantification of serine in different R15 and LPl1 neurons of *A. californica*. (C) Hierarchical cluster analysis differentiating the D11, V11, and V21 cells in 16-cell *Xenopus laevis* embryos and volcano plot shows significant metabolite differences between the cells. Reproduced from ref. 41 with permission from The Royal Society of Chemistry.

2.7 Conclusions

CE and MS combine excellent analytical figures of merit for single-cell metabolomics. CE is compatible with the limited amounts of material that are contained in cells and has exquisite separation resolution to address complex metabolite extracts. Various on-column pre-concentration techniques by CE enhance detection to trace-level sensitivity (e.g., ~60 amol or 10 nM by FACS), allowing one to measure metabolites over broad dynamic concentration ranges exhibited in biological systems. MS detection complements CE with high molecular specificity, label-free operation, and capability for quantification of broad types of metabolites in cells. Data resulting from single-cell CE-MS has shed new light on small-molecule differences between cells in various tissues and model organisms, ranging from metabolites in early stages of developing vertebrate embryos[12] to signaling molecules in the nervous system.[123]

Continuing technological advances promise exciting opportunities to advance our understanding of cell biology.[53] Sampling approaches with faster operation and scalability in space and time allow a larger number of cells to be probed, thus enhancing statistical power to uncover differences between cells and to characterize cells at the whole population level. These developments in fast sampling can be supported by analyses capable of higher throughput, including sample processing on microfluidic devices,[124] separation by microchip electrophoresis,[125] and ionization by MALDI[31, 70] or ESI[12, 65, 100] mass spectrometers. To analyze the large amounts of complex data from these studies, software tools capable of statistical and multivariate analyses are needed, particularly those that can address the narrow and often low-

level signals that are expected from single-cell studies. Parallel advances in the steps of the single-cell CE-MS workflow can help extend this powerful bioanalytical technology to systems biology studies on cells and limited cell populations, promoting the understanding of molecular mechanisms that affect cell and developmental processes.

Chapter 3: Enabling dual cationic–anionic profiling of metabolites in a single cell of the *Xenopus laevis* embryo by CE-ESI-MS

This chapter has been published as a peer reviewed journal article. Reproduced from: E.P. Portero and P. Nemes*, Dual cationic–anionic profiling of metabolites in a single identified cell in a live *Xenopus laevis* embryo by microprobe CE-ESI-MS, Analyst, 2019, 144, 892–900. https://doi.org/10.1039/C8AN01999A with permission from The Royal Society of Chemistry.

In situ microprobe sampling and CE-ESI-MS enabled the characterization of cationic metabolites in single cells in complex tissues and organisms.[55] However, for a deeper coverage of the metabolome and metabolic networks, analytical approaches are needed that provide complementary detection for anionic metabolites, ideally using the same instrumentation. This chapter describes the development of a CE-ESI-MS approach that enables sequential cationic and anionic (dual) analysis of metabolites in the same identified cell in a live vertebrate embryo. A calibrated volume was microaspirated from the animal-ventral cell in a live 8-cell embryo of *Xenopus laevis*, and cationic and anionic metabolites were one-pot microextracted from the aspirate, followed by CE-ESI-MS analysis of the same extract. A laboratory-built CE-ESI interface was reconfigured to enable dual cationic–anionic analysis with ~5–10 nM (50–100 amol) lower limit of detection and a capability for quantification. To provide robust separation and efficient ion generation, the CE-ESI interface was enclosed in a nitrogen gas filled chamber, and the operational parameters were

optimized for the cone-jet spraying regime in both the positive and negative ion mode. A total of ~250 cationic and ~200 anionic molecular features were detected from the cell between m/z 50–550, including 60 and 24 identified metabolites, respectively. With only 11 metabolites identified mutually, the duplexed approach yielded complementary information on metabolites produced in the cell, which in turn deepened network coverage for several metabolic pathways. With scalability to smaller cells and adaptability to other types of tissues and organisms, dual cationic–anionic detection with *in situ* microprobe CE-ESI-MS opens a door to better understand cell metabolism.

3.1 Introduction

Single-cell mass spectrometry (MS) provides a molecular snapshot to investigate the phenotypical and physiological state of a cell;[64] the technology is qualitative, capable of label-free detection, and can be made quantitative. As a downstream product of transcription and translation, the metabolome, comprising of all metabolites produced by a cell, responds dynamically and rapidly to intrinsic and extrinsic events to the cell. Therefore, the single-cell metabolome raises a new frontier in the study of molecular events underlying cell differentiation and the establishment of cell-to-cell differences (cell heterogeneity) during normal and impaired development.

Detection of the single-cell metabolome presents grand analytical challenges for MS since the metabolome encompasses vast molecular complexity and spans a broad dynamic range of concentration. Other challenges arise from varying

dimensions as cells develop and different physical and temporal positions that they assume in tissues and developing organism. For example, blastomeres become progressively smaller and undergo long-range movements during morphogenesis in vertebrate embryos.[126] To better understand cell metabolism, specialized approaches are required that integrate spatially and temporally scalable sample collection, particularly in complex tissues and organisms, with trace-sensitive MS for broad types of metabolites.

Recent developments in CE-MS technology raise a potential toward anionic metabolomics in single cells (see reviews in ref.[127-130]). Low limits of detections (~10–200 nM) and high measurement reproducibility were accomplished for anions from metabolite standards and extracts of tissues and biological fluids using CE-MS interfaces that employ sheathflow,[112, 131] low-flow electrokinetically-pumped,[26, 132] and sheathless[75] interface designs. Nucleotides were most recently profiled in single neurons from *Aplysia californica* using a coaxial sheath-flow CE-ESI interface.[112] In principle, the combination of cationic and anionic analysis holds the potential to deepen metabolic coverage in single cells. However, individual cells contain prohibitively limited amounts of materials for independent sample processing that is typical for cationic and anionic analysis. Additionally, complex CE-ESI interface designs and the use of different CE capillaries for cationic and anionic measurements (e.g., chemically derivatized capillaries) lower analytical throughput, hindering the analysis of multiple single cells to facilitate results interpretation.

Described here is a simplified methodology that enables the dual analysis of cationic and anionic metabolites in single cells of live embryos. We used capillary

microsampling to collect cell material from identified single cells in live *X. laevis* embryos, which was followed by a one-pot micro extraction of anionic and cationic metabolites from the collected material. A custom-built sheath-flow CE-ESI interface was supplemented with a nitrogen gas filled environmental chamber to minimize electrical discharges at the electrospray emitter to ensure stable and efficient ion generation for detection. Cationic and anionic analysis using the same bare fused silica capillary with different background electrolytes provided complementary metabolite identifications, yielding a deeper coverage of metabolic networks than was feasible using each approach in isolation using single-cell CE-ESI-MS.

3.2 Experimental

3.2.1 Chemicals

LC-MS grade solvents and chemicals including formic acid, ammonium bicarbonate, methanol, acetonitrile, isopropanol, and water were purchased from Fisher Scientific (Fair Lawn, NJ), unless otherwise noted. Trizma hydrochloride and trizma base were obtained from Sigma Aldrich (Saint Louis, MO). Cysteine was from MP Biomedicals (Solon, OH).

3.2.2 Solutions

Steinberg's solution (100% v/v) and cysteine solution (2% v/v) were prepared following standard protocols.[126] The "metabolite extraction solvent" consisted of 40% (v/v) methanol and 40% (v/v) acetonitrile in water (pH 4.7). For cationic analysis, the CE "background electrolyte" (BGE) solution was 1% (v/v) formic acid (pH 2.8) and

the electrospray sheath solution was 50% (v/v) methanol in water containing 0.1% (v/v) formic acid. For anionic analysis, the BGE was 20 mM ammonium bicarbonate (pH 8.2), and the electrospray sheath solution was 0.2 mM ammonium bicarbonate in 50% (v/v) isopropanol.

3.2.3 Animal care and embryo collection

All protocols regarding the humane care and handling of animals were approved by the University of Maryland Institutional Animal Care and Use Committee (IACUC no. R-DEC-17-57). Male and female adult *Xenopus laevis* frogs were purchased from Nasco (Fort Atkinson, WI) and maintained in a breeding colony. Embryos were obtained via gonadotropin-induced natural mating following established protocols.[126] The jelly coating of freshly laid embryos was removed as described elsewhere.[133] Dejellied embryos were transferred to a Petri dish containing 100% Steinberg's solution (SS). Two-cell stage embryos showing stereotypical pigmentation patterns[134] across the dorsal-ventral and left-right axis were cultured in 100% SS to the 8-cell stage for this study.

3.2.4 Single-cell sampling and metabolite extraction

The left animal-ventral (V1) cell was identified in 8-cell embryos in reference to established cell-fate maps.[135] An ~10 nL aliquot of cellular content was aspirated from the cell using microcapillary sampling following our recent protocols.[55, 101] To extract small polar metabolites from the aspirate, the sample was expelled into 4 μL of metabolite extraction solution at ~4 °C and vortex-mixed for ~1 min at room temperature before centrifugation at 8000g for 5 min at 4 °C to pellet cell debris.

Metabolite extracts were stored together with the cell debris at −80 °C until CE-ESI-MS analysis.

3.2.5 Single-cell CE-ESI-MS

Single-cell metabolite extracts were measured using a laboratory-built microanalytical CE-ESI system coupled to a quadrupole time-of-flight mass spectrometer (Impact HD, Bruker Daltonics, Billerica, MA), following our established protocols.[12, 55, 101] In this study, CE separation was performed in a 1-meter long bare fused silica capillary with 40/105 μm inner/outer diameter (Polymicro Technologies, Phoenix, AZ) with the outlet end grounded using a custom-built coaxial sheath-flow CE-ESI interface.[100] Cationic analysis implemented the following parameters: CE separation at +20–22 kV (applied to capillary inlet) in 1% formic acid (yielding ~7.5–8 μA CE current); CE-ESI interface operated in the cone-jet regime (0.1% formic acid in 50% methanol supplied at 1 μL min^{-1} as sheath flow) at −1700 V spray potential applied to mass spectrometer front plate; CE-ESI environmental chamber, no nitrogen supplied (ambient air as bath gas). Anionic analysis was performed using the following settings: CE separation at +17–19 kV (applied to capillary inlet) in 20 mM ammonium bicarbonate (yielding 4.9–5.6 μA CE current); CE-ESI interface operated in the cone-jet electrospray regime (0.2 mM ammonium bicarbonate in 50% isopropanol supplied at 0.6 μL min^{-1} as sheath) at +2100 V spray potential applied to the mass spectrometer front plate; CE-ESI environmental chamber, nitrogen supplied at 0.6 L min^{-1}. In both cationic and anionic measurements, the stability of the CE-ESI interface was characterized by ion current

measurements using a mass spectrometer and by direct optical inspection of the electrified liquid meniscus using a stereomicroscope (40× magnification, Simul-Focal Stereomicroscope, United Scope, Irvine, CA). Identification of the electrospray regimes was performed as detailed elsewhere.[106]

Ions generated by CE-ESI were detected using a quadrupole time-of-flight mass spectrometer (Impact HD, Bruker). Experimental settings were the following: MS survey scan rate, 2 Hz; mass range (MS^1 and MS^2), *m/z* 50–550; collision-induced dissociation, 18–20 eV in nitrogen collision gas; dry gas, nitrogen at 2 L min^{-1} at 100 °C for positive and 150 °C for negative ionization mode. The mass spectrometer was externally mass-calibrated to <5 ppm accuracy by analyzing 150 mM sodium formate using CE-ESI in the positive ion mode and directly infusing 10 mM sodium formate (in 0.2 mM ammonium bicarbonate prepared with 50% v/v isopropanol) through the CE-ESI interface in the negative ion mode.

3.2.6 Data analysis

Raw MS-MS/MS data were processed using a custom-written script in Compass DataAnalysis version 4.3 (Bruker Daltonics) as described elsewhere.[12] Briefly, each file was externally calibrated to <1 ppm accuracy (enhanced quadratic calibration mode) for sodium formate cluster ions that were formed in the ion source as salts separated from the samples, molecular features were semi-manually surveyed between *m/z* 50–550 with 5 mDa increments, and the resulting accurate *m/z* and migration time information were recorded for each detected molecular feature. Under-the-curve peak areas and signal-to-noise (signal/noise) ratios were calculated

using Compass 4.3 (Bruker Daltonics). Metabolic pathway analysis was performed in MetaboAnalyst 4.0[120] using the Kyoto Encyclopedia of Genes and Genome (KEGG) metabolomic knowledgebase (http://www.genome.jp/kegg) with the following settings: Pathway library, *Danio rerio* (zebrafish); pathway analysis algorithms, overrepresentation analysis by hypergeometric test and pathway topology analysis by relative betweenness centrality.

3.2.7 Study design

To account for biological variability, a total of N = 4 different V1 cells were analyzed in this study, each from a different embryo from a different clutch over a three-month period. For each cell, dual cationic–anionic analysis was performed in technical duplicate–triplicate.

3.2.8 Safety considerations

Standard safety procedures were followed when handling chemicals and biological samples. Capillary micropipettes and electrospray emitters, which pose a potential puncture hazard, were handled with gloves and safety goggles. To prevent against electrical shock hazard posed by high voltage, all electrically connective parts of the CE-ESI setup were earth-grounded and isolated in an enclosure equipped with a safety interlock-enabled door.

3.3 Results and discussion

3.3.1 Technology development

The goal of this study was to enhance the characterization of small polar metabolites in single cells, specifically in identified blastomeres directly in live embryos. We adapted *in situ* sampling by a microprobe to a microanalytical CE-ESI-MS platform to enable the metabolic analysis of single cells in *X. laevis* embryos.[55, 101] This approach allowed the detection of ~80 identified small polar metabolites and revealed quantitative metabolic changes as single cells divide to form cell clones in the 8–32-cell embryo.[55] However, microprobe CE-ESI-MS was restricted to cationic analysis due to frequent electrical breakdowns that destabilized the electrospray in the negative ion mode (ESI−). Theoretically, the standard metabolomics approach to perform independent analysis of cations and anions can deepen the detectable portion of the single-cell metabolome. However, two-step metabolite extraction is challenging or incompatible for single cells due to (i) the limited amounts of material that are available from a single cell and (ii) cell heterogeneity hindering the use of multiple cells, even from the same cell type, for sample processing.

Here, we addressed this technical limitation by enabling dual cationic–anionic characterization of the same single identified cell in live embryos using CE-ESI-MS. Our strategy (Fig. 3.1) extended microprobe single-cell sampling[55, 101] with essentially a one-pot microextraction of cationic and anionic metabolites and also advanced CE-ESI-MS detection for the negative ion mode (Fig. 3.2).

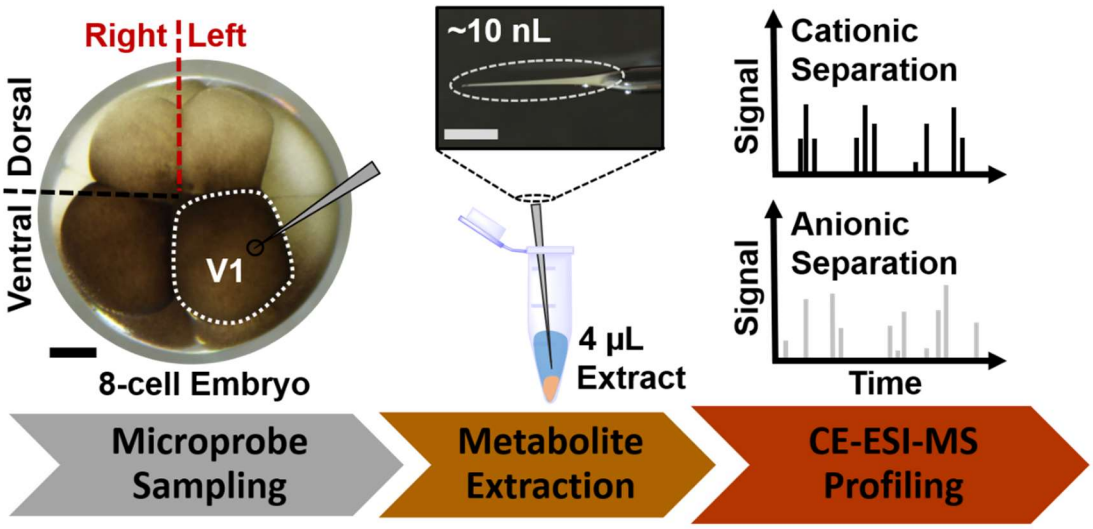

Figure 3.1 Microprobe CE-ESI-MS strategy to measure cationic and anionic metabolites from the same identified cell in a live *X. laevis* embryo. Scale bars = 250 µm. Reproduced from ref. 30 with permission from The Royal Society of Chemistry.

For technology development and validation, the left-ventral (V1) cell was used in 8-cell *X. laevis* embryos (see Fig. 3.1, left panel), which is considerably large (~500 µm in diameter, or ~180 nL in volume) to facilitate microprobe sampling and is readily identifiable based on pigmentation, location, and in reference to established cell-fate maps.[58, 133-135] An ~10 nL volume of the identified cell, corresponding to ~5% of the total cell volume, was withdrawn using a microfabricated capillary mounted to a three-axis translation stage following our recent protocol.[55, 101] The aspirate was ejected into 4 µL of 40% aqueous acetonitrile containing 40% methanol, which efficiently extracts small polar metabolites with different physicochemical properties, including acidity and polarity.[57] The resulting extract, containing cationic and anionic metabolites, thus raised a possibility for enhanced single-cell metabolomics in the embryo.

Anionic analysis required extension of cationic CE-ESI-MS to separation and detection of negatively charged metabolites. As an alternative to electron-scavenging reagents[136-140] or intricate CE-ESI interface designs,[26, 75, 112] we opted to refine our laboratory-built CE-ESI platform to stabilize electrospray operation in the negative ion mode. The setup, shown in Fig. 3.2A, builds on a coaxial sheath-flow interface that we[12, 55, 74] and others[14, 56, 65, 100, 141] extensively used for cationic analysis and recently nucleotide detection.[112] To minimize/eliminate electrical discharges upon negative ion-mode ESI, we enclosed the CE-ESI emitter tip in a lab-fabricated environmental chamber that was (optionally) purged with dry nitrogen gas at a controllable rate and incident flow angle with respect to the electrospray emitter (see "N2 bath gas"). The chamber was directly mounted on the atmospheric pressure interface of the mass spectrometer and featured a hole to allow fine-positioning of the CE-ESI emitter tip in the chamber in front of the orifice of the mass spectrometer inlet. Bidirectional illumination and a long-working distance stereomicroscope were implemented to monitor the stability of the electrospray.

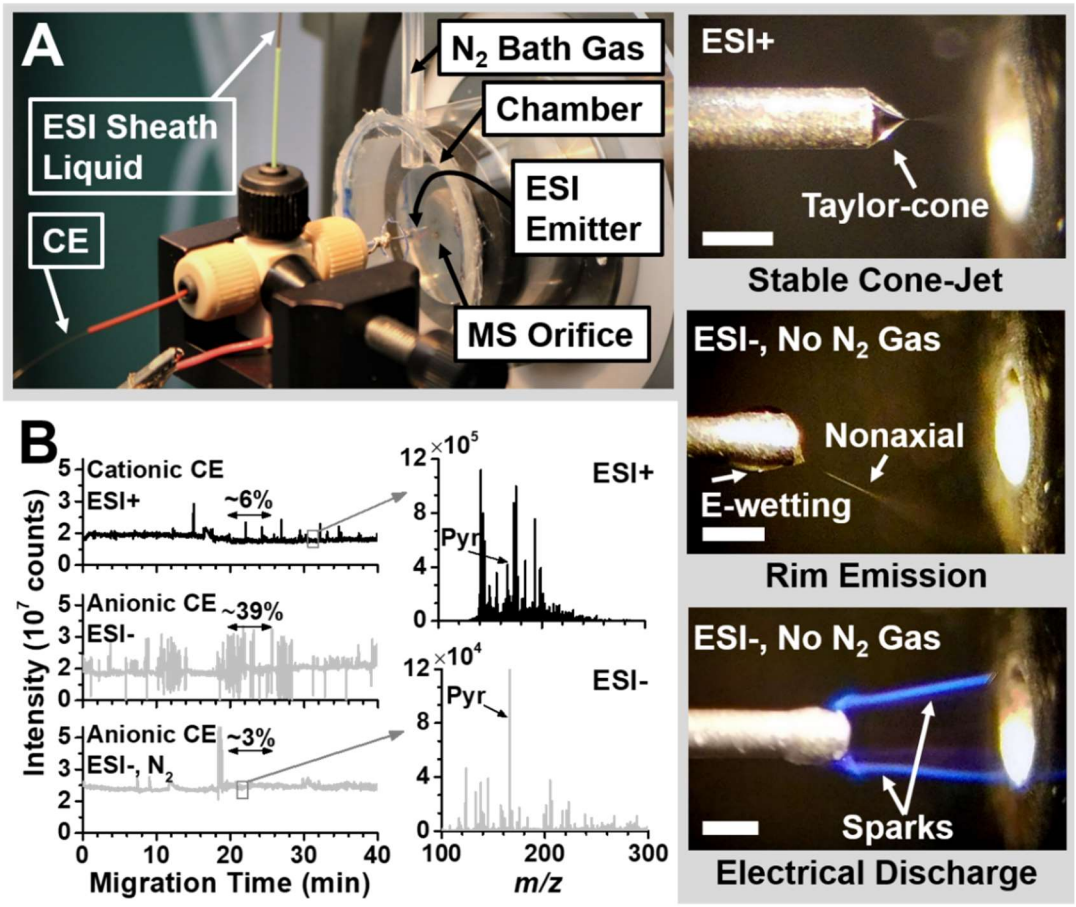

Figure 3.2 CE-ESI-MS for cationic and anionic analysis. (A) The CE-ESI-MS interface with major components labeled. Microscopy comparison of stable Taylor-cone in ESI+ (top panel) and nonaxial (rim) emission (middle panel) and electrical discharge (spark) in ESI- without nitrogen bath gas. Scale bar = 250 µm (B) Total ion chromatograms revealing stable operation during cationic separation with +ESI. Astable ESI– with anionic separation was stabilized upon enclosing the electrospray emitter in a nitrogen-filled environmental chamber. Spray stability is quantified as % relative standard deviation (RSD). Representative mass spectra of a V1 cell extract revealing simplified chemical background during ESI–. Pyr, pyridoxal. Reproduced from ref. 30 with permission from The Royal Society of Chemistry.

The stability of the CE-ESI-MS system was evaluated. The electro-hydrodynamic behavior of the liquid meniscus was monitored at the tip of the CE-ESI emitter using a stereomicroscope, while the temporal evolution of ion generation was

followed using the mass spectrometer. The operational modality of the electrospray was identified according to established nomenclature (reviewed in ref.[106, 142]) as follows (see examples in Fig. 3.2, right panel): a stable Taylor-cone with axial spray emission marked the cone-jet regime; a pulsating liquid meniscus with axial spray emission indicated the burst, astable, or pulsing regimes; non-axial spray emission was categorized as "rim emission" in this study. Agreeing with earlier studies (see ref.[100]), the CE-ESI interface yielded stable operation in the cone-jet regime under cationic experimental conditions (see Experimental) in air (no nitrogen bath gas used). Purging of the environmental chamber with a nitrogen bath gas (ambient temperature) at 0.4–1.0 L min^{-1} maintained stable operation with a variation of ~6% relative standard deviation (RSD) in total ion current (see Fig. 3.2, top panel). Therefore, the CE-ESI setup equipped with the environmental chamber still maintained robust performance for cationic analysis in this study.

The modified CE-ESI setup was tuned for robust anionic analysis. Electrospray polarity switching from cationic measurement conditions destabilized spray generation (data not shown), which worsened upon replacing the BGE with 20 mM bicarbonate, which was previously used for nucleotide analysis.[112] Encouraged by this study, we replaced the electrospray sheath solution with 200 μM ammonium bicarbonate in 20%, 50%, and 70% isopropanol to test electrospray stability in the negative ion mode. Although the temporal stability of ion generation improved using a 50% isopropanol solution (Fig. 3.2, middle panel), a ~39% RSD in the total ion chromatogram (TIC) in our hand revealed still pronounced fluctuation for quantification. Microscopy inspection of the emitter tip captured frequent

transitions between the pulsating (data not shown), rim (see Fig. 3.2 right panel, middle inset), and cone-jet electrospray regimes with occasional electrical sparks between the emitter tip and the MS orifice plate (see Fig. 3.2 right panel, bottom inset). These instabilities in electrostatic spraying and consequent ion generation ceased upon continuous purging of the environmental chamber with a steady-stream of nitrogen gas. After optimizing the nitrogen gas flow rate at 0.6 L min^{-1} and incidence perpendicularly to the electrospray emitter (see Fig. 3.2), the TIC stability was improved to only ∼3% RSD variation.

The cationic and anionic separations provided complementary analytical performance for detection. For several metabolite standards (e.g., creatine, lysine), quantification was tested to be linear between ∼100 nM and ∼1 μM (regression coefficient, $R2 > 0.99$) in both modalities, which the digitizer of the mass spectrometer is expected to extend to an ∼4-log-order dynamic range following our recent study.[12] Based on the analysis of a 100 nM creatine standard, the lower limit of detection was extrapolated to 7.5 nM (75 amol) during cationic and 5.5 nM (55 amol) during anionic analysis. Furthermore, mass spectra resulting from anionic measurements contained substantially fewer background ions, which also had lower ion intensities, suggesting minimized spectral interferences compared to cationic analysis. Fig. 3.2 exemplifies detection of the pyridoxal anion from a V1 cell extract at a ∼3 : 1 analyte : background signal ratio (average ESI−) in a sparsely populated spectrum, whereas the cation of this metabolite yielded a ∼1 : 3 ratio in a complex mass spectrum from the same cell extract. These analytical figures of merit suggested a potential for sequential cationic and anionic profiling of the same metabolite extract

using the same CE-ESI-MS instrument, which we refer to as "dual cationic–anionic" measurement in this report.

3.3.2 Dual cationic-anionic metabolomics of single cells

We applied these methodologies to characterize small metabolites in N = 4 single V1 cells (recall Fig. 1). As described earlier, an ~10 nL portion of the cell was aspirated *in situ* from a live 8-cell *X. laevis* embryo using a pulled microcapillary. Small metabolites were extracted from the aspirate in 4 μL of 40% acetonitrile containing 40% methanol. An ~10 nL portion of the resulting extract was analyzed under cationic and then anionic conditions using the same CE-ESI-MS setup and different BGEs. Data-dependent tandem MS was performed to facilitate metabolite identifications. These measurements, thus, consumed a total of ~20 nL, viz. ~0.5% of metabolites that were extracted from the V1 cell. Our recent findings using microsampling[55] suggests that microprobe CE-ESI-MS with dual cationic–anionic analysis is scalable to smaller cells and later stages of the developing embryo as well as other tissues and organisms.

These data provide rich metabolic information on the cell. After deisotoping and manual annotation of the MS data, we found ~250 cationic and ~200 anionic nonredundant molecular features between m/z 50–550. These numbers excluded non-covalent clusters as well as signals that originated from the extraction solvents or the culturing media (e.g., polymers from vials and salt peaks). Metabolite identifications were made for 60 cationic and 24 anionic molecular features (Table 3.1) based on accurate mass, isotopic peak distribution analysis, tandem MS, and comparison to

MS-MS/MS data recorded on chemical standards, in our previous studies,[12, 55, 57, 74] or published in Metlin[43] and MzCloud (http://www.mzcloud.org).

Table 3.1 Metabolites identified by cationic–anionic microprobe CE-ESI-MS.

Positive ion mode

ID	Metabolite	Formula	Time (min)	m/z measured	m/z theoretical	Δm/z (mDa)	Δm/z (ppm)
1	Spermidine (SPM)**	$C_7H_{19}N_3$	15.5	146.1663	146.1652	–1.1	–7.5
2	Thiamine**	$C_{12}H_{16}N_4OS$	17.8	265.1114	265.1118	0.4	1.4
3	Choline (Cho)*,**	$C_5H_{13}NO$	18.6	104.1068	104.1070	0.2	1.9
4	Arg-Ala (RA)**	$C_9H_{19}N_5O_3$	19.3	246.1570	246.1561	–0.9	–3.8
5	Lys-Ser (KS)**	$C_9H_{19}N_3O_4$	19.3	234.1434	234.1448	1.4	6.1
6	Val-Lys (VK)**	$C_{11}H_{23}N_3O_3$	19.6	246.1805	246.1812	0.7	2.9
7	S-adenosyl-methionine (SAM)**	$C_{15}H_{22}N_6O_5S$	19.6	399.1430	399.1445	1.5	3.8
8	Ser-Arg (SR)**	$C_9H_{19}N_5O_4$	19.6	262.1511	262.1510	–0.1	–0.4
9	Ornithine (Orn)**	$C_5H_{12}N_2O_2$	19.8	133.0973	133.0972	–0.1	–0.8
10	Lysine (Lys)*,**	$C_6H_{14}N_2O_2$	20.0	147.1132	147.1128	-0.4	-2.7
11	Arginine (Arg)*,**	$C_6H_{14}N_4O_2$	20.4	175.1193	175.1190	–0.3	–2.0
12	Homolysine**	$C_7H_{16}N_2O_2$	20.4	161.1287	161.1285	–0.2	–1.5
13	Tyr-Lys (YK)**	$C_{15}H_{23}N_3O_4$	20.4	310.1749	310.1761	1.2	4.0
14	γ-aminobutyric acid (GABA)*,**	$C_4H_9NO_2$	20.5	104.0707	104.0706	–0.1	–0.9
15	N6,N6,N6-trimethyl-lysine (TML)**	$C_9H_{20}N_2O_2$	20.5	189.1599	189.1598	–0.1	–0.8
16	Histidine (His)*,**	$C_6H_9N_3O_2$	20.5	156.0774	156.0768	–0.6	–4.1
17	Methylhistidine**	$C_7H_{11}N_3O_2$	20.7	170.0928	170.0924	–0.4	–2.3
18	Guanidinopropanoate**	$C_4H_9N_3O_2$	20.8	132.0761	132.0768	0.7	4.9
19	Acetylcholine (AcCho)*,**	$C_7H_{15}NO_2$	20.8	146.1177	146.1176	–0.1	–1.0
20	Leu-Ala (LA)**	$C_9H_{18}N_2O_3$	22.0	203.1388	203.1390	0.2	1.1
21	Cis-urocanate (cURA)**	$C_6H_6N_2O_2$	22.2	139.0500	139.0502	0.2	1.4
22	Guanine**	$C_5H_5N_5O$	22.3	152.0572	152.0567	–0.5	–3.4
23	Carnitine (Car)*,**	$C_7H_{15}NO_3$	22.8	162.1131	162.1125	–0.6	–3.9
24	Trans-Urocanate (tURA)**	$C_6H_6N_2O_2$	23.0	139.0500	139.0502	0.2	1.4
25	Methylguanine**	$C_6H_7N_5O$	23.3	166.0726	166.0723	–0.3	–1.8
26	Pyridoxal**	$C_8H_9NO_3$	23.4	168.0659	168.0655	–0.4	–2.3

ID	Metabolite	Formula	Time (min)	m/z measured	m/z theoretical	Δm/z (mDa)	Δm/z (ppm)
27	Acetylcarnitine (AcCar)[**]	$C_9H_{17}NO_4$	24.5	204.1231	204.1230	–0.1	–0.3
28	Methylaspartate[**]	$C_5H_9NO_4$	25.4	148.0605	148.0604	–0.1	–0.4
29	Glycine[*]	$C_2H_5NO_2$	25.3	76.0386	76.0393	0.7	9.3
30	Niacinamide[*]	$C_6H_6N_2O$	25.4	123.0549	123.0553	0.4	3.2
31	Creatine (CR)[*,**]	$C_4H_9N_3O_2$	25.6	132.0779	132.0768	–1.1	–8.7
32	Pro-Val (PV)[**]	$C_{10}H_{18}N_2O_3$	25.8	215.1378	215.1390	1.2	5.7
33	Alanine (Ala)[*]	$C_3H_7NO_2$	27.4	90.0548	90.0550	0.2	1.7
34	Argininosuccinate (ASA)[**]	$C_{10}H_{18}N_4O_6$	28.5	291.1292	291.1299	0.7	2.4
35	Valine (Val)[*,**]	$C_5H_{11}NO_2$	30.5	118.0864	118.0863	–0.1	–1.2
36	Serine (Ser) [*,**]	$C_3H_7NO_3$	30.6	106.0498	106.0499	0.1	0.7
37	Isoleucine[*,‡]	$C_6H_{13}NO_2$	30.7	132.1023	132.1019	–0.4	–3.0
38	Leucine[*,‡]	$C_6H_{13}NO_2$	31.0	132.1023	132.1019	–0.4	–3.0
39	Asparagine (Asn)[**]	$C_4H_8N_2O_3$	32.1	133.0610	133.0608	–0.2	–1.7
40	Threonine (Thr)[*,**]	$C_4H_9NO_3$	32.1	120.0654	120.0655	0.1	1.0
41	Tryptophan (Trp)[*,**]	$C_{11}H_{12}N_2O_2$	32.6	205.0967	205.0972	0.5	2.2
42	Methionine (Met)[*,**]	$C_5H_{11}NO_2S$	32.7	150.0588	150.0583	–0.5	–3.2
43	Glutamine (Gln)[**]	$C_5H_{10}N_2O_3$	32.8	147.0769	147.0764	–0.5	–3.3
44	2-Aminoadate[**]	$C_6H_{11}NO_4$	32.9	162.0767	162.0761	-0.6	-3.8
45	Acetylhomoserine[†]	$C_6H_{11}NO_4$	32.9	162.0767	162.0761	–0.6	–3.8
46	Citrulline (Cit)[**]	$C_6H_{13}N_3O_3$	33.1	176.1027	176.1030	0.3	1.5
47	Homocitrulline[**]	$C_7H_{15}N_3O_3$	33.2	190.1178	190.1186	0.8	4.3
48	Glutamic acid (Glu)[**]	$C_5H_9NO_4$	33.2	148.0610	148.0604	–0.6	–3.8
49	Phenylalanine (Phe)[**]	$C_9H_{11}NO_2$	33.7	166.0867	166.0863	–0.4	–2.7
50	Acetyllysine[†]	$C_8H_{16}N_2O_3$	34.0	189.1219	189.1234	1.5	7.8
51	Tyrosine (Tyr)[*,**]	$C_9H_{11}NO_3$	34.1	182.0813	182.0812	–0.1	–0.7
52	Hypoxanthine (HPX)[**]	$C_5H_4N_4O$	34.3	137.0461	137.0458	–0.3	–2.3
53	Proline (Pro)[*,**]	$C_5H_9NO_2$	34.6	116.0707	116.0706	–0.1	–0.8
54	Ser-Val (SV)[†]	$C_8H_{16}N_2O_4$	34.9	205.1181	205.1183	0.2	0.9
55	Cysteine[*,**]	$C_3H_7NO_2S$	35.8	122.0269	122.0270	0.1	1.0
56	Aspartic acid[*,**]	$C_4H_7NO_4$	36.0	134.0451	134.0448	–0.3	–2.4
57	Glycine betaine (GB) [*,‡]	$C_5H_{11}NO_2$	36.6	118.0864	118.0863	–0.1	–1.2
58	Glutathione, oxidized (GSSG)[**]	$C_{20}H_{32}N_6O_{12}S_2$	37.2	307.0826	307.0833	0.7	2.1

ID	Metabolite	Formula	Time (min)	m/z measured	m/z theoretical	Δm/z (mDa)	Δm/z (ppm)
59	Hydroxyproline (Hyp)**	$C_5H_9NO_3$	38.3	132.0660	132.0655	–0.5	–3.6
60	Glutathione (GSH)*,**	$C_{10}H_{17}N_3O_6S$	40.0	308.0908	308.0911	0.3	0.9
Negative ion mode							
1	Arginine (Arg)**	$C_6H_{14}N_4O_2$	11.3	173.1027	173.1033	0.6	3.5
2	Lysine (Lys)**	$C_6H_{14}N_2O_2$	13.9	145.0958	145.0971	1.3	9.2
3	Glutamine (Gln)**	$C_5H_{10}N_2O_3$	15.1	145.0605	145.0608	0.3	2.3
4	Glucose*,**	$C_6H_{12}O_6$	16.4	179.0555	179.0550	–0.5	–2.8
5	Asparagine (Asn)**	$C_4H_8N_2O_3$	17.3	131.0461	131.0451	–1.0	–7.6
6	Creatine (CR)**	$C_4H_9N_3O_2$	17.6	130.0613	130.0609	–0.4	–3.1
7	Phenethoxybenzamid - oxopentanoic Acid**	$C_{19}H_{19}N_3O_7$	19.9	400.1150	400.1139	–1.1	–2.8
8	Phosphorylcholine**	$C_4H_{12}NO_4P$	20.5	168.0413	168.042	0.7	4.3
9	Pyridoxal**	$C_8H_9NO_3$	20.8	166.0519	166.0498	–2.1	–12.6
10	Aspartic acid (Asp)**	$C_4H_7NO_4$	24.8	132.0287	132.0291	0.4	3.3
11	Phosphoylethanolamine**	$C_2H_8NO_4P$	28.2	140.0115	140.0107	–0.8	–5.7
12	Glyceric acid**	$C_3H_6O_4$	31.3	105.0191	105.0182	–0.9	–8.6
13	Guanine**	$C_5H_5N_5O$	31.9	150.0415	150.041	–0.5	–3.3
14	Pantothenic Acid**	$C_9H_{17}NO_5$	32.0	218.1044	218.1023	–2.1	–9.6
15	Cytidine phosphate (CMP)**	$C_9H_{14}N_3O_8P$	38.4	322.0462	322.0434	–2.8	–8.7
16	Adenine**	$C_5H_5N_5$	38.7	134.0482	134.0461	–2.1	–15.7
17	Pyridoxic acid (PHOS)**	$C_8H_9NO_4$	39.7	182.0472	182.0447	–2.5	–13.7
18	Glutamate (Glu)**	$C_5H_9NO_4$	40.4	146.0472	146.0456	–1.6	–11.0
19	Uridine monophosphate**	$C_9H_{13}N_2O_9P$	40.9	323.0301	323.0274	–2.7	–8.4
20	Hypoxanthine (HPX)**	$C_5H_4N_4O$	45.4	135.0311	135.0301	–1.0	–7.4
21	Phosphocreatine**	$C_4H_{10}N_3O_5P$	53.4	210.0276	210.0274	–0.2	–1.0
22	Alanine (Ala)**	$C_3H_7NO_2$	53.6	88.0405	88.0393	–1.2	–13.6
23	Guanidinopropanoate**	$C_4H_9N_3O_2$	53.9	130.0613	130.0611	–0.2	–1.5
24	Glucose phosphate**	$C_6H_{13}O_9P$	62.0	259.0234	259.0214	–2.0	–7.7

Note: Asterisk (*) signifies identification based on migration-time. Double asterisk (**) denotes identification by tandem mass. Dagger (†) indicates that tandem mass spectrum agrees with molecular fragmentation predicted in Mass Frontier 7.0 (Thermo Fisher). Double dagger (‡) indicates mass-match in Metlin.

Cationic and anionic measurements complemented each other. There were noticeable differences between CE separation performance. Fig. 3.3 presents representative extracted ion electropherograms for a subset of identified metabolites from V1 cells. Although most metabolites were separated in a shorter amount of time during cationic analysis, anionic separation provided higher separation efficiency: the average number of theoretical plates (N) was ~170,000 for cationic and ~200,000 for anionic analyses. These separation performances compare favorably to other CE-ESI designs, including recent low-flow coaxial (N = 15 000 plates per m)[26] and sheathless (N = 40 000–60 000 plates per m)[75] porous tip sprayer with high-sensitivity detection.

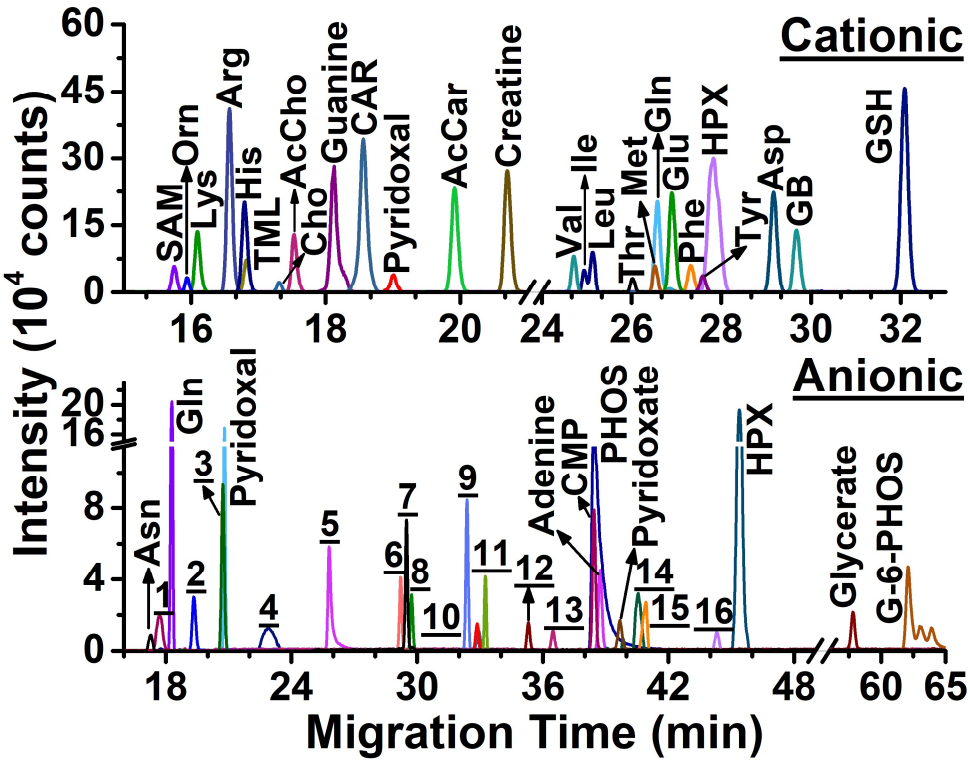

Figure 3.3 Cationic and anionic profiling of metabolites in the same V1 cell in a live *X. laevis* embryo. Reproduced from ref. 30 with permission from The Royal Society of Chemistry.

Additionally, metabolite identifications were also complementary (Fig. 3.4). Molecular assignments were made for 60 cations and 24 anions with 11 metabolites identified under both conditions (Fig. 3.4A). Detection performance was compared based on signal-to-noise (signal/noise) ratios that were calculated for these 11 metabolites (Fig. 3.4B). The results revealed similar sensitivity for alanine, glutamine, glutamic acid, lysine, and pyridoxal. Cationic analysis yielded higher sensitivity for arginine, creatine, guanine, and hypoxanthine, whereas anionic analysis was more sensitive for asparagine and aspartic acid. Therefore, differences in complementary separation performance and compound-dependent ionization translated into quantitative differences using the cationic and anionic methodologies.

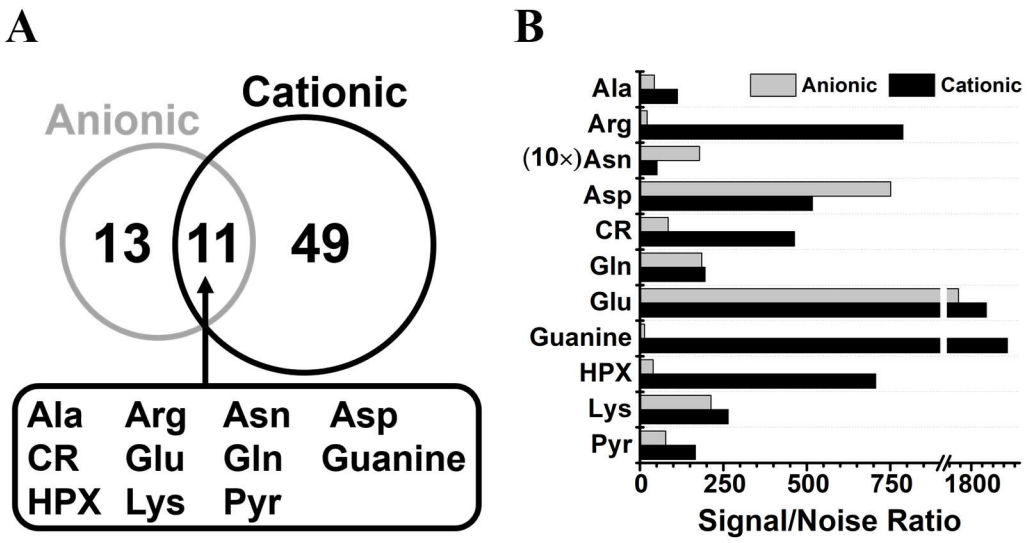

Figure 3.4 Complementary (A) identification and (B) quantification of metabolites in single *Xenopus laevis* V1 cells using dual cationic–anionic microprobe CE-ESI-MS. Key: Cr, creatine; HPX, hypoxanthine; Pyr, pyridoxal. Reproduced from ref. 30 with permission from The Royal Society of Chemistry.

The identified metabolites enabled pathway enrichment analysis. Metabolites that were identified by cationic, anionic, and dual cationic–anionic analyses were mapped to the KEGG metabolomic knowledgebase using MetaboAnalyst as the search engine (see details in Experimental). Pathway significance was calculated from pathway enrichment analysis, and pathway impact was determined from pathway topology analysis. Fig. 3.5 plots pathway significance vs. pathway impact from dual anionic–cationic analysis. Several pathways were enriched to statistical significance ($p < 0.05$) with pathway impact varying between high (>0.5), modest (0.2–0.5), and low (<0.2). Representative metabolic pathways are labeled in Fig. 3.5 (top panel). For example, arginine–proline and glycine–serine–threonine metabolism were of high impact, whereas enrichment was modest for vitamin B6 metabolism and low for glycero-phospholipid metabolism.

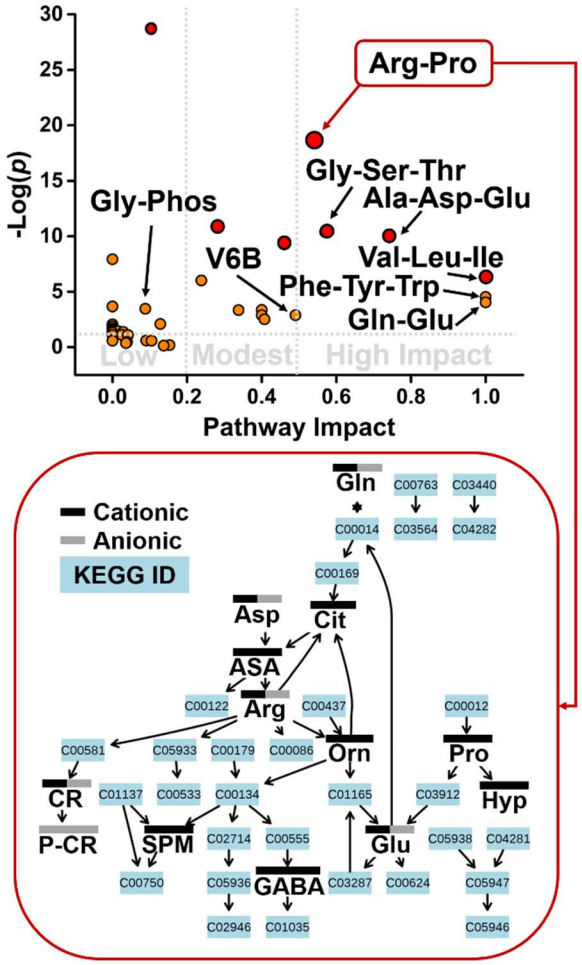

Figure 3.5 KEGG pathway analysis for metabolites identified in single V1 cells. Values of statistical significance (p) and impact are shown for labeled pathways in Table 3.1. Pathway view for arginine–proline metabolism marking complementary detection by cationic and anionic analyses. ASA, argininosuccinate; Cit, citrulline; CR, creatine; Gly-Phos, Glycero-phospholipid metabolism; Hyp, hydroxyproline; P-CR, phosphocreatine; SPM, spermidine; V6B, vitamin 6B metabolism. Reproduced from ref. 30 with permission from The Royal Society of Chemistry.

Furthermore, anionic and cationic analyses provided complementary information for pathway analysis. Table 3.2 compares pathway enrichment and pathway impact based on metabolites that were identified during the cationic, anionic, and dual cationic–anionic measurements. Cationic and anionic analyses appeared to

cover several pathways of high impact, including alanine–aspartate–glutamate, arginine–proline, and glutamine–glutamate. The complementarity of cationic and anionic detection is illustrated for the arginine–proline pathway in Fig. 3.5 (bottom panel). Notably, additional metabolite identifications that resulted from dual cationic–anionic analysis helped improve statistical significance and/or pathway impact for several pathways, including glycerophospholipid and vitamin B6 metabolism (see Table 3.2). Combined, these results demonstrate that dual cationic–anionic analysis by microprobe single-cell CE-ESI-MS provide deeper coverage of metabolism than feasible by these approaches in isolation.

Table 3.2 KEGG pathway analysis (statistical p-value and pathway impact) for metabolites identified in single V1 cells by microprobe CE-ESI-MS.

Name of Metabolic Pathway	Total	Cationic Analysis			Anionic Analysis			Dual Analysis		
		Hits	p	Impact	Hits	p	Impact	Hits	p	Impact
Alanine, aspartate, glutamate	24	7	1.06E-05	0.74	5	3.24E-05	0.60	7	4.34E-05	0.74
Arginine, proline	43	12	7.33E-09	0.54	7	3.57E-06	0.23	13	8.17E-09	0.54
Glutamine, glutamate	5	2	1.12E-02	1.00	2	2.27E-03	1.00	2	1.75E-02	1.00
Glutathione	26	7	1.91E-05	0.46	1	0.36	0.03	7	7.69E-05	0.46
Glycero-phospholipid	28	2	0.265	0.03	2	0.081	0.06	4	0.032	0.09
Glycine, serine, threonine	31	7	6.66E-05	0.57	2	0.10	0.00	8	3.14E-05	0.57
Histidine	14	4	1.12E-3	0.24	2	2.26E-02	0.00	4	2.25E-03	0.24
Nitrogen	9	4	1.61E-4	0.00	2	9.45E-3	0.00	4	3.64E-4	0.00
Phenylalanine, tyrosine, tryptophan	4	2	7.21E-03	1.00	0	0	0.00	2	7.21E-03	1.00
Valine, leucine, isoleucine	13	4	8.21E-04	1.00	0	0	0.00	4	8.21E-04	1.00
Vitamin B6	9	1	0.281	0.49	1	0.145	0.00	2	0.056	0.49

3.4 Conclusions

In this study, we advanced CE-ESI-MS technology to enable dual cationic–anionic analysis of metabolites in single embryonic cells. *In situ* microprobe sampling using a microfabricated capillary allowed us to sample an identified cell directly in a live *X. laevis* embryo under optical guidance by a stereomicroscope. To analyze metabolites extracted from the collected cell content, we equipped an in-house built CE-ESI-MS[12] platform with dual capability to perform cationic and anionic analysis using different BGEs for separation, without modifying the setup between sequential measurements. Optimization of experimental variables and the use of a nitrogen bath gas to minimize/eliminate electrical breakdown upon negative electrospray ensured sufficiently reproducible and robust operation for single-cell investigations in trace sensitivity (~5 nM, viz. ~50 amol demonstrated here).

The approach affords analytical benefits for biological studies on single cells. *In situ* microprobe sampling is compatible with complex tissues and organisms, as we demonstrated for 8-cell embryos of *X. laevis* in this work. CE-ESI-MS consumes sufficiently small amounts of extracts to afford multiple analysis of the same extract under cationic and anionic conditions. With complementary performance, the metadata resulting from these approaches improved metabolite identifications and quantification, which in turn led to better coverage of metabolic networks in single cells. This study design complements earlier works in which bare fused or coated capillaries were used to deepen metabolic coverage. Further improvements in detection sensitivity and expansion of metabolomic MS–MS/MS databases are needed to help identification of molecular features that were detected from the single

cells. Combined, results from this study and recent works[12, 55, 100, 112] suggest that dual cationic–anionic microprobe CE-ESI-MS is scalable to smaller cells and other types of cells and organisms to understand cell biology at the level of small molecules: the metabolome.

Chapter 4: Uncovering metabolic pathways underlying cell fate commitment during early embryonic development

Based on material in preparation for submission by Erika P. Portero, Aleena J. Andrews, and Peter Nemes*.

4.1 Introduction

The study of molecular mechanisms underlying cell and tissue differentiation is essential to enhance our understanding of normal and impaired development. Characterization of the biochemical state of individual cells in the organism provides a powerful descriptor of cell heterogeneity,[64, 143] as a single-cell differentiates to form specific tissues and organs. For example, emerging information from human, mouse, and frog (*X. laevis*) embryonic stem cells suggests the implication of metabolic reactions during key developmental processes including cell differentiation,[144-146] cell fate commitment,[12] morphogenesis, and organ formation.[147-148] In fact, the metabolome provides fast and dynamic feedback to intrinsic and extrinsic events, offering a unique look into the phenotypical and physiological state of the cell.[64] Mass spectrometry (MS) offers unbiased label-free detection and quantitation of metabolites with high sensitivity and selectivity. Particularly, single-cell MS provides a significant improvement over contemporary large-scale cell pooling analysis since it eliminates signal averaging that can interfere with the identification of cell-to-cell variability.

A subset of single-cell MS technologies utilizes chemical separation prior to ionization to reduce chemical interference and effectively extend the detectable

coverage of the single-cell metabolome.[12, 29, 55, 70, 149-150] By combining cell dissection, microprobe sampling, and single-cell CE-ESI-MS, the Nemes lab recently revealed spatial and temporal metabolic heterogeneity among single cells of the *X. laevis* embryo,[12, 55, 57] and uncovered metabolites that can alter dorsal–ventral cell commitment.[12] Although dorsal and ventral cell types in the 16-cell embryo present characteristic metabolic profiles; the fundamental molecular mechanisms that link metabolites and cell fate commitment remain unspecified.

To help address this knowledge gap, I applied a stable isotope labeling (SIL) approach to elucidate dynamic metabolism in developing embryonic cells of the *Xenopus laevis*. Stable isotope labeling has demonstrated to be a useful tool to study metabolic flux and pathway discovery in systems biology.[151-153] Since metabolic fluxes are considered an endpoint of cellular regulation and are likely to reflect changes on the transcriptome and proteome, it has become a valuable read-out in many areas of biology, including biomedicine and bioengineering.[154-155] Isotopic labeling patterns are also known to be a direct consequence of metabolic fluxes; thus, changes in labeling pattern indicate metabolic flux changes. The use of isotope tracers (e.g., ^{13}C-glucose, ^{13}C-amino acids, etc.) provides valuable information on the dynamics of downstream metabolite labeling, enabling the study of metabolic pathways. Recently, stable isotope labeling and liquid chromatography (LC)-MS on whole *X. laevis* embryos revealed the remodeling of core metabolic pathways during early cleavage stages by tracking the consumption of neutron-enriched (heavy labeled) alanine and aspartate in the Krebs cycle.[13] However, the analysis of whole embryos also uncovered significant differences in metabolite abundance (e.g.,

alanine, proline) between embryos, emphasizing the importance of a single-cell analysis to avoid embryo-to-embryo variability.

This chapter describes the development of a single-cell metabolomics workflow combining stable isotope labeling and microprobe CE-ESI-MS to uncover dynamic metabolic pathways from targeted dorsal and ventral offspring cells, also referred to as clones, at the early stages of embryonic development. This strategy investigates metabolism of dorsal and ventral clones from the 16-cell stage to stage 9 at the mid-blastula transition. Next, I applied this approach to identify temporal changes of the metabolome of dorsal and ventral clones after microinjecting select metabolites known to alter cell fate commitment in the 16-cell *X. laevis* embryo. The presented work identified metabolic pathways that respond to metabolite concentration changes, and the rapid rearrangement of the metabolome that ultimately leads to tissue fate alterations of dorsal and ventral clones.

4.2 Experimental

4.2.1 Chemicals and reagents

Chemicals. LC-MS-grade solvents including acetonitrile, methanol, and water as well as formic acid, phosphate buffered saline (PBS, 10X) solution, and Alexa Fluor Dextran 488 (FD) were purchased from Fisher Scientific (Fair Lawn, NJ). Ficoll PM 400, 13C4,15N-L-threonine (Thr*), and 13C5,15N-L-methionine (Met*) were from Sigma-Aldrich (Saint Louis, MO). L-methionine (Met), L-serine (Ser), D-threonine (Thr), and acetylcholine chloride (ACh) were from Acros Organics (Fair Lawn, NJ). Cysteine, diethyl pyrocarbonate (DEPC), and paraformaldehyde were

from MP Biomedicals (Solon, OH). Capillaries. For sample collection, borosilicate capillaries (0.5/1.0 mm inner/outer diameter, part no. B100-50-10, Sutter Instrument Co., Novato, CA) were pulled to barrel length ~800 µm in a capillary puller (model P-1000, Sutter Instruments Co., Novato, CA). For capillary electrophoresis (CE), fused silica capillaries (40/104 µm inner/outer diameter) were from Polymicro Technologies, Phoenix, AZ and used as received. CE capillaries were conditioned prior to use with 100 mM sodium hydroxide. As the emitter for electrospray source, a platinum alloy emitter (0.0055" inner diameter and 0.003" wall, part no. 29910E, Johnson Matthey Inc., West Chester, PA) was used. GFP Plasmid and mRNA. In vitro transcription kit (part no. AM1348, ThermoFisher Scientific, Waltham, MA) and plasmid containing open-reading frame for green fluorescent protein (pCS2+).

4.2.2 Solutions

Biology. Steinberg's solution (SS), 2% cysteine, 3% Ficoll, and 4% paraformaldehyde in PBS solutions were prepared following standard protocols.[126] All solutions and media that were used to culture embryos or to perform cell injections were prepared with DEPC-treated and autoclave-sterilized deionized. Cell fates were traced using 0.5% (v/v) FD in DEPC-treated water. Chemistry. The metabolite "*extraction solvent*" comprised of 40% acetonitrile and 40% methanol in LC-MS grade water (pH 4.7), chilled at 4 °C, chosen to stabilize the metabolome by minimizing/eliminating metabolic degradation.[12, 57, 100] For CE, the background electrolyte was 1% formic acid (pH 2.8). For electrospray ionization (ESI), the

"*sheath liquid*" was 0.1% formic acid in 50% methanol prepared in LC-MS grade water.

4.2.3 Animals and embryo collection

All protocols related to the maintenance and humane handling of animals were approved by the University of Maryland Institutional Animal Care and Use Committee (IACUC no. R-DEC-17-57). Adult male and female *Xenopus laevis* frogs were purchased from Nasco (Fort Atkinson, WI) and maintained in a breeding colony. Fertilized embryos were obtained via gonadotropin-induced natural mating of adult frogs. The jelly coating surrounding freshly laid embryos was removed using a 2% cysteine solution following established protocols.[126] Dejellied embryos were transferred to Petri dishes containing 100% SS and examined under a stereomicroscope. To enable accurate cell type identification in this study, 2-cell embryos showing stereotypical pigmentation patterns[134] across the left-right axis were isolated into a separate Petri dish and cultured in 100% SS at 21 °C temperature. Developmental staging followed the Nieuwkoop-Faber[156] nomenclature.

4.2.4 Cell fate tracking and metabolite injections

Individual 2-cell *X. laevis* embryos were monitored under a stereomicroscope until they reached the 16-cell stage, then transferred to a Petri dish containing 3% ficoll in 100% SS. In the 16-cell embryo, the midline dorsal-animal (D11) and the midline ventral-animal (V11) cells were identified following established cell fate maps.[58, 135] As controls in this study, the dorsal and ventral cell clones were labeled by expressing the green fluorescent protein in the identified precursor cell. The left

D11 cells (N = 78) or the left V11 cells (N = 44) were injected with 2 nL of 100 pg/nL GFP mRNA using a microinjector station. A microscope (model SMZ 1270, Nikon, Melville, NY) was employed to identify the cell type and position using a three-axis micromanipulator (TransferMan 4r, Eppendorf, Hauppauge, NY) the tip of the pulled borosilicate capillary (~10 μm inner diameter) into the cell. The capillary was connected to a microinjector (model PLI-100A, Warner Instrument, Handem, CT) delivering a pressure pulse (40 psi for 0.9 s), which in turn delivered the required volume.[157]

The experimental groups consisted of metabolite-perturbed clones of D11 and V11. To study the effect of metabolites on the dorsal clone, the identified D11 cell was injected with 2 nL of metabolite mixture of the following composition in DEPC-treated water: 7.5 mM ACh and 100 pg/nL GFP mRNA (N = 81); 75 mM Met and 100 pg/nL GFP mRNA (N = 72); 7.5 mM ACh, 75 mM Met, and 100 pg/nL GFP mRNA (N = 91); or 40 mM Thr* with 100 pg/nL GFP mRNA (N = 67). Similarly, the effect of metabolite perturbation was evaluated on the ventral clone by injecting the identified V11 cell with 2 nL of metabolite mixture containing following: 75 mM Thr and 100 pg/nL GFP mRNA (N = 49); 75 mM Ser and 100 pg/nL GFP mRNA (N = 57); 75 mM Thr, 75 mM Ser, and 100 pg/nL GFP mRNA (N = 61); or 60 mM Met* and 100 pg/nL GFP mRNA (N = 49). Approximately 20 min after the injection, the embryos were transferred into Petri dishes containing 50% SS and cultured at 14 °C to the larval stage. Stage 34 larvae were fixed in 4% paraformaldehyde and 3% sucrose in PBS for 1 h. The fixed larvae were rinsed with 1× PBS and stored at 4 °C until fluorescent imaging and scoring.

4.2.5 Phenotyping

The larvae were imaged under bright-field and epifluorescence on a research-grade stereomicroscope (model SMZ18 equipped with SMZ-25/18 P2-EFLC EGFP BP HC Filter Set, Nikon, Melville, NY). The relative size of the cell clones in each tissue of interest were assessed in stage 34 larvae following established cell fate maps.[58, 135] Criteria for scoring were as follows: "0" was assigned to mark no labeled cells in the tissues of interest; "1" was assigned to indicate ≤ 10 labeled cells in the tissue of interest; "5" was assigned when at least 50% of the cells in the tissue were labeled; and "10" was assigned for tissues entirely labeled by fluorescent cells. To eliminate inter-personal biases during scoring, the same person performed all the phenotyping through this study.

4.2.6 Stable isotope labeling of dorsal and ventral clones

Metabolic perturbation as dorsal-ventral clones switched tissue fate was reported using an isotopologue of endogenously enriched threonine in the D11 cell and methionine in the V11 cell, viz. in the 16-cell embryo. To enhance detection sensitivity by allowing for metabolic incorporation, the precursor cell of the clone was injected with the heavy isotope at an early stage, viz. at the 4-cell stage. After culturing the embryo to the 16-cell stage in 3% Ficoll in 100% SS, metabolic perturbation was introduced with co-injection into the cell with the dye FD. Therefore, to study dorsal-to-ventral fate change in the D11 cell upon Met injection, the left D cell (4-cell embryo) was injected with 2 nL of 40 mM Thr* and the descendent left D11 cell was injected with 2 nL of Met and FD (75 mM Met in 0.5%

FD). Conversely, to study ventral-to-dorsal fate change in the V11 cell upon Thr injection, the left V cell (4-cell embryo) was injected with 2 nL of 60 mM Met*, and the offspring left V11 cell was injected with 2 nL Thr and FD (75 mM Thr in 0.5% FD). The resulting embryos were cultured at room temperature in 50% SS to the cleavage (32 or 64 cells) or blastula (stages 8 or 9) stages.

4.2.7 Sample preparation

The fluorescently labeled clones (FD) were visualized under the fluorescence stereomicroscope. The sample collection (sampling) approach was tailored to corresponding developmental stages. In the cleavage stage embryos (32- and 64-cell), where cells are considerably large, an ~10–15 nL volume of the D11 (N = 3) or V11 (N = 3) clone were aspirated using a fabricated microprobe (~20 μm outer diameter) following our established protocol.[55, 101] Metabolites from the collected cell content were extracted in 4 μL of metabolite extraction solvent (4 °C) in a microvial. The microprobe was replaced for each sampling event to avoid cross-contamination. For mid-blastula stage 8 (N = 3) or stage 9 (N = 3), the protective vitelline membrane was carefully peeled off and the fluorescent clones dissected using sharp forceps under guidance by the stereomicroscope.[12] Metabolites were extracted from the collected tissues in 10 μL of metabolite extraction solvent (4 °C). Vials containing the cell extracts from the cleave- and blastula-stage embryos were vortex-mixed for ~1 min at room temperature to facilitate lysis and extraction and centrifuged for 5 min at 8,000 × g at 4 °C to pellet cell debris. The resulting extracts were kept together with the cell debris to avoid sample losses and stored at −80 °C until analysis by CE-ESI-MS.

4.2.8 CE-ESI-MS platform

Metabolite extracts were analyzed using a home-built microanalytical CE electrospray ionization (ESI) platform coupled to a commercial high-resolution mass spectrometer (HRMS; Impact HD, Bruker Daltonics, Billerica, MA). Details of the experimental setup[12, 100] as well as protocols of operation and performance validation[101] were described elsewhere. Experimental settings were optimized for separating metabolites by CE (capillary, 1 m and 40/105 μm inner/outer diameter; potential on inlet end, +18–20 kV dynamically adjusted to maintain ~7.5–8.0 μA current across the fused silica capillary) and ionizing them in a co-axial sheath flow CE-ESI interface (flow rate of sheath liquid, 0.6 μL/min; design, earth grounded; spray regime, coaxial for optimal ionization efficiency. The generated ions were mass-analyzed on a quadruple orthogonal-acceleration time-of-flight HRMS with the following settings: spray voltage, –1,700 V (applied to orifice front plate); MS survey scan rate, 2 Hz; mass range (MS1 and MS2), *m/z* 50–550; collision-induced dissociation, 18–20 eV in nitrogen collision gas; dry gas, 2 L/min at 100 °C. The mass spectrometer was externally mass calibrated on a bi-daily basis to <0.6 ppm mass (m/z) accuracy using sodium formate clusters that formed as sodium ions of abundance in the sample migrated into the ion source.

4.2.9 Data analysis

Primary HRMS–MS/MS data were processed in Compass DataAnalysis version 4.3 (Bruker Daltonics) following our established protocols.[12] Each data file was externally mass (*m/z*) calibrated to <0.6 ppm mass accuracy using sodium

formate clusters. A custom-written script was used to generate extracted ion chromatograms (EICs) for identified metabolites and their [M+1] isotopes within ±5 mDa accuracy. Peak intensities and the under-the-curve peak areas were manually integrated. Precise masses (*m/z* values) were calculated in Compass IsotopePattern (Bruker Daltonics version 4.3). Isotope ratios (%) were normalized to the monoisotopic peak. Metabolic pathway analysis was conducted in MetaboAnalyst 4.0[120] with the following settings: pathway library, *Danio rerio* (zebrafish) model; pathway analysis algorithm, overrepresentation analysis by hypergeometric test, and pathway topology by relative betweenness centrality. Pathway mapping was performed using Kyoto Encyclopedia of Genes and Genomes (KEGG).[158] Statistics. The metadata were normalized by total sum and further evaluated in MetaboAnalyst 4.0 using Euclidian method to calculate the distance matrix and Ward method to generate data clusters for hierarchical cluster analysis. One-way ANOVA was measured at p-value <0.05 to determine statistical significance and post-hoc tests using Fisher's least significant discriminant (LSD). Two-tailed Mann-Whitney U test was calculated in OriginPro 2016 (OriginLab, Northampton, MA) with $p \leq 0.05$ marking significance.

4.3 Results and discussion

4.3.1 Altering the concentration of individual metabolites results in cell fate changes

A recent study uncovered differences in metabolite levels among three cell types on the 16-cell *X. laevis* embryo located in the dorsal–ventral and animal–vegetal developmental axes using single-cell dissection and CE-ESI-MS.[12] Based on

established cell fate maps,[58, 134] each targeted cell has a predetermined cell fate leading to the formation of specific tissues. For example, the midline dorsal-animal D11 cell gives rise to the brain, retina, and central somite, whereas the midline ventral-animal V11 cell gives rise to the head and trunk epidermis (Fig. 4.1). Although single-cell MS was able to capture metabolite abundance differences between D11 and V11 cells, further experiments revealed the developmental significance of cell-specific metabolite profiles in determining cell fates. Interestingly, it was found that injecting a subset of metabolite standards into dorsal D11 or ventral V11 cells influences their corresponding tissue fates. For example, microinjecting a mixture of metabolite standards that were quantified as largely abundant in the V11 cell (e.g., acetylcholine and methionine) along with a fluorescent lineage tracer into the D11 cell (Fig. 4.1A) showed a reduction in the fluorescent labeling of neural tissues such as the brain and central somite. Consequently, a substantial increment of fluorescently labeled cells that corresponded to head and body epidermis was noticed. Likewise, microinjecting metabolites found in higher concentrations in the D11 cell (e.g., serine and threonine) into the V11 cell (Fig. 4.1B) revealed the establishment of neural tissues such as the retina and cement gland. Although it was previously demonstrated that altering the concentration of a mixture of metabolites in dorsal and ventral cells has an effect on tissue fate, as the metabolome reacts rapidly to intrinsic and external factors such as concentration variations due to cellular actions;[150] we anticipated that altering the concentration of an individual metabolite can result in substantial changes to cell fate.

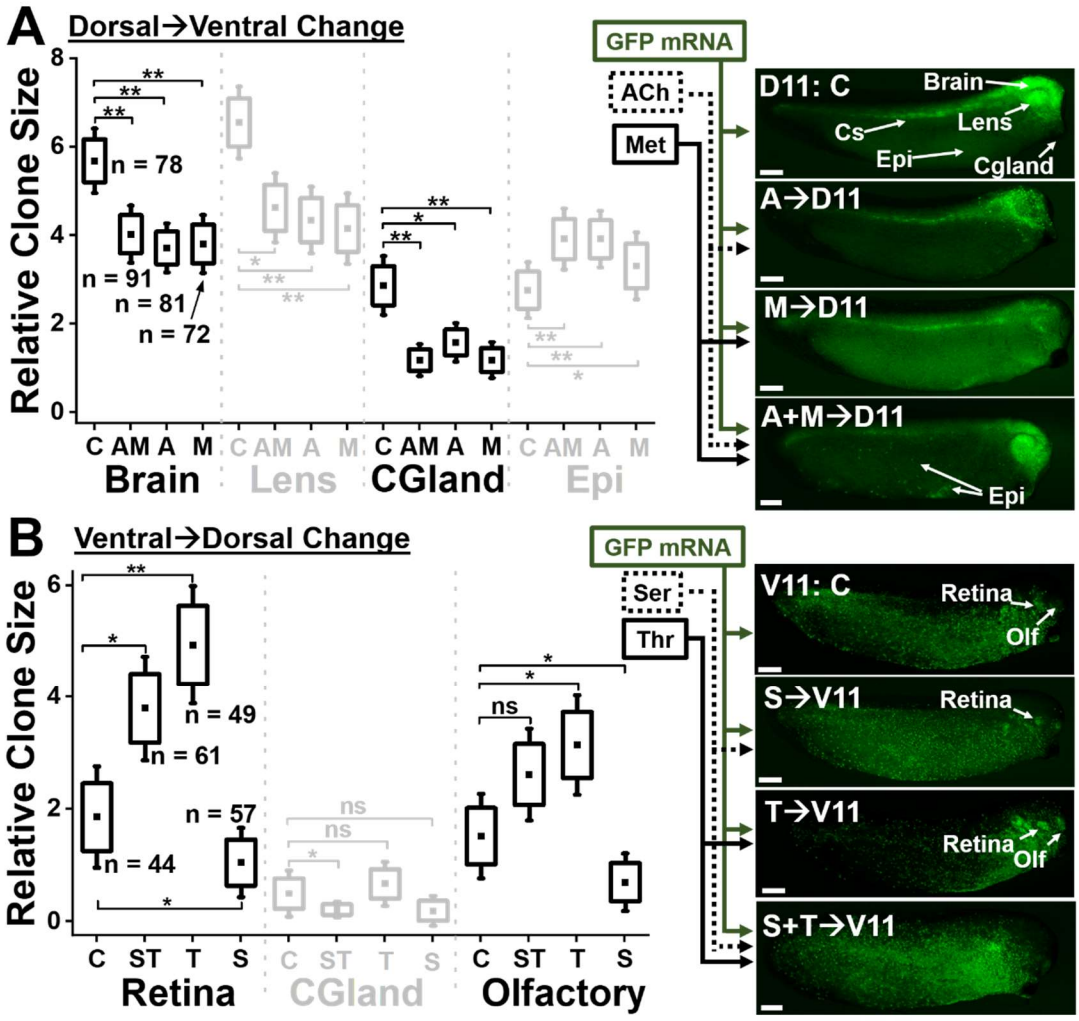

Figure 4.1 Metabolite microinjections and cell linage tracing at larval stages (side view) to test metabolite-induced cell fate changes. (A) D11 cells were injected with GFP mRNA only as control, GFP mRNA plus a mixture of acetylcholine and methionine (A+M), and GFP mRNA with acetylcholine (A) or methionine (M). Fluorescent D11 descendant cells corresponding to central somite (Cs), cement gland (CGland), and epidermis (Epi) are observed. (B) V11 cells were injected with GFP mRNA only as control, GFP mRNA plus a mixture of serine and threonine (S+T), and GFP mRNA with serine (S) or threonine (T). Fluorescently labeled descendant cells of the V11 corresponding to retina and olfactory placode (Olf) were observed. Scale bar = 300 μm.

To compare the effect of individual metabolite injections to the cell fate of the D11 and V11 cell, we microinjected metabolite standards (Fig. 4.1) as discussed in

the experimental section. Acetylcholine and methionine chemical standards were microinjected into D11 cells as a mixture (n = 91) and individually (n = 81 and n = 72, respectively) along with a fluorescent lineage tracer to help with the identification of the clone at the larval stage. Additionally, a subset of D11 cells were microinjected with lineage tracer only (n = 78) to serve as a control. We conducted lineage analysis at the larval stage (stage 34) by determining the relative contribution of fluorescent cells to the organ/tissue fate as described elsewhere.[134-135] As observed in our previous study,[12] the injection of acetylcholine and methionine mixture into the D11 cell (Fig. 4.1A) shows a significant decrease in the fluorescent labeling of the brain and central somite, and an increase of epidermal cells as compared to the control larvae injected with lineage tracer only. Remarkably, individual injections of acetylcholine and methionine also showed a significant reduction in the formation of neural structures (Appendix 4.1). For example, the injection of acetylcholine revealed a substantial effect on the formation of the brain (Mann-Whitney $U = 4180$, $p < 0.0005$) as compared to the injection of the metabolite mixture (Mann-Whitney $U = 4586$, $p = 0.0006$). Likewise, injecting methionine in the D11 showed a significant decrease on the formation of the lens and olfactory placode than observed with the metabolite mixture (Mann-Whitney $U= 3372$, $p = 0.02$ and $p = 0.06$). Additionally, we microinjected serine and threonine as a mixture (n = 61) and individually (n = 57 and n = 49, respectively) into V11 cells and uncovered a significant formation of the retina with discrete metabolite microinjections (Mann-Whitney (mixture) $U = 1004$, $p = 0.01$ and (threonine) $U= 696$, $p < 0.0005$). Thus, we find that altering the concentration of a single metabolite causes downstream responses in the metabolisms

of *X. laevis* embryonic cells that lead to changes in tissue fate. Supporting this notion, it is well-known that metabolite concentrations are essential to regulate cellular processes such as reaction rates[159] and enzyme binding[160] that influence the dynamic state of the metabolome.

4.3.2 Tracking dynamic metabolic pathways of early developing clones

To investigate the effect of metabolite-injections that alter the metabolism of dorsal and ventral cells, we developed a stable isotope labeling strategy compatible with the live developing *X. laevis* embryo. Using isotope tracers, we sought out to investigate downstream metabolite labeling patterns to elucidate dynamic metabolic pathways. First, we selected isotope tracers based on previous knowledge of the D11 and V11 cell metabolome.[12] For example, single-cell MS measurements found threonine to be highly enriched in the D11 cell as compared to the V11, raising the possibility of a fast turnover of threonine in dorsal clones. First, we tested the incorporation of heavy isotope threonine ($^{13}C_4$,^{15}N-L-threonine or Thr*) by injecting the dorsal-left cell in the 4-cell embryo, when the dorsal–ventral developmental axis is established, and microsampling a portion of the D11 cell in the 16-cell embryo. Single-cell CE-ESI-MS analysis of control and Thr* injected D11 cells identified fast incorporation of ^{13}C and ^{15}N by comparing experimental and theoretical percent isotope abundance of the M+1 signal for a subset of previously identified metabolites. Based on the fast incorporation of threonine isotope tracer, with ~30–40 min of developmental time between the 4- to 16-cell *X. laevis* embryo[161] at room temperature, we extended the isotope labeling approach to investigate isotope

labeling patterns during cleavage and blastula stages (Fig. 4.2). Additionally, we selected heavy isotope methionine ($^{13}C_5$,^{15}N-L-methionine or Met*) as an isotope tracer for the ventral clone, since methionine has been previously detected in high abundance in the V11 cell.[12]

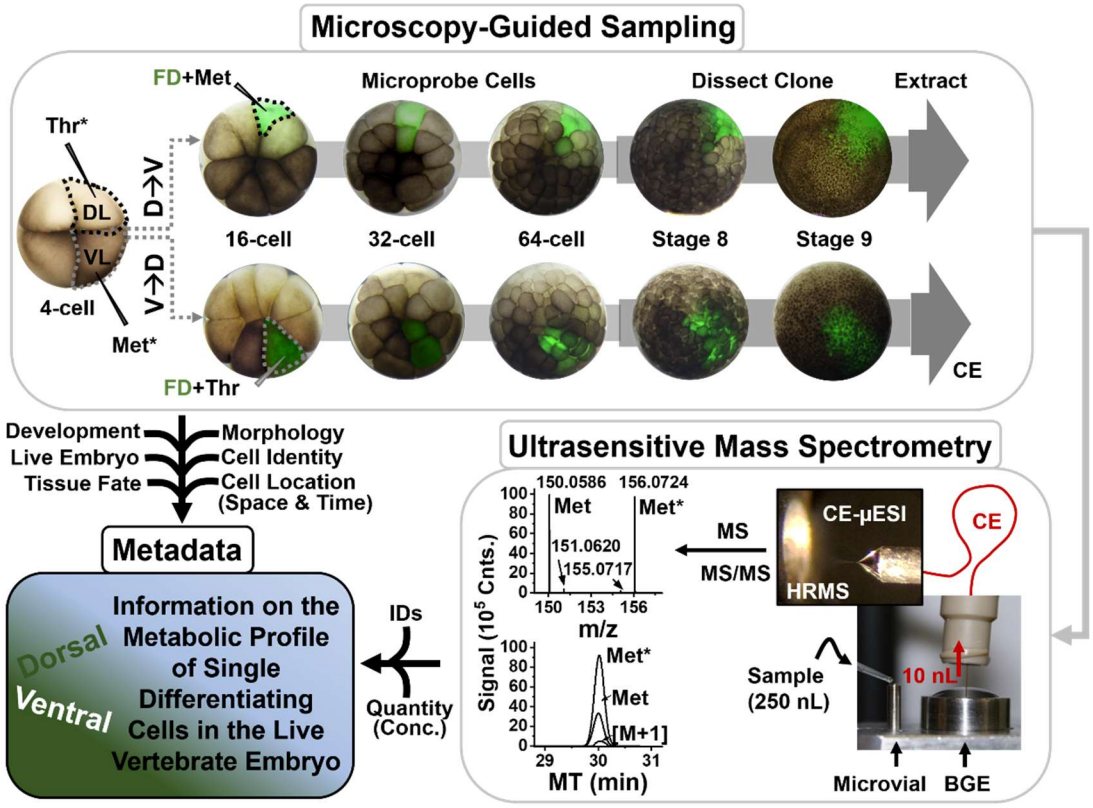

Figure 4.2 Stable isotope labeling workflow to investigate metabolic pathways involved in metabolite-induced cell fate alteration in early developing dorsal and ventral clones of *X. laevis*. Thr* was injected into dorsal cells and Met* into ventral cells with fluorescent dye (FD), followed by single-cell CE-ESI-HRMS workflow. Scale bar = 250 μm

The overall stable isotope labeling approach to track metabolic pathways that participate in dorsal and ventral cell fate specification is presented in Fig. 4.2. To investigate a dorsal-to-ventral cell fate change (Fig. 4.2A), we injected the dorsal-left cell with heavy isotope threonine and cultured the embryo to the 16-cell stage; then,

methionine was injected to alter the D11 cell fate. A fluorescent dye was co-injected into the D11 cell to facilitate cell-clone tracking and targeted sampling, as cell division becomes asymmetrical and less synchronized during blastula stages.[162] Using our recently developed microprobe sampling approach,[55] we collected ~ 10–15 nL of cellular content from offspring cells of the D11 at the 32- and 64-cell stage, and conducted cell-dissection of fluorescent dorsal clones at stages 8 and 9. For each developmental stage, n = 3–4 biological replicates were collected to ensure statistical confidence. To track native metabolism of dorsal clones, a control group was collected (n = 3 biological replicates per stage) comprising of dorsal clones without methionine injections. We applied the same approach to track ventral-to-dorsal cell fate change (Fig. 4.2A); however, the ventral-left cell was injected with a heavy isotope methionine tracer, and threonine at the 16-cell embryo to alter V11 cell fate (n = 3–4 biological replicates). A control group for ventral clones was collected in n = 3 biological replicates per stage. A detailed report of heavy isotope metabolite tracer injections, cell sampling and single-cell CE-ESI-MS analysis is provided in the methods.

We calculated the percent isotope abundance of the M+1 signal for a subset of ~70 previously identified metabolites (Appendix 4.2). Metabolites that exhibited significantly higher M+1 signal abundance as compared to theoretical values derived from each metabolite chemical formula, were considered to have incorporated ^{13}C and ^{15}N from heavy isotope tracers. These metabolites were mapped to the Kyoto Encyclopedia of Genes and Genomes (KEGG),[158] a metabolomic knowledgebase to examine pathway significance resulting from pathway enrichment analysis, and

pathway impact calculated from pathway topology analysis (Figure 4.3). Interestingly, several pathways were enriched with high significance ($p < 0.005$), including arginine–proline metabolism, which has been identified in early cleavage *X. laevis* embryos.[30, 57] Moreover, metabolism of threonine isotope tracer in the dorsal clone identified the arginine–proline and glutathione metabolisms as statistically significant with a high pathway impact. However, when methionine was injected in the D11 cell, the isotope labeling pattern revealed a significant enrichment of the valine–leucine–isoleucine metabolism (Figure 4.3A) in the dorsal clone. Recent studies have documented the correlation between branched chain amino acids (e.g., leucine, glutamine, and isoleucine) and the (mammalian target of rapamycin) mTOR signaling pathway,[163] largely known to serve as a regulator of cell metabolism, proliferation, development, and survival.[164] Although it is unclear whether amino acids are able to activate mTOR, protein kinases have been identified as mediators of amino acid signaling to induce mTOR in stem cells.[165-166] Additionally, metabolism of the methionine isotope tracer in the ventral clone reveled arginine–proline and alanine–aspartate–glutamate metabolisms as statistically significant; but after injecting threonine into the V11 cell (Figure 4.3B), the labeling pattern exhibited enrichment of the glutathione metabolism. This is consistent with recent findings indicating the importance of redox regulation during early embryonic cell differentiation.[144] For example, glutathione (GSH) serves as a reducing agent that protects the cell from oxidative stress/damage by converting to its oxidized form (oxidized-glutathione, GSSG). We observed incorporation of the isotope tracer in the

oxidized-glutathione (GSSG) form; thus, we hypothesize that the glutathione metabolism is activated to maintain homeostasis.

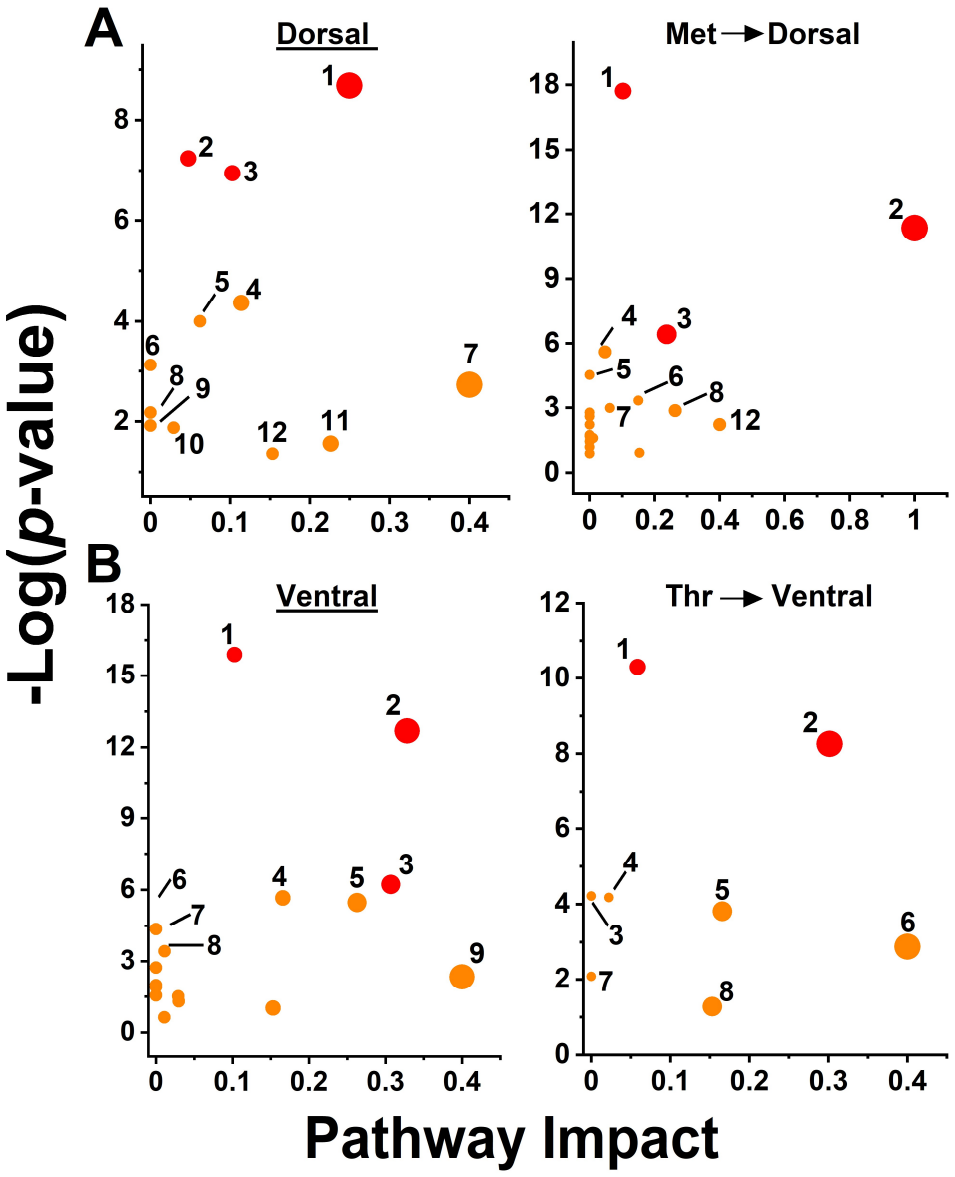

Figure 4.3 KEGG pathway analysis of (A) dorsal cell clones injected with $^{13}C_4$,^{15}N-L-threonine and dorsal clones injected with Thr* and methionine. (B) Ventral clones injected with $^{13}C_5$,^{15}N-L-methionine (or Met*), and ventral clones injected with Met* and threonine. Key to labels in Appendix 4.3.

4.3.3 Effect of isotope tracer injections to embryonic development

Since altering the inherent metabolite abundance of D11 and V11 cells causes changes to tissue fate, we tested whether injection of isotope tracers leads to cell fate changes (Fig. 4.4). For instance, threonine was measured at 10 pmol and found to be significantly abundant in the D11 cell as compared to the V11 cell;[12] however, we microinjected its isotope tracer equivalent ($^{13}C_4$,^{15}N-L-threonine) in a fourfold (×4) quantity at 40 pmol. Similarly, methionine was measured at 20 pmol in the V11 cell and its isotope tracer equivalent ($^{13}C_5$,^{15}N-L-methionine) was injected into the ventral cell in a threefold (×3) concentration at 60 pmol (see experimental methods). Lineage analysis at the larval stage revealed statistical differences (Mann-Whitney U = 2628, p = 0.0192) in the formation of the olfactory placode, between control (n = 72) and heavy-isotope threonine injected (n = 67) D11 cells. In ventral cells, lineage and statistical analysis revealed no differences between control (n = 70) and heavy-isotope methionine injected (n = 58) V11 cells.

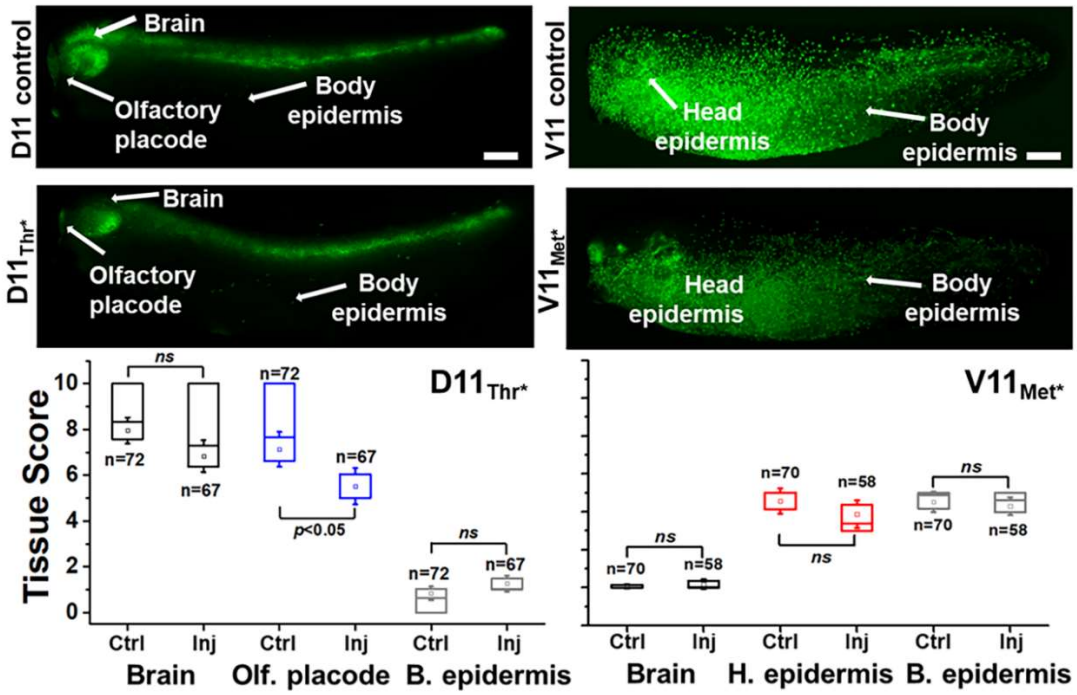

Figure 4.4 Injection of isotopically labeled metabolites and cell lineage tracing in *X. laevis* embryos. Scale bar = 300 µm.

4.3.4 Single-cell metabolome reorganizes during cell fate commitment

Metabolite profiles of control and metabolite-injected dorsal and ventral clones were compared using multivariate analysis. Unsupervised hierarchical cluster analysis (HCA) and heat map (Fig. 4.5) analysis were performed based on 60 commonly identified metabolites and 20 corresponding M+1 signals among dorsal and ventral clones. The relative abundance of each signal was computed by integrating the under-the-curve peak area of extracted ion electropherograms. The resulting dendrogram shows the clustering of all samples into four main groups (Fig. 4.5, Top axis), each corresponding to different experimental conditions: dorsal clone (control), dorsal clone injected with methionine, ventral clone (control), and ventral

clone injected with threonine. Sub-clustering of each group reveals that cleavage (32- and 64-cell) and blastula stages (stages 8 and 9) are comprised of different metabolite abundances. In support of this view, a previous study conducted on single dorsal-cells of the 16- and 32-cell *X. laevis* embryo revealed a subset of metabolites (e.g., creatine, lysine, arginine) that maintain similar abundance levels in the cleavage stages.[55] Likewise, a study on whole *X. laevis* embryos confirmed the increase of select metabolites (e.g., glutamine, α-ketoglutarate) during blastula stages as part of the tricarboxylic acid (TCA) cycle.[13] Based on these observations, it is possible that the sub-clustering observed in our data reflects metabolic changes between cleavage and blastula stages.

We also identified differential clustering of metabolite abundance among experimental conditions (Fig. 4.5, Top axis) resulting in two subgroups. Surprisingly, the left group consisted of samples collected from ventral cells and methionine-injected dorsal cells, revealing a small subset of metabolites (Fig. 4.5, Left axis, bottom) found in high abundance between the two groups. After injecting methionine into the D11 cell in the 16-cell embryo, it appears that the metabolome of its offspring cells (32-cell to stage 9) adjusts rapidly to the perturbation in metabolite concentration. In this case, the metabolite composition of methionine-injected dorsal clones becomes similar to the ventral clone. Similarly, the right group (Fig. 4.5, Top axis) contains samples collected from dorsal cells and threonine-injected ventral cells; suggesting that the metabolome of dorsal and ventral clones injected with metabolite standards to alter cell fate commitment rapidly reorganizes to replicate the metabolic state of its new corresponding cell fate.

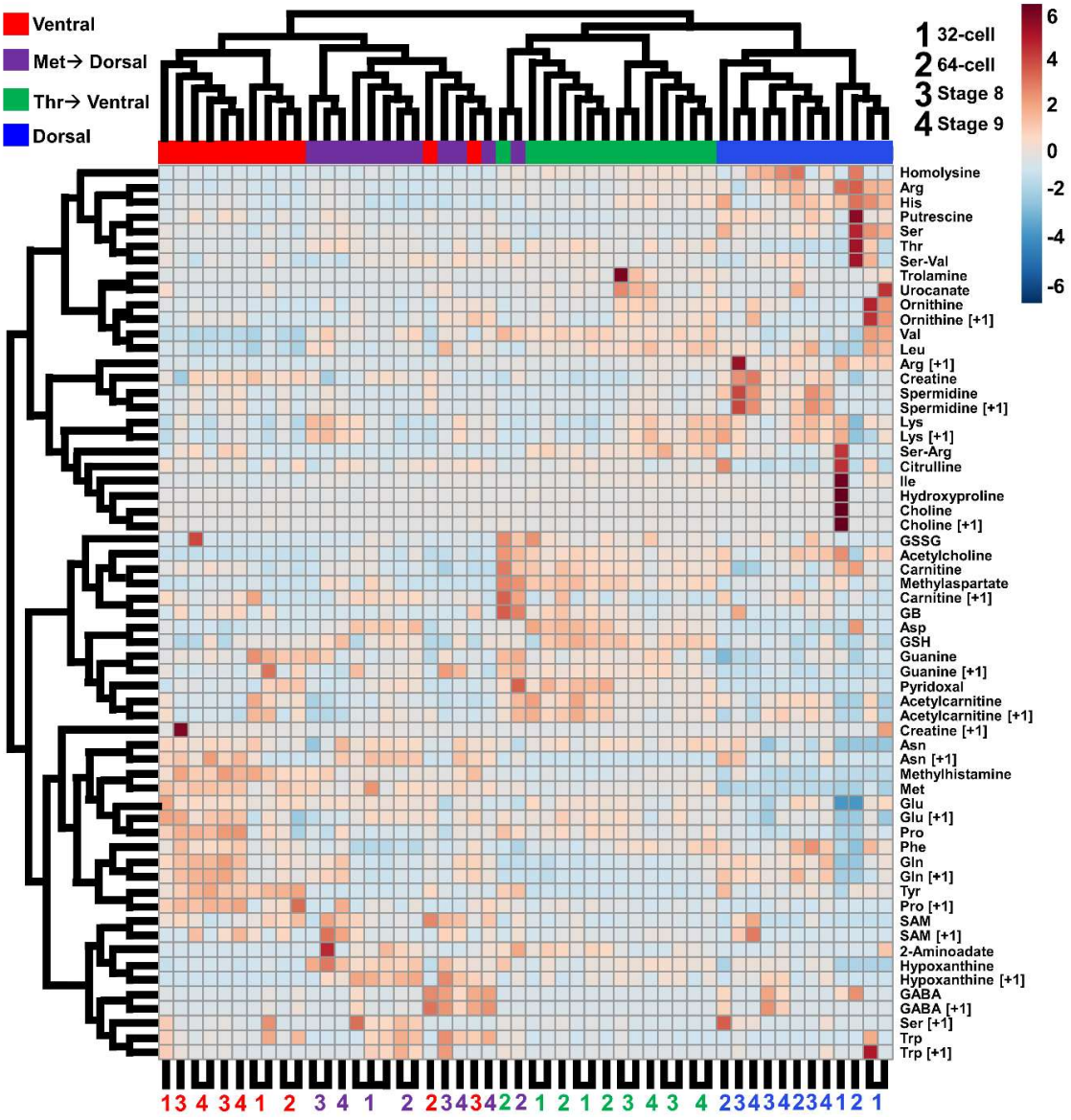

Figure 4.5 Hierarchical cluster analysis- heat map of metabolites detected in dorsal and ventral clones. (Top) Experimental and control groups, (Right) metabolite identifiers, (Left) clustering, and (Bottom) sample-stage identifiers. Metabolite abundance was normalized to the total sum.

Although stable isotope labeling was able to capture differences in metabolic pathway activity during metabolite-induced cell fate changes, a secondary effect in metabolite production was also uncovered with an untargeted metabolomics

approach. Isotope labeling patterns are directly associated to metabolic pathways that utilize (deplete) the isotope tracer introduced into the organism. Thus, all downstream changes in metabolism would hardly participate in isotope labeling patterns alone; instead there are additional resulting widespread alterations to the metabolome. Analysis of variances (ANOVA) uncovered a subset of 30 metabolites (Table 4.1) with statistically different abundance levels among the four experimental groups (Fig. 4.5, Top). For instance, there is a significant increase in the relative abundance of aspartate, glutathione, and hypoxanthine in metabolite-injected clones. Unexpectedly, the increase in aspartate concentration during early embryonic development contradicts previous isotope-flux experiments in whole *X. laevis* embryos[13] and single-cell metabolic profiling of D11 offspring cells.[55] Recent experiments identified alanine as an energy source that rapidly converts to aspartate in early developing *X. laevis* embryos, which acts as a source of nitrogen to produce glutamine and other nucleotides for the embryo. In agreement with the notion that consumption-production of aspartate and glutamine are interconnected, we observed a decrease in glutamine abundance after the injection of metabolites that lead to cell fate changes. The change in production of aspartate suggests a significant shift in the Ala–Asp–Glu pathway, indicating the activation of other metabolic networks including the Cys–Met and glutathione metabolism (Fig. 4.6).

Table 4.1 Metabolite abundance changes calculated by one-way ANOVA between dorsal and ventral clones injected with heavy-isotope tracers and metabolites to alter cell fates. Key: F value, ratio of variance; FDR, false discovery rate.

ID	Metabolite	F value	*p* value	FDR
1	2-Aminoadate	4.64	6.45E-03	1.16E-02
2	Acetylcarnitine	4.09	1.18E-02	1.89E-02
3	Acetylcholine	12.27	5.03E-06	2.79E-05
4	Arginine	13.72	1.59E-06	1.04E-05
5	Arginine [+1]	9.76	4.24E-05	1.72E-04
6	Asparagine	7.47	3.56E-04	1.03E-03
7	Asparagine [+1]	8.07	2.00E-04	6.41E-04
8	Aspartate	12.06	6.00E-06	3.05E-05
9	Carnitine	5.55	2.46E-03	5.00E-03
10	Creatine	4.36	8.79E-03	1.53E-02
11	Glutamate	4.32	9.16E-03	1.55E-02
12	Glutamate [+1]	6.58	8.58E-04	2.09E-03
13	Glutamine	8.54	1.29E-04	4.93E-04
14	Glutamine [+1]	7.08	5.23E-04	1.39E-03
15	Glutathione	13.64	1.70E-06	1.04E-05
16	Guanine	5.26	3.34E-03	6.36E-03
17	Guanine [+1]	6.67	7.85E-04	1.99E-03
18	Histidine	14.52	8.65E-07	6.59E-06
19	Homolysine	8.27	1.66E-04	5.92E-04
20	Hypoxanthine	18.68	4.58E-08	5.58E-07
21	Hypoxanthine [+1]	14.92	6.41E-07	5.59E-06
22	Leucine	6.52	9.12E-04	2.14E-03
23	Methionine	46.05	6.68E-14	2.04E-12
24	Methyl- aspartate	15.42	4.45E-07	4.52E-06
25	Methyl- histamine	47.51	3.91E-14	2.04E-12
26	Phenylalanine	6.18	1.29E-03	2.70E-03
27	Proline	10.30	2.65E-05	1.16E-04
28	Proline [+1]	11.94	6.62E-06	3.11E-05
29	Putrescine	5.52	2.54E-03	5.00E-03
30	Pyridoxal	7.50	3.44E-04	1.03E-03
31	SAM	6.26	1.18E-03	2.57E-03
32	Ser-Arg	4.29	9.44E-03	1.56E-02
33	Serine	7.30	4.21E-04	1.17E-03
34	Spermidine	8.22	1.75E-04	5.92E-04
35	Spermidine [+1]	5.03	4.25E-03	7.86E-03
36	Tryptophan	6.33	1.10E-03	2.48E-03
37	Tyrosine	21.35	8.26E-09	1.68E-07
38	Valine	18.97	3.78E-08	5.58E-07

Next, we mapped our data comprising of isotopically-labeled metabolites, and metabolites identified to change abundance levels using ANOVA to the KEGG database. The results showed a high coverage of the following metabolic pathways: Arg–Pro, Gly–Ser–Thr, Cys–Met, Ala–Asp–Glu and glutathione metabolism. Fig. 4.6 shows a reconstructed metabolic network containing the formerly identified metabolic pathways. Several metabolites exhibit a direct relation to the injected isotope tracers. For example, isoleucine, tyrosine, γ-aminobutyric acid (GABA), and carnitine showed incorporation of heavy isotope ^{13}C or ^{15}N after the injection of methionine into the D11 cell to cause a shift from dorsal-to-ventral cell fate. Additionally, metabolites such as leucine and glutamine presented both heavy isotope incorporation and significant changes in abundance based on ANOVA. Moreover, a subgroup of metabolites including aspartate, phenylalanine, proline, S-adenosylmethionine, and acetylcarnitine were identified to significantly vary in abundance levels after injection of methionine into the D11 cell. Intriguingly, the latter two metabolites were found to be accumulated in the dorsal clone after injection of methionine; however, previous studies reported their enrichment in ventral cells in the 16-cell *X. laevis* embryo[12] with acetylcarnitine decreasing in abundance in the dorsal clone during cleavage stages.[55]

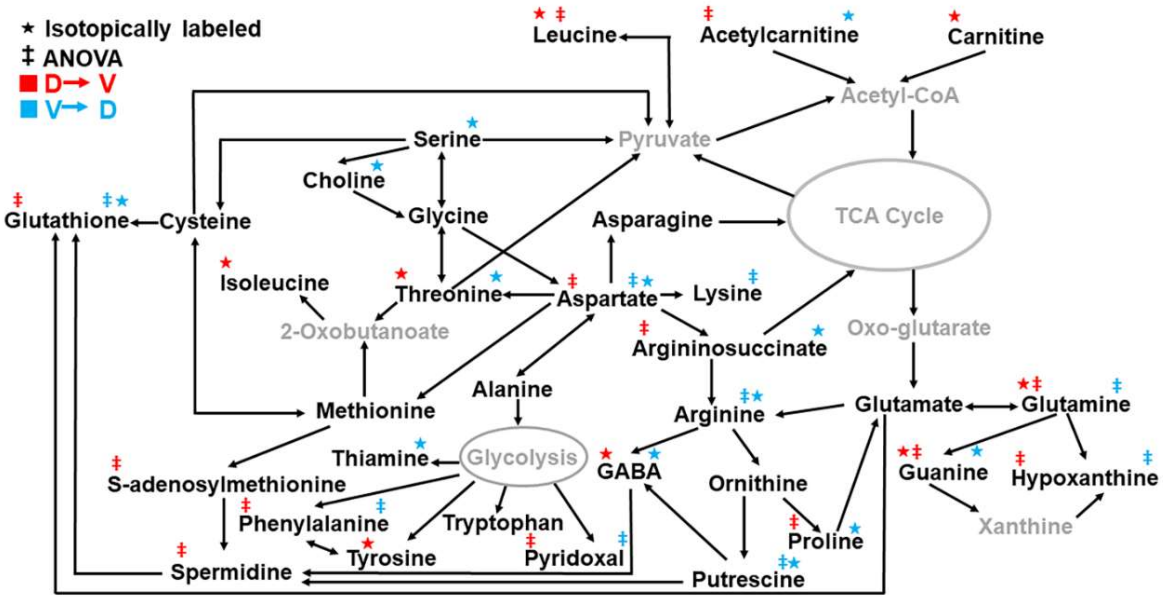

Figure 4.6 Dynamic metabolic network participating in metabolite-induced cell fate modification of dorsal and ventral cells. Key: left-star (★) denotes isotope pattern derived from injection of methionine into D11 cell to induce dorsal-to-ventral tissue fate. Right-star (★) corresponds to isotope pattern resulting from injection of threonine into V11 to induce ventral-to-dorsal cell fate. Double-dagger (‡) indicates significant changes in abundance calculated by ANOVA. Metabolites in grey were not detected.

A similar trend was observed after injecting threonine into the V11 cell to induce ventral-to-dorsal tissue fate. For example, threonine-injected ventral clones revealed heavy isotope incorporation of serine, choline, aspartate and thiamine. Other metabolites such as arginine, putrescine, and glutathione showed incorporation of heavy isotopes from the methionine isotope tracer, as well as additional changes in concentrations identified by ANOVA (Table 4.1). As previously mentioned, ventral clones injected with threonine showed an enrichment in the glutathione metabolism, suggesting the rapid initiation of the glutathione pathway as a response to oxidative stress caused by metabolite concentration alteration. Although we identified similar metabolites between isotope patterns derived from dorsal and ventral clones, the

metabolic responses of these cell types to metabolite injections that alter cell fate are distinctive (see Fig. 4.6). It appears that some metabolites partake in fundamental mechanisms in the cell, for example, aspartate and glutamine play essential roles as energy source for the embryo and were found to be equally important to cell fate commitment. Likewise, we observed isotopic incorporation and metabolite abundance changes that are unique to the dorsal or ventral cell type, emphasizing the importance of single-cell measurements to uncover molecular processes that lead to neural and epidermal tissue fates.

4.4 Conclusions

In the presented work, we uncovered dynamic metabolic pathways that participate in cell specification of dorsal and ventral clones during early stages of *X. laevis* embryonic development. First, we determined metabolites that can alter dorsal and ventral cell fate commitment and designed a stable isotope labeling strategy compatible with the live embryo to elucidate dynamic metabolism. By implementing stable isotope labeling and single-cell MS, we investigated metabolism of normal (control) and metabolite-injected dorsal and ventral clones and uncovered previously unknown changes in metabolic activity. Our data suggest that the glutathione metabolism plays an important role in early developing embryonic cells, as they establish their corresponding tissue fates. The metabolic trends identified in this work corroborate previous findings at the whole-embryo level and open new frontiers to study metabolism of individual cells. We also discovered the rapid remodeling of the metabolome after metabolite-induced cell fate alteration and identified central

metabolites (e.g., aspartate and glutathione) that appear to contribute to the reestablishment of cell specification. Finally, we verified the effect of isotope tracer injections to the development of the *X. laevis* embryo.

Chapter 5: Cell-by-cell interrogation of metabolic activity uncovers small-molecule gradients in the live frog embryo

Based on material in preparation for submission by Erika P. Portero, Leena Pade, Jie Li, and Peter Nemes*.

5.1 Introduction

Detection and quantification of biomolecules in single cells is essential to enhance our understanding of biochemical processes that take place to establish cell functionality and heterogeneity.[71, 88] Although recent developments in single-cell mass spectrometry (MS) have enabled the characterization of metabolic differences among neurons,[14] trichome[93] and *Allium cepa* cells,[94] sampling the fast-changing metabolome during live development still presents a major analytical challenge. Due to the volume-limited sample afforded by single cells and the complexity of the metabolome, fast and minimally invasive sampling techniques are required. Currently, a variety of analytical tools coupled to MS have been devised to study the metabolome of single cells including single probe,[28, 167] microprobe,[55] microsampling,[29] patch clamp pipette,[56] live single-cell video MS,[168] and microdissection of cells.[12, 57] In Chapter 2, I discussed the development of microprobe[55, 101] as a sampling technique for single-cell metabolomics. Microprobe sampling was designed to assist in the collection, handling, and extraction of small sample volumes from cells of the 8-, 16-, and 32-cell *X. laevis* embryo.[55] In this chapter, I apply microprobe CE-ESI-MS analysis to investigate spatial metabolic heterogeneity among dorso–ventral cells located in the same 16-cell *X. laevis* embryo.

Spatial and temporal mapping of biomolecules during embryonic development can provide new insights into mechanisms that underlie tissue differentiation and organogenesis. For instance, recent studies have focused on understanding the role of metabolites in cell division and differentiation[144, 165] and their implications in developmental biology.[13, 169] Since metabolites are effector molecules that act downstream to transcriptional and translational changes, a metabolic analysis can help uncover the physiological state of the cell.[64] Previous studies conducted in the Nemes lab characterized metabolites in embryonic cells of the *Xenopus laevis* frog and investigated changes in cell fates caused by metabolite injections.[12] Additional studies have uncovered the significance of small molecules and gap junctional communication in early development and morphogenesis.[170] Gap junctions act as channels for the passage of metabolites between adjacent cells, supporting cell-to-cell communication and serving as important mediators for small molecule signaling within embryonic cells.[171-173] Specifically, gap junctions were found to play a role in establishing left–right symmetry in early developing *X. laevis* embryos. Thus, it was demonstrated that modulating junctional communication leads to heterotaxia in developing embryos.[170]

In this work, microprobe CE-ESI-MS was utilized to characterize metabolites among four adjacent cells located in the left–animal axis of the 16-cell *X. laevis* embryo. Using cluster analysis, we uncovered metabolite concentration gradients across selected dorso-ventral cells. Besides empowering statistical analysis by minimizing embryo-to-embryo metabolic variability, microprobe CE-ESI-MS analysis enabled the study of transjunctional transport of metabolites using stable

isotopically labeled metabolites and single-cell MS analysis. The results demonstrated the effective transfer of small molecules (e.g., methionine, threonine) between dorsal and ventral cells. Furthermore, using fluorescent cell lineage tracing, we investigated the effect of metabolite injections to cell fate alteration between adjacent dorsal cells. Finally, a color preference behavioral assay was conducted to test the visual function of *X. laevis* tadpoles (stage 45) injected with a metabolite that alters the tissue fate of neural-fated dorsal cells.

5.2 Experimental

5.2.1 Chemicals and solutions

LC-MS formic acid, methanol, acetonitrile, and water, as well as phosphate buffered saline (PBS, 100X) solution, melatonin, and Alexa Fluor Dextran 488 (FD) were purchased from Fisher Scientific (Fair Lawn, NJ). Acetylcholine chloride, L-methionine were from Acros Organics (Fair Lawn, NJ). Carbenoxolone disodium salt, ficoll PM 400, $^{13}C_4$,^{15}N-L-threonine, and $^{13}C_5$,^{15}N-L-methionine were purchased from Sigma–Aldrich (Saint Louis, MO). Cysteine, diethyl pyrocarbonate (DEPC), and paraformaldehyde were from MP Biomedicals (Solon, OH).

Steinberg's solution (SS), 2% cysteine, 4% paraformaldehyde in PBS, 0.1X Marc's Modified Ringer's (MMR) solution, and 3% ficoll were prepared following previous protocols.[126] The "extraction solution" contained 40% (v/v) acetonitrile and 40% (v/v) methanol in MS-grade water at pH 4.70.[57] The CE "background electrolyte" (BGE) contained 1% (v/v) formic acid in MS-grade water (pH 2.8). The

CE-ESI "sheath liquid" contained 50% (v/v) methanol and 0.1% (v/v) formic acid in MS-grade water.

5.2.2 Microprobe fabrication

Borosilicate glass capillaries (part no. B100-50-10, 0.5/1 mm inner/outer diameter, Sutter Instruments, Novato, CA) were first pulled to narrow tips with ~900 µm barrel length using a micropipette puller (model P-97, Sutter Instruments, Novato, CA) following earlier protocols.[55, 101] The aperture of each micropipette tip was ~20 µm inner diameter.

5.2.3 Animals and embryo collection

Male and female *Xenopus laevis* frogs were obtained from Nasco (Fort Atkinson, WI) and maintained in a breeding colony at the University of Maryland, College Park. All protocols related to the maintenance and handling of *Xenopus laevis* were approved by the Institutional Animal Care and Use Committee (IACUC no. R-DEC-17-57). Fertilized embryos were obtained via gonadotropin-induced natural mating of adult frogs and the jelly coats from freshly-laid embryos were removed using a 2% cysteine solution following established protocols.[126] Dejellied embryos were kept in Petri dishes containing 100% SS, and 2-cell embryos showing stereotypical pigmentation patterns[134] across the left-right axis were transferred into a separate Petri dish. Embryos were cultured at 14 ˚C until they reached the 16-cell stage and transferred to a dish containing 3% ficoll in 100% SS. In each embryo, the midline-left ventral V11, V12, and dorsal D11 and D12 cells were identified based on pigmentation and location in reference to cell fate maps.[58]

5.2.3 Single-cell microprobe sampling

A fabricated microprobe was mounted on a micromanipulator (Harvard Instruments, Holliston, MA) and the tip was fine positioned into the target cell under a stereomicroscope. A ~10 nL portion of the cell's content was aspirated using a microinjector operated in the fill mode (model PLI-100A, Warner Instruments, Hamden, CT). Thereafter, the microprobe tip was retracted from the cell, and the microinjector was reversed to the injection mode to eject the captured cytoplasmic fraction into a micro vial containing 4 μL of extraction solvent chilled to ~4 °C. The cellular content of each target cell was microaspirated using separate microcapillaries to avoid potential contamination among samples. Metabolite extracts were vortex-mixed for 1 min at room temperature and centrifuged at 8 000 ×g at 4 ˚C for 5 min. Vials containing metabolite extracts were stored at –80 ˚C until measurement by CE-ESI-MS. For each cell type, n = 3−5 biological replicates were sampled (same cell type measured from different embryos). Additionally, each cell extract was measured in 2–3 technical replicates. This study was comprised of embryos from 1 and 2 sets of parents to compare and minimize genetic variability.

5.2.4 Regulating metabolite transfer

Fertilized 2-cell embryos were selected based on stereotypical pigmentation patterns and isolated in a Petri dish containing 100% SS. Control embryos were monitored under a stereomicroscope until they reach the 8-cell stage and injected into the D1 cell with a 2 nL solution containing 20 mM $^{13}C_4$,^{15}N-L-threonine and 10 mM $^{13}C_5$,^{15}N-L-methionine. A second set of embryos was injected with 100 μM

carbenoxolone into the DL cell at the 4-cell stage to inhibit transjunctional communication between cells. Then, injected with 20 mM $^{13}C_4$,^{15}N-L-threonine and 10 mM $^{13}C_5$,^{15}N-L-methionine into the D1 cell. Additionally, a set of 2-cell embryos was cultured in 860 μM melatonin in 0.1X MMR solution to promote transjunctional transfer and injected with isotopically labeled methionine and threonine at the 8-cell stage.

Injected embryos were kept in 100% SS and monitored under a stereomicroscope until the 16-cell stage. Individual fabricated microcapillaries were used to aspirate cellular content from identified left D12 and V12 cells from the same embryo, as previously described. Each cell specimen was expelled into micro vials containing 4 μL extraction solution chilled to ~4 °C. Metabolite extracts were vortex-mixed and centrifuged as noted above and kept in –80 °C until CE-ESI-MS analysis.

5.2.5 Metabolite injections and dual-fluorescent cell fate tracking

Individual 2-cell embryos were transferred into a Petri dish containing 100% SS and cultured at 14 ˚C until they reached the 16-cell stage. Then, embryos were transferred into a dish containing 3% ficoll and 100% SS solution and the midline dorsal-animal D11 and D12 cells were identified following established cell fate maps.[58-59] In control embryos, a 2 nL volume of a mixture containing 100 pg/nL green-fluorescent protein (GFP) mRNA was injected into the D11, while 2 nL of 100 pg/nL red-fluorescent protein (RFP) mRNA was injected into the D12. The first experimental group was injected with 2 nL 75 mM methionine in GFP mRNA into the D11, and 2nL of RFP mRNA into the D12 cell. The second experimental group

was injected with 2nL GFP mRNA into the D11 cell, and 75 mM methionine in RFP mRNA into the D12 cell. Each control and experimental group consisted of ~50 injected embryos. Approximately 20 min after the injection, embryos were transferred into Petri dishes containing 50% SS and monitored until they reached the larval stage. At stage 34, the larvae were fixed using 4% paraformaldehyde and 3% sucrose in phosphate-buffered saline (PBS) solution for 1 h. Finally, the fixed larvae were rinsed with 1× PBS solution and stored at 4 °C.

5.2.6 Phenotyping

Larval stage embryos (stage 34) were imaged using a confocal microscope (Leica SP5X, Buffalo Grove, IL). To conduct lineage analysis, embryos were examined and imaged using epifluorescence on a research-grade stereomicroscope (model SMZ18 equipped with SMZ-25/18 P2-EFLC EGFP BP HC Filter Set, Nikon, Melville, NY). The relative contribution of fluorescence to the organ/tissue fate was scored following original guidelines used to determine cell fate maps.[58] The scoring was assigned as follows, a "0" indicated no labeled cells in the tissues of interest; "1" indicated ≤ 10 labeled cells; "5" indicated at least 50% labeled cells; and "10" indicated that the tissue was entirely covered by labeled cells. To compare differences between control and experimental dual-fluorescent labeled cells, two-tailed Mann-Whitney U test and student's t-test were calculated in OriginPro 2016 (OriginLab, Northampton, MA) with a significance level of 0.05.

5.2.7 Metabolite detection

Metabolite extracts were centrifuged at 8 000 ×g at 4 °C for 5 min to pellet cell debris and precipitated proteins before analysis in a laboratory-built CE-ESI-MS platform as previously described.[12, 55, 100] Briefly, the laboratory-built CE stage comprised of a 1-meter fused silica capillary (40/102 µm inner/outer diameter) with the capillary inlet submerged in background electrolyte (BGE) containing 1% (v/v) formic acid, and the outlet connected to a co-axial sheath-flow interface that supplied sheath liquid at 0.6 µL/min. Electrophoretic separation of small molecules was conducted by applying 18–20 kV. Generated ions were analyzed using a quadrupole orthogonal-acceleration time-of-flight mass spectrometer (Impact HD, Bruker Daltonics, Billerica, MA) with the following settings: –1,700V spray voltage (applied to the front plate orifice); MS survey scan rate, 2 Hz; mass range (MS1 and MS2), *m/z* 50–550; collision-induced dissociation (using nitrogen gas) energy, 18–20 eV; dry gas, 100 °C with a flow rate 2 L/min.

5.2.8 Data analysis

Raw mass spectrometric data files were processed in Compass Data Analysis version 4.3 (Bruker Daltonics) using a custom-written data analysis script.[12] Each data file was externally mass-calibrated (enhanced quadratic calibration in Compass) for sodium-formate cluster ions that formed in the ESI source. Molecular features (unique m/z vs. migration time domains) were semi-automatically searched between *m/z* 50–550 with a 5 mDa window and their accurate mass and selected-ion peak area were manually recorded. The metadata were further evaluated in MetaboAnalyst

4.0[120] with the following settings: normalization by sum; log transformation; data auto scaling. Unsupervised principal component analysis (PCA), statistical tools (e.g., T-test, ANOVA, etc.) and hierarchical cluster analysis (HCA) were performed on MetaboAnalyst using statistically significant features ($p<0.05$) and Euclidean distance measure. Cluster analysis was performed in GProX ver.1.1.16[174] with the following settings: cluster number, 0-4; upper limit, 1.5; lower limit, 0.75; fuzzification value, 2; minimum membership for plot, 0.5; standardizations and 100 iterations.

5.2.9 Color preference behavioral assay

To test the visual function of *Xenopus laevis* tadpoles (stage 45) after methionine injection into dorsal D11 and D12 cells, a color preference behavioral assay was conducted following a previously established protocol.[175] All protocols related to the maintenance and handling of *Xenopus laevis* tadpoles were approved by the University of Maryland Institutional Animal Care and Use Committee (IACUC no. R-JUN-20-31). Two cell embryos were collected in a Petri dish containing 100% SS and cultured at 14 ˚C until they reached the 16-cell stage. The control group (n = 15) consisted of wild-type 16-cell embryos cultured in 50% and 20% SS at room temperature (20–21 °C) to stage 45. Experimental groups consisted of metabolite-injected clones of corresponding D11 and D12. A volume of 2 nL of L-methionine was injected into D11 (n =10) or D12 (n =15) cells in separate embryos at the following concentrations: 75 mM (1×) and 150 mM (2×). Injected embryos were transferred to 50% SS and cultured at room temperature until they reached tadpole stage 34. At stage 45, tadpoles were transferred to Petri dishes containing 20 % SS.

The "*test tank*" consisted of two-tanks: an outer tank with one half covered with black electrical tape and the second half covered with white paper, and an inner tank filled with 20% SS at ~5 cm height. Next, a camera (Canon EOS 70D, Canon USA, Huntington, NY) was placed on a tripod and adjusted to visualize the testing area. A lightweight white cloth was placed over the setup to reduce external lighting and maintain luminance between 40–50 cd/m^2.

Using a large-aperture pipette, an individual tadpole was carefully transferred to the white-side of the "*test tank"*. Immediately, the first trial was recorded using the camera setup for 2 min. Then, the inner tank was rapidly elevated while the outer tank was rotated 180° and placed back into the outer tank. A second trial was recorded for 2 min, then the tadpole was returned to a dish containing 20% SS. Control and experimental groups were tested on 2 consecutive days. After the trials were finished, the recordings were manually analyzed by noting down the amount of time individual tadpoles spent on the white side of the tank. The position of the tadpole was determined based on the location of the eyes. A tadpole was considered to cross the black/white line only when both eyes were found on either black or white locations. The data was analyzed using two-tailed Mann-Whitney U test calculated in OriginPro 2020 (OriginLab, Northampton, MA) with a significance level of 0.05.

5.3 Results and discussion

5.3.1 Microprobe sampling of cells in the same embryo uncovered metabolite gradients

The goal of this work was to characterize metabolites among cells in the same vertebrate embryo. We recently adapted and validated microprobe microsampling to conduct *in situ* and temporal analysis of the metabolome in dorsal embryonic cells from 8−32 cell stages of the *Xenopus laevis* embryo.[55, 101] Although only a small portion of the cell was extracted, it was demonstrated that microprobe sampling is able to detect a comparable number molecular features (unique *m/z* and migration time) compared to a microdissection workflow.[12] Additionally, microprobe sampling minimized oxidative stress and physical damage caused to neighboring cells while collecting inner cellular content. In this study, I targeted four adjacent cells in the 16-cell South African *Xenopus laevis* frog embryo (Fig. 5.1), a well-established model in cell and developmental biology. Animal dorsal-ventral cells located on the left side of the embryo were exclusively sampled since a previous study conducted by the Nemes lab uncovered left-right metabolic asymmetry in the 8-cell embryo.[57] Moreover, these cells were strategically chosen because they are fated to develop into distinct tissues and organs as determined by corresponding cell fate maps.[58] For example, the D11 cell gives rise to part of the central nervous system, including the brain and retina, while the D12 cell reproducibly gives rise to the spinal cord, otocyst and head epidermis. On the other hand, the V12 cell forms part of the neural crest, and the V11 cell gives rise to the head and trunk epidermis. Figure 5.1 demonstrates how we

utilized fabricated borosilicate micropipettes (μP) with a needle-tip outer diameter of ~20 μm to extract a small portion of cellular content 10–15 nL from individual cells. Importantly, after microsampling individual cells of the 16-cell embryo, there was minimal damage observed among the cells. Next, the extracted portion of the cell was immediately transferred to a microvial containing 4 μL of metabolite extraction solvent as described in the experimental section. Metabolite extracts form each cell were measured using our customized single-cell CE-ESI-MS platform[12, 100-101] and the resulting metadata was analyzed to interpret metabolite heterogeneity among dorso-ventral cell types.

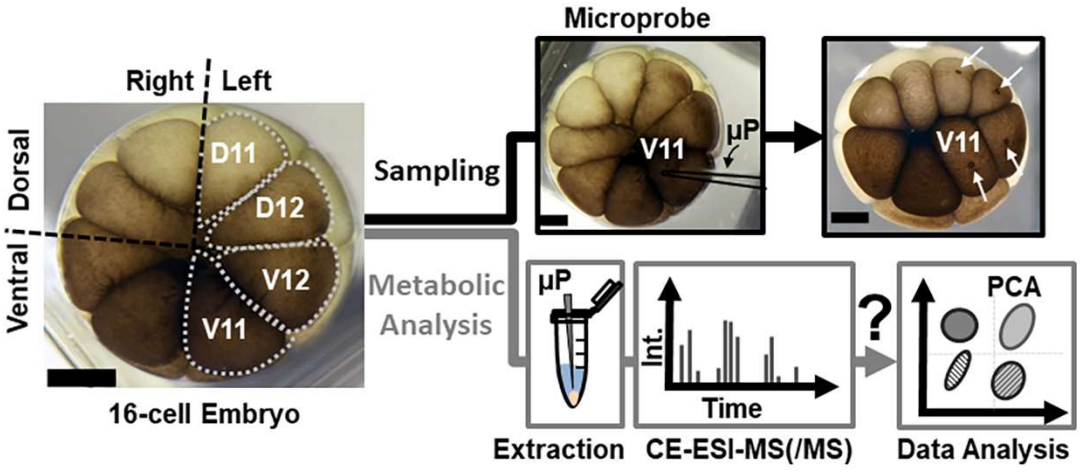

Figure 5.1 Analytical pipeline enabling the metabolic differentiation of dorsal and ventral single cells in a live embryo. A ~10 nL portion of cytoplasm from D11 (neural fate), D12 (head epidermis fate), V12 (cranial ganglia and epidermis fate), and V11 (head and truck epidermis fate) *X. laevis* embryonic cells were aspirated using a microprobe (μP). Samples were analyzed by CE-ESI-MS. Scale = 250 μm.

Using CE-ESI-MS, we detected about ~140 distinct molecular features in single-cell extracts, from which 90 were identified as metabolites (Appendix 5.1). Metabolite identification protocols are described in Chapter 2. Briefly, confident

metabolite identification was conducted by comparison of accurate masses to a database (e.g., METLIN[43] and HMDB[3]), comparison of migration time (MT) to one of a known metabolite standard, and comparison of tandem-MS patterns to chemical standards or available spectra in online databases. To compare the relative abundance of detected molecular features among dorso-ventral cell types, we used under-the-curve peak area as a proxy to metabolite concentration.

Next, we conducted unsupervised principal component analysis (PCA) based on ~140 molecular features from n = 3 embryos of same parental origins (Fig. 5.2A), which revealed no discrete clustering of the D11, D12, V12 and V11 cell types based on the their corresponding metabolite profiles. This result was in agreement with previous findings that suggest the existence of embryo-to-embryo metabolic heterogeneity during the cleavage stages of embryonic development.[13] Surprisingly, when comparing technical triplicates measured by CE-ESI-MS using PCA, a distinct clustering based on cell types was observed (Fig. 5.2C), which indicates that cell type differences at the level of metabolites could be masked by embryo–embryo differences. Consequently, we performed unsupervised hierarchical clustering analysis (HCA) (Fig. 5.2B) of the 75 most statistically significant molecular features determined by analysis of variance ANOVA. Interestingly, HCA showed differential clustering based on cell types (top axis) and relative metabolite abundance (left axis). For example, in the case of the arginine-alanine (Arg-Ala) and serine-alanine (Ser-Ala), their corresponding concentration pattern indicates higher concentration of both in V11 (highest) and D12 cells , while a lower in D11 and V12 (lowest) was determined. Additionally, Figure 5.2B reveals a large group of metabolites (e.g.,

histidine, choline) with similar concentration trends where the highest concentration is found in D12 and V12 cells, and the smallest concentration is found in D11 and V11 cells. This result indicates that microprobe CE-MS is amenable to uncover spatial concentration gradients between adjacent dorsal-ventral cells in the 16-cell embryo.

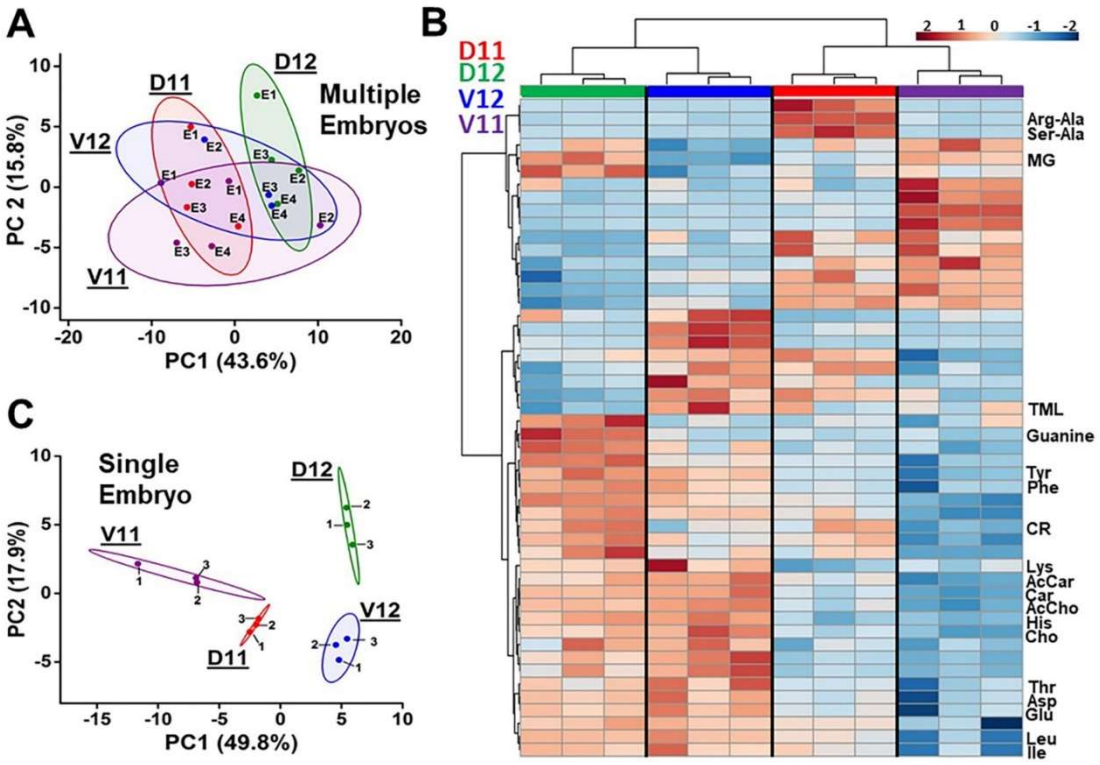

Figure 5.2 Overall differences between embryos can mask cell-to-cell differences in the metabolome. (A) PCA shows overlap between cell types (V11, V12, D11, and D12) when comparing multiple embryos. (B) Hierarchical clustering−heatmap shows the technical reproducibility achieved per measurement of each cell type. (C) Cell types can be differentiated via PCA when looking at the metabolite distribution of an individual embryo. Key: AcCar, Acetylcarnitine; AcCho, Acetylcholine; Car, Carnitine; Cho, Choline; CR, Creatine; TML, N6,N6,N6-trimethyl-lysine.

5.3.2 Dorso-ventral metabolite transport and modulating GJC

An unsupervised data clustering and visualization tool such as GProx,[174] (Fig. 5.3A) was used to generate and interpret metabolite concentration patterns across left dorso-ventral cells. A total of 84 molecular features were grouped into 4 different clusters based on their corresponding spatial abundance from the D11 cell towards the V11 cell. A complete list of molecular features and assigned cluster groups is presented in Appendix 5.2. Molecular features allocated to cluster 0 represent molecules found at a steady concentration across all cells. Interestingly, clusters 1 and 2 follow similar concentration patterns, as the highest metabolite concentration was found in the D11 cell and progressively decreasing in abundance towards the D12, V12, and V11 cells. However, in cluster 1 the lowest concentration is located at the V12 cell whereas cluster 2 shows a low concentration at the V11 cell. Cluster 3 presents a reversed pattern as compared to cluster 1, with the lowest molecular abundance found in the D11 cell and the highest at the V12 cell. Finally, cluster 4 depicts a unique pattern where both the D11 and V11 cells contain the highest level of metabolites. At first glance, the concentration gradients observed across dorso-ventral cells could result from various developmental processes taking place during *X. laevis* embryogenesis. Due to the similarities in metabolite concentration trends between clusters 1 and 2, we hypothesized that these gradients could be a product of intercellular communication via gap junction channels that regulate metabolite transport between cells.[176] Recent measurements in 16- to 64-cell *X. laevis* embryos[170, 177-178] revealed that dorsal blastomeres have greater gap junctional communication (GJC) than ventral embryonic cells; thus, it is possible that the spatial

distribution captured by microprobe CE-ESI-MS reflects on dorso-ventral metabolite transfer in the embryo.

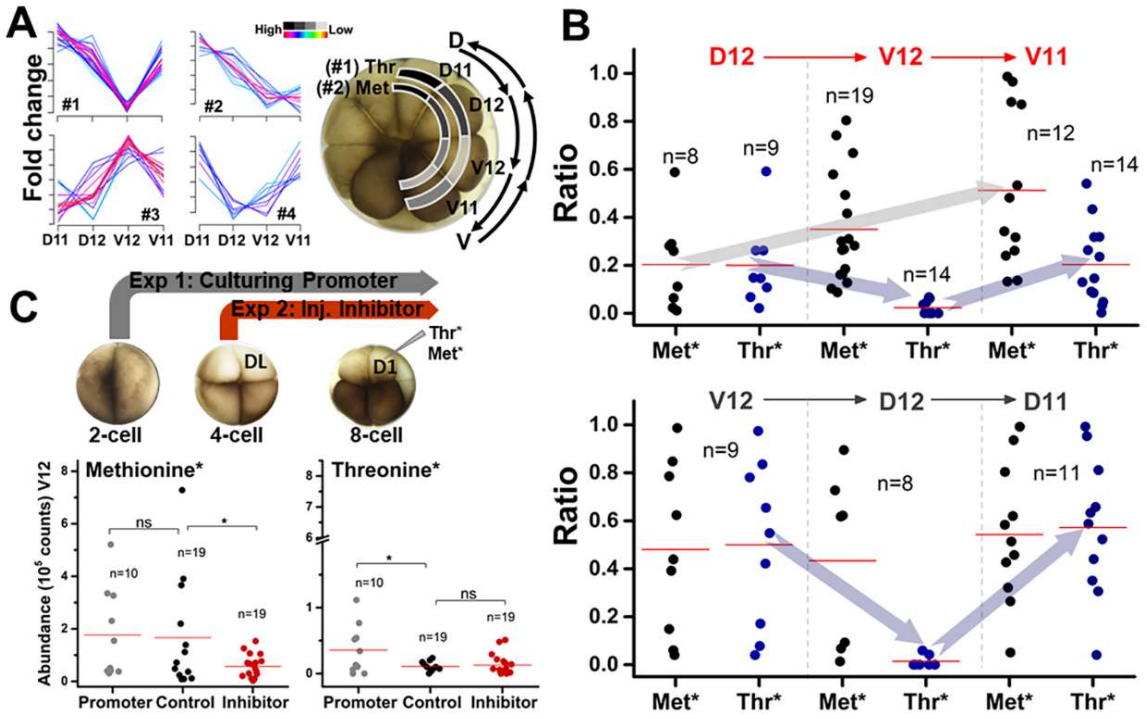

Figure 5.3 Metabolite gradients and transport across dorso-ventral cells. (A) Unsupervised cluster analysis of small-molecular features in adjacent cells of the 16-cell X. laevis embryo. (B) Determining transport of metabolites mediated by gap junctions using stable-isotopically labeled methionine and threonine. (C) Modulating junctional transfer between by introducing inhibitor and promoter molecules. Key: ns- not significant.

To test our hypothesis that GJC may be at play to create metabolite gradients in the 16-cell embryo, we developed a strategy where stable isotope metabolites are injected into target cells followed by single-cell CE-ESI-MS analysis. For example, isotopically labeled threonine (cluster 1) and methionine (cluster 2) were co-injected as a mixture into the D11 cell, then the embryo was cultured for 10–15 min and microprobe sampling was used to collect a portion of the D11 and D12 cell for single-

cell CE-ESI-MS analysis. Next, the isotopically labeled metabolite mixture was injected into the D12 cell in a separate group of embryos and later sampled at the D12 and V12. Finally, we injected the metabolite mixture into the V12 cell to investigate the small molecule transfer between V12 and V11 cells, as seen in Figure 5.3B. A ratio (Equation 5.1.) was used to calculate whether isotopically labeled threonine or methionine had migrated between neighboring cells, as follows:

$$\text{Ratio} = \frac{\text{Peak intensity (Thr* or Met*) injected cell}}{\sum \text{Peak intensity (Thr* or Met*) microrpobed cell}} \qquad \text{(Equation 5.1)}$$

For instance, if the isotopically labeled metabolites were injected into the D11 cell and both D11 and D12 cells were sampled and analyzed; then a ratio of 1 following Equation 5.1 would indicate no metabolite transport to the adjacent cell, while 0 would indicate total transfer of the metabolite. Remarkably, we found that methionine transport is favored between dorsal, dorso-ventral, and ventral cells (Fig. 5.3B). On the other hand, threonine followed a similar pattern where metabolite transport was detected between dorsal and ventral cells, but no transfer was detected between dorso-ventral D12 and V12 cells. This observation is consistent with the metabolic concentration profile displayed by cluster 1 (Fig. 5.3A). Additionally, we investigated metabolite transfer from V11 cell in the direction towards the D11 cell (Fig. 5.3B, bottom). Interestingly, it was found that threonine does not migrate in a ventral-to-dorsal directionality. Our observations of small-molecule transfer between dorsal cells in the 16-cell embryo are in agreement with previous studies that characterized GJC using small and large molecular weight fluorescent dyes.[170, 179]

To further characterize the extent of small molecule transfer via GJC, we treated embryos with drugs known to inhibit junctional conductance such as carbenoxolone,[180] and melatonin[170, 181] which facilitates GJC (Fig. 5.3C). Embryos in the 4-cell stage were injected with carbenoxolone into the DL cell, then co-injected with isotopically labeled methionine and threonine into the D1 cell, and finally microprobed into D12 and V12 cell in the 16-cell embryo. Our results show that the addition of carbenoxolone significantly reduces the transfer of methionine towards the V12 cell. There was no change in the transfer pattern previously observed with threonine. A second set of embryos were cultured in a solution containing melatonin at the 2-cell stage, co-injected with isotopically labeled metabolites, and microprobed into the D12 and V12 cells. Adding melatonin into the culturing media significantly increased the transfer of threonine into the V12 cell. Overall, our collective results suggest that metabolite gradients observed in the 16-cell *X. laevis* embryo could indeed result from GJC. Moreover, previous studies demonstrated that gap junctional communication variations effectively take place during early embryogenesis; thus, junctional permeability plays an important role in establishing the orientation of body axes.[170, 179]

5.3.3 Tracking cell fate changes in adjacent neural-precursor cells

In the last decade, several studies have focused on understanding the mechanisms that allow the vertebrate embryo to reliably self-assemble via body patterning.[172] Given the complexity of the underlying events that take place during embryogenesis, it is believed that receptor-mediated signal exchange plays a major

role to enable information flow between cells and tissues. Therefore, direct cell-to-cell exchange of small molecules through gap junctions is essential to establish communication between neighboring cells.[182] This notion is supported by the findings in this study, where we discovered the effective transfer of methionine between dorso-ventral cells in the 16-cell *X. laevis* embryo. In Chapter 4, I investigated cell fate changes caused by injection of methionine and acetylcholine into the dorsal D11 cell. Since our earlier work demonstrated that injecting methionine into the neural-fated D11 cell causes a decrease in fluorescent lineage of cells that form the brain, lens, and olfactory placode; we hypothesized that the cell fate of the neighboring D12 cell may also be affected due to junctional transfer of methionine.

To test our hypothesis, we performed dual-fluorescent labeling of D11 and D12 cells in the same embryo by injecting two fluorescent-protein mRNA lineage tracers. A control group consisted of 16-cell embryos injected with green-fluorescent protein (GFP) into the D11, and red-fluorescent protein (RFP) into the D12 to trace cell fates in the larval stage 34 (Fig. 5.4). In the first experimental group, a mixture of methionine and GFP was injected into the D11 cell to induce an epidermal cell fate, while D12 was injected with RFP. Finally, a mixture of RFP and methionine was injected into the D12 cell, while the D11 cell was fluorescently traced with GFP. Bright-field and fluorescent microscopy was used to score the relative cell contribution to brain, retina, lens, spinal cord, olfactory placode, cement gland, otocyst, branchial arches, and epidermis following established protocols.[58] We performed statistical analysis using tissue scores to evaluate significant differences

(p-value <0.05) between control and experimental groups. Table 5.1 summarizes statistical p-values obtained after performing student's t-test using tissue scores.

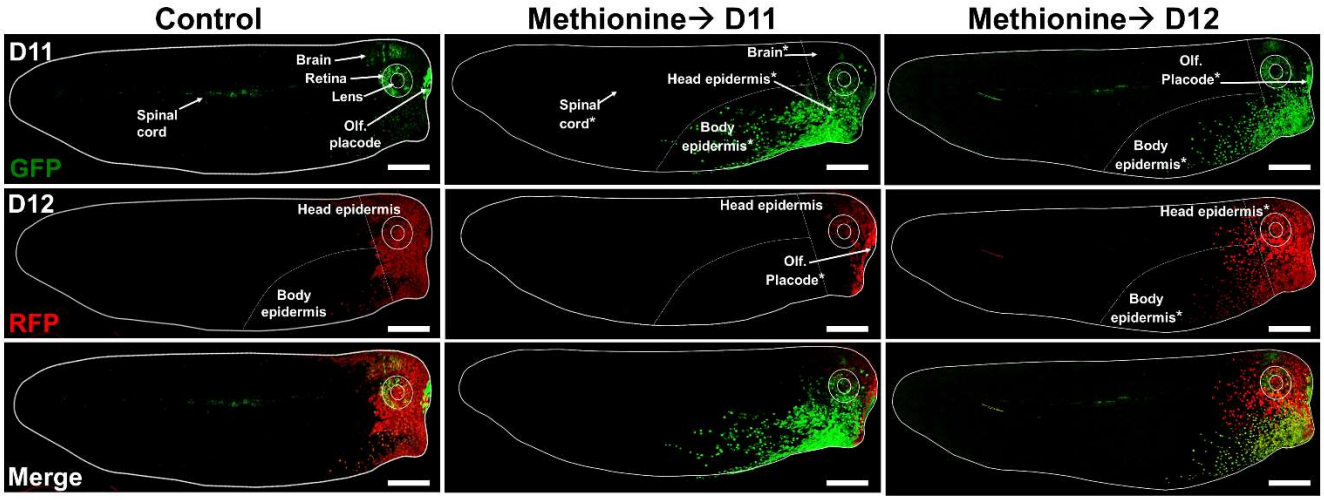

Figure 5.4 Dual-fluorescent labeling of dorsal cell clones in *X. laevis* larva (stage 34). Methionine injection into the D11 and D12 cells revealed cell fate changes to corresponding neighboring cells. Scale bar = 200 µm.

Our results demonstrate that injection of methionine into the D11 and D12 cell can induce cell fate changes on the immediate dorsal-adjacent cell (Fig. 5.4). For example, upon injection of methionine into the D11 cell, fluorescently derived cells of the D12 (red, RFP) contributing to the retina, lens, and olfactory placode significantly decrease. Similarly, injection of methionine into the D12 cell shows a notable effect in the formation of brain, lens, spinal cord, and olfactory placode derived from D11 cell clones (green, GRP). Thus, the data provided herein validate our notion that altering methionine concentration in dorsal cells coupled with junctional communication in the early *X. laevis* embryo can ultimately intervene with normal cell fate commitment.

Table 5.1 Student's t-test and *p*-values of tissue scores after metabolite injection into D11 or D12 cells in 16-cell *X. laevis* embryos.

Student's t-test	**Methionine into D11**		**Methionine into D12**	
Tissue	*D11*	*D12*	*D11*	*D12*
Retina	0.152	4.9E-04	0.939	0.256
Lens	0.003	0.001	0.041	0.088
Brain	0.013	0.053	0.048	0.609
Spinal cord	0.223	0.602	4.3E-04	0.004
Olfactory placode	0.055	3.3E-06	0.018	0.091
Cement gland	0.059	0.208	0.260	0.175
Otocyst	0.098	0.817	0.074	0.065
Branchial arches	0.719	0.655	0.057	0.403
Head epidermis	0.002	0.510	0.861	0.014
Body epidermis	5.9E-05	0.550	0.186	0.017

5.3.4 Behavioral assay on metabolite-injected tadpoles reveals visual deficit

Last, we measured the visual function of *X. laevis* tadpoles injected with methionine at the 16-cell stage using an recently established color preference behavioral assay for *Xenopus laevis* tadpoles.[175] Since D11 and D12 cells give rise to neural structures such as the retina, lens, and brain; we tested whether methionine injection into individual cells at 1× and 2× concentrations (see experimental section) impairs visual function at tadpole stage 45. Control or wild-type tadpoles were selected at the 2-cell stage and cultured at room temperature until the tadpole stage. Experimental groups were injected into D11 and D12 cells with methionine in 1× and 2× concentrations, correspondingly. Then, tadpoles were placed in a test tank consisting of a half-tank covered in white, while the second half is covered in black (Fig. 5.5A). In previous studies, it was noted that when placing a tadpole in a half-black/half-white tank, pre-metamorphic *X. laevis* tadpoles (stage 45) quickly swim to

the white side of the tank.[183] Based on this notion, we expected that tadpoles with intact visual function would prefer to swim towards the white side of the test tank.

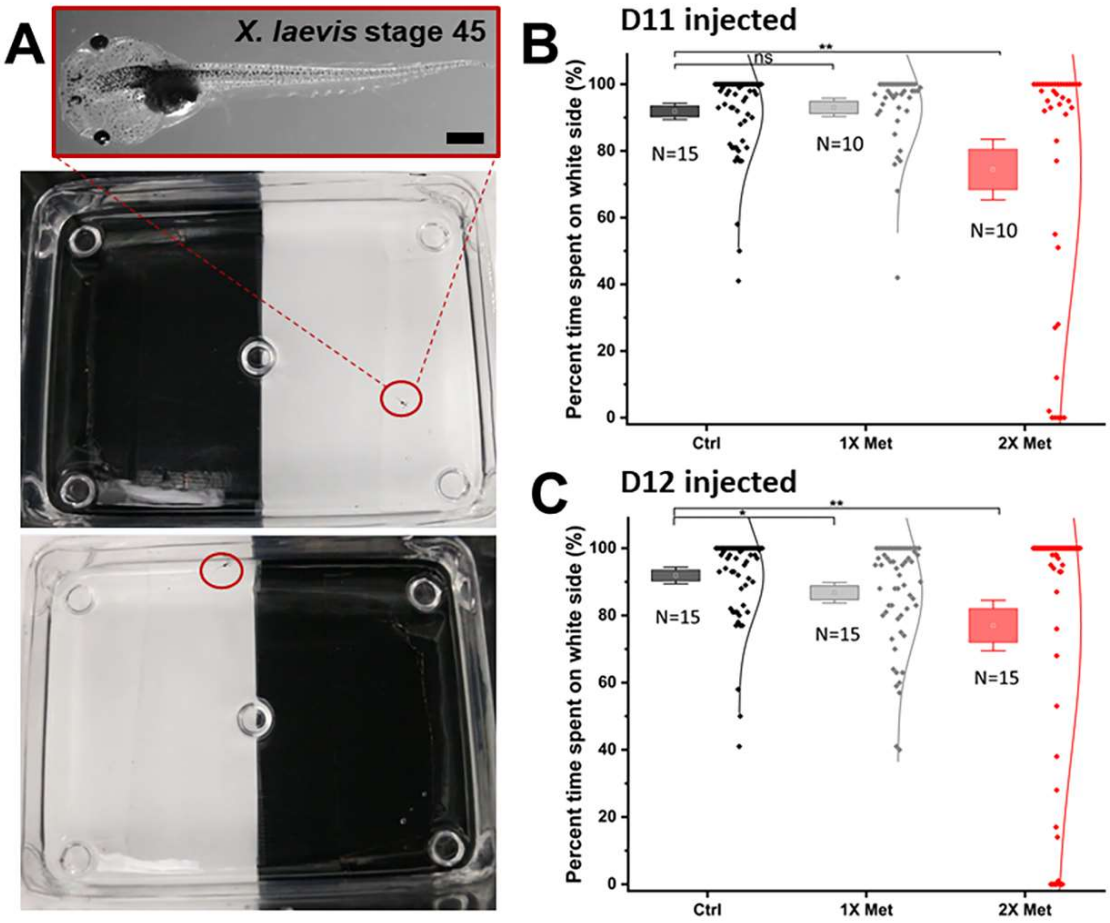

Figure 5.5 Color preference behavioral assay performed to test visual function of *X. laevis* tadpoles (stage 45). (A) Test tank consisting of half-white and half-black background color. (B) Methionine was injected into the D11 cell in 1× and 2× doses. Statistical analysis reveals a deficit in visual function in tadpoles receiving a 2× metabolite injection. (C) Injection of 1× and 2× doses of methionine into D12 cell causes visual deficit in tadpoles. Scale bar = 1 mm.

Our preliminary results (Fig. 5.5B) indicate that a 1× injection of methionine into the D11 cell (n = 10) does not seem to affect visual function in *X. laevis* tadpoles, since the percentage of time spent on the white side of the tank is comparable to the control (untreated) group (n = 15). However, a 2× dose of methionine (n = 10) shows a significant decrease in the amount of time tadpoles spent on the white side of the tank. On the other hand, 1× (n = 15) and 2× (n = 15) methionine injections into the D12 cell (Fig. 5.5C) show a significant deficit in visual function of injected tadpoles due to the reduction of time spent on the white side of the tank. To avoid a directionality bias (e.g., by placing the tadpole on one side of the tank only), we tested each tadpole by placing it on the right side of the tank and sequentially rotating the tank to expose the tadpole to the opposite side (Fig. 5.5A). Additionally, tadpoles were tested during two consecutive days to ensure the reproducibility of our measurements. Interestingly, the results obtained with the color-preference behavioral assay described in this work suggest that visual function of *X. laevis* tadpoles could be impaired upon injection of methionine into neural-fated dorsal cells of the 16-cell embryo.

5.4 Conclusions

In this work, we demonstrated that microprobe can be effectively used to enable the analysis of multiple cells in the same embryo. We also uncovered embryo-to-embryo metabolic heterogeneity and have minimized statistical and biological variability that could hinder the analysis of cell heterogeneity in the developing frog embryo. The resulting data uncovered metabolite concentration gradients across

dorso-ventral cells in the 16-cell embryo resulting from possible metabolite exchange through gap junctional communication (GJC). Remarkably, we found that methionine transport between neural-fated dorsal cells can alter their corresponding tissue fates, further validating the importance of GJC for early embryonic development and organogenesis. Finally, the preliminary results obtained from a color-preference behavioral assay indicate that perturbing methionine abundance in dorsal cells can cause visual deficits in *X. laevis* tadpoles.

Chapter 6: Conclusions and future directions

6.1 Advancing single-cell metabolomics and developmental biology

Single-cell metabolomics by MS provides a powerful tool to study molecular mechanisms responsible for cell heterogeneity. Classical MS-based analytical workflows are designed to characterize biomolecules in bulk cell populations (e.g., tissues, blood, etc.) but it has been observed that cell populations are not necessarily homogeneous.[64, 184-185] Therefore, to understand the chemical diversity between cell types and subtypes, it is important to conduct molecular profiling at the single cell level. To this end, several analytical approaches have been refined to enable single-cell metabolomics. However, due to the large chemical diversity, fast turnover rates of the metabolome, and limited sample volume afforded by single cells, there is still a need to improve current technologies.

The work presented herein accomplished several technological advances towards the analysis of metabolites in single cells of the vertebrate *X. laevis* embryo. First, we adapted microprobe sampling to enable minimally intrusive sample collection of ~10–15 nL content from *X. laevis* embryonic single cells[55] (Chapter 2). This microprobe sampling methodology was compatible with the morphologically complex structure of the vertebrate embryo. Additionally, based on the effectiveness demonstrated by microprobe to collect sample from the live embryo, we utilized this approach to interrogate temporal (Chapter 4) and spatial cell heterogeneity (Chapter 5). Next, we advanced a laboratory-built CE-ESI-MS platform to facilitate the dual analysis of cationic and anionic metabolites from a single cell extract[30] (Chapter 3) to

expand the detectable coverage of the single-cell metabolome. The CE-ESI-MS platform offers high sensitivity, ~5–10 nL (50–100 amol) lower limit of detection, and quantification capabilities to detect endogenous metabolites and neurotransmitters in single cells.

In this work, we demonstrated that combining cell identification using cell fate maps[58-59] with ultra-sensitive CE-ESI-MS, empowers the study of metabolism during early embryonic development. Our results revealed surprising spatial and temporal metabolic cell heterogeneity in the embryo. For instance, we conducted cell lineage studies to determine metabolites and their corresponding concentrations needed to induce cell fate changes (Chapter 4). Then, by profiling metabolites from neural-fated cells of the 16-, 32-cell, stage 8, and 9 embryos, we discovered the reorganization of the metabolome upon injection of select metabolites that induce neural- to epidermal-cell fates. While the active molecular mechanisms that drive metabolite-induce cell fate determination remain elusive to us at this point, our established CE-ESI-MS analytical platform and findings can allow us and others to conceive new hypotheses and research strategies to understand how metabolite heterogeneity contributes to cell specification in the early developing embryo.

Moreover, we uncovered spatial metabolic heterogeneity in the same embryo (Chapter 5) and investigated transjunctional transport of metabolites between adjacent cells. Our findings support previous studies that characterized the importance of gap junctional communication for the establishments of body-axes during embryogenesis.[170, 177] Our data provides new information to understand the role of small molecule transjunctional transfer during body patterning, raising exciting

research possibilities for cell and molecular biology. To validate the significance of cell-to-cell communication and metabolite transport for body patterning and organogenesis, future studies should focus on the development of functional assays that probe and examine metabolite-induced organ development irregularities (e.g., heterotaxia, hypoplasia) during later stages of growth. Results from these and other future experiments are expected to delve into the significance of small molecules for the normal and impaired development of the vertebrate embryo.

6.2 Technological advancements needed for single-cell metabolomics

Improvements in metabolite detection. To facilitate the analysis of metabolites from single cells, I developed a single-cell CE-ESI-MS platform that enables dual anionic-cationic metabolite detection from single cell extracts,[30] with the goal of improving metabolite coverage. This analytical platform was able to detect ~250 cationic and ~200 anionic molecular features from a single cell, including 60 and 24 identified metabolites, respectively. Additional technological advances to our platform may be implemented to aid with metabolite detection and sensitivity to continue improving single-cell metabolite detection. To improve sensitivity, larger amounts of samples can be injected into the CE capillary via sample stacking.[112] This approach is compatible with our platform and likely to yield improved sensitivity for metabolite detection and identification. Improvements in CE interface and spray stabilization will also result in added detection sensitivity. For example, a decrease in sheath-flow from 1 μL to <300 nL/min by incorporating alternative CE-ESI interfaces, such as tapered-tip CE-ESI,[107] electrokinetically pumped low-flow CE-

nanoESI,[108] and even sheathless CE-ESI,[186] will result in reduced dilution of analytes in the electrospray plume. Combined, these suggested improvements can facilitate small molecule detection, which results in a deeper profiling of biomolecules in single cells.

Improvements in throughput. At the moment, a major limitation for the analysis of single cells originates from the minuscule amounts of starting material, which can be lost during sample preparation. Droplet-based isolation[187-188] and microfluidics[18, 189] approaches enable new developments to overcome sample losses and streamline single-cell analytical workflows. For example, by combining single-cell printer technology with liquid-vortex capture (LVC)-MS,[187] a recent study demonstrated high-throughput analysis of metabolites in single cells at a rate of ~30 cells/s. Other approaches utilized stable isotope labeling assisted microfluidics chip ESI[190] to detect and quantify metabolites from individual cells. Based on the advantages achieved by microfluidic devices, our CE-ESI-MS platform could benefit from further advancements and added automatization for sample handling and injection to streamline analysis.

Additionally, to enable the rapid analysis of multiple cells using our CE-ESI platform, a multi-segmented sample injection[113] into the CE separation capillary can significantly boost the analysis throughput of metabolite extracts. Due to the difference in migration of charged compounds through the CE capillary, which is driven by their distinctive electrophoretic mobility, adequate peak resolution remains unaffected for up to 7–10 sample segments. The advantage of adapting this approach

is that the analysis time can be significantly reduced, thus leading to a fast analysis of a larger number of cells.

Improvements in data analysis. In contrast to chromatographic-based separation techniques (e.g., LC), open-access software tools to effectively select peaks (peak-finding) and correct shifts in migration times are still underrepresented in CE-MS based metabolomics. We recently developed Trace,[191] which uses machine learning to enhance signal detection in CE high-resolution MS analysis and demonstrated high accuracy and robustness in data processing throughput for a metabolomics workflow. Trace is compatible with open-source MS data format (mzML) and its python code is conveniently accessible. Further improvements including the implementation of a graphical user interface will facilitate its routine use in CE-MS data analysis workflows. Other software tools such as ROMANCE[192] have focused on correcting migration time shifts by converting migration time into effective electrophoretic mobility. The use of electrophoretic mobility raises the potential to aid compound identification in biological samples. For example, in a study comprised of 13 independent laboratories, including our lab, we recently examined migration time reproducibility and identification capabilities in CE-MS based metabolomics.[193] The results revealed that the reproducibility of the electrophoretic mobility for 20 out of 21 model compounds was below 3.1% vs 10.9% with migration time, regardless of the huge heterogeneity in experimental conditions and platforms across the 13 laboratories. Overall, our findings validate the use of CE-MS as a reproducible approach for metabolomics. As such, we expect that future developments of software tools will continue to move the field onwards.

Appendices

Appendix 4.1 Mann–Whitney U test comparing tissue scores after metabolite injection into D11 or V11 cells in 16-cell *X. laevis* embryos. Key: U, total range; Z, normal distribution test; IQR, interquartile range.

Control vs. Acetylcholine in D11	**Brain**	**Retina**	**Lens**	**Olfactory Placode**	**Cement Gland**	**Branchial Arches**	**C. Somite**	**Epidermis**
U	4180	4090	3644	3846	4055	2920.5	4328	2327
Z	3.6607	3.3153	1.7814	2.4800	3.2498	0.7269	4.2053	–1.6838
Exact. Prob.	2.21E–04	7.91E–04	0.0757	0.0131	0.0011	0.4668	1.93E–05	0.0944
Approx. Prob.	2.52E–04	9.16E–04	0.0749	0.0131	0.0012	0.4673	2.61E–05	0.0922
Median control	5	5	10	5	1	0	5	1
Median AcCho	5	1	1	1	0	0	5	5
IQR control	1–10	1–10	0–10	1–10	0–5	0–1	1–10	0–5
IQR AcCho	1–5	0–5	0–10	0–10	0–1	0–1	1–5	0–5
Control vs. Methionine in D11	**Brain**	**Retina**	**Lens**	**Olfactory Placode**	**Cement Gland**	**Branchial Arches**	**C. Somite**	**Epidermis**
U	3666.5	3175	3372	3732	3780	2272	3199	2452.5
Z	3.3593	1.4380	2.2757	3.6227	3.8625	–0.8071	1.5439	0.0174
Exact. Prob.	7.17E–04	0.1534	0.0229	2.60E–04	9.18E–05	0.4249	0.1235	0.9873
Approx. Prob.	7.81E–04	0.1505	0.0229	2.92E–04	1.22E–04	0.4196	0.1226	0.9861
Median control	5	5	10	5	1	0	5	1
Median Met	1	5	1	1	0	0	5	1
IQR control	1–10	1–10	0–10	1–10	0–5	0–1	1–10	0–5
IQR Met	1–5	0–10	0–10	0–5	0–1	0–5	1–10	0–10
Control vs. AcCho + Met in D11	**Brain**	**Retina**	**Lens**	**Olfactory Placode**	**Cement Gland**	**Branchial Arches**	**C. Somite**	**Epidermis**
U	4585.5	3723.5	4110.5	4070	4346.5	2338	4655	2068
Z	3.4009	0.5770	1.8740	1.7353	2.6413	–0.5064	3.6358	–1.6385
Exact. Prob.	6.27E–04	0.5682	0.0610	0.0823	0.0081	0.6116	2.41E–04	0.1029
Approx. Prob.	6.72E–04	0.5639	0.0609	0.0827	0.0083	0.6126	2.77E–04	0.1013
Median control	5	5	10	5	1	0	5	1
Median AcCho+Met	5	5	5	5	1	0	5	3
IQR control	1–10	1–10	0–10	1–10	0–5	0–1	1–10	0–5
IQR AcCho + Met	1–5	0–10	0–10	0–10	0–5	0–5	1–5	0–5

Control vs. Serine in V11	Retina	Lens	Brain	C. Somite	Olfactory Placode	Cement gland	Branchial arches	Head epidermis	Body epidermis
U	1350	1499	1144	1087	1441	1352	1314	1360	1324.5
Z	1.0928	2.001	–1.9953	–2.0311	2.1284	1.5168	0.5475	0.7849	0.5089
Exact. Prob.	0.4149	0.0514	0.1057	0.0439	0.0484	0.1952	0.5974	0.4205	0.6139
Aprox. Prob.	0.2745	0.0454	0.0460	0.0423	0.0333	0.1293	0.5840	0.4325	0.6108
Median control	0	0	0	0	0	0	0	5	5
Median Ser	0	0	0	0	0	0	0	5	5
IQR control	0–0	0–10	0–0	0–0	0–0	0–0	0–1	1–10	1–5
IQR Ser	0–0	0–5	0–0	0–0	0–0	0–0	0–0	5–5	1–5
Control vs. Threonine in V11	**Retina**	**Lens**	**Brain**	**C. Somite**	**Olfactory Placode**	**Cement gland**	**Branchial arches**	**Head epidermis**	**Body epidermis**
U	696	1411	572	799	818	945	803	928	1187
Z	–3.4585	3.1021	–5.1747	–3.1833	–2.3504	–1.5150	–2.3874	–1.2503	0.8944
Exact. Prob.	5.19E–4	0.0016	3.12E–8	0.0015	0.0189	0.1586	0.0168	0.2138	0.3733
Aprox. Prob.	5.43E–4	0.0019	2.28E–7	0.0015	0.0188	0.1298	0.0170	0.2112	0.3711
Median control	0	0	0	0	0	0	0	5	5
Median Thr	5	0	0	0	0	0	1	5	5
IQR control	0–0	0–10	0–0	0–0	0–0	0–0	0–1	1–10	1–5
IQR Thr	0–10	0–0	0–1	0–1	0–5	0–0.5	0–5	5–10	1–5
Control vs. Ser + Thr in V11	**Retina**	**Lens**	**Brain**	**C. Somite**	**Olfactory Placode**	**Cement gland**	**Branchial arches**	**Head epidermis**	**Body epidermis**
U	1004	1663	946	980	1110	1283.5	1016.5	1282.5	1407
Z	–2.5339	2.7280	–3.8221	–3.2507	–1.6777	–0.3998	–2.2804	–0.2593	0.6111
Exact. Prob.	0.0115	0.0070	5.64E–5	5.44E–4	0.0930	0.8128	0.0226	0.7987	0.5456
Aprox. Prob.	0.0113	0.0064	1.32E–4	0.0012	0.0934	0.6893	0.0226	0.7954	0.5411
Median control	0	0	0	0	0	0	0	5	5
Median Ser+Thr	0	0	0	0	0	0	0	5	5
IQR control	0–0	0–10	0–0	0–0	0–0	0–0	0–1	1–10	1–5
IQR Ser+Thr	0–10	0–0	0–1	0–1	0–5	0–0	0–10	5–10	1–5

Control vs. Thr* in D11	Retina	Lens	Brain	C. Somite	Olfactory Placode	Cement gland	Branchial arches	Head epidermis	Body epidermis
U	2628	2662	2794.5	2537.5	2911.5	2740	2132.5	2260	2006
Z	1.1146	1.3046	1.8538	1.0437	2.3417	1.4469	–1.2953	–0.6698	–1.8857
Exact. Prob.	0.2731	0.1944	0.0666	0.2470	0.0195	0.1490	0.1978	0.5063	0.0615
Approx. Prob.	0.2650	0.1921	0.0638	0.2966	0.0192	0.1479	0.1952	0.5030	0.0593
Median control	10	10	10	10	10	1	0	1	0
Median Thr*	10	10	10	10	5	1	1	1	1
IQR control	5–10	6.25–10	5–10	10–10	1–10	0–8.75	0–1	1–5	0–1
IQR Thr*	5–10	0–10	5–10	10–10	0–10	0–5	0–1	1–5	0–1
Control vs. Met* in V11	**Retina**	**Lens**	**Brain**	**C. Somite**	**Olfactory Placode**	**Cement gland**	**Branchial arches**	**Head epidermis**	**Body epidermis**
U	1025.5	1209.5	1051	1071.5	990.5	1045.5	1054.5	1241.5	1230
Z	–1.1383	1.1721	–0.6662	–0.0703	–1.1129	–0.6300	–0.2163	1.3144	1.3034
Exact. Prob.	0.3153	0.2504	0.6804	1.0000	0.3257	0.3577	0.8379	0.1927	0.1894
Approx. Prob.	0.2550	0.2412	0.5053	0.9440	0.2658	0.5287	0.8288	0.1887	0.1924
Median control	0	0	0	0	0	0	0	5	5
Median Met*	0	0	0	0	0	0	0	1	5
IQR control	0–0	0–10	0–0	0–0	0–0	0–0	0–3	1–10	1–5
IQR Met*	0–0	0–1	0–0	0–0	0–0	0–0	0–5	1–5	1–5

Appendix 4.2 Calculated percent isotope abundance (% [M+1]) for dorsal and ventral clones injected with heavy-isotope tracers.

			32-cell												
Metabolite	**m/z**	**Theor. %**	**Dorsal with Thr***			**Dorsal with Thr* + Met**			**Ventral with Met***			**Ventral with Met* +Thr**			
			Bio Rep 1	**Bio Rep 2**	**Bio Rep 3**	**Bio Rep 1**	**Bio Rep 2**	**Bio Rep 3**	**Bio Rep 1**	**Bio Rep 2**	**Bio Rep 3**	**Bio Rep 1**	**Bio Rep 2**	**Bio Rep 3**	**Bio Rep 4**
Ornithine	133.0972	6.36	10.31	-	8.01	7.90	8.69	5.77	17.31	-	-	8.00	2.45	-	9.63
Lysine	147.1128	7.50	5.70	10.08	7.01	6.18	6.34	5.70	7.67	6.95	5.54	6.69	6.78	7.01	6.09
Arginine	175.1190	8.20	9.67	8.43	6.96	6.33	7.21	6.64	4.81	8.83	7.70	6.74	6.58	6.95	5.46
Acetylcarnitine	204.1230	10.50	6.94	-	-	8.55	11.23	9.83	7.17	11.86	10.64	8.83	7.84	7.90	7.42
Glutamine	147.0764	6.30	8.84	-	5.84	5.19	5.61	4.53	5.94	5.88	5.10	4.93	5.89	5.76	4.91
Glutamate	148.0604	6.00	3.04	-	-	4.14	4.17	4.66	2.58	5.26	4.73	3.86	4.12	3.73	3.48
Tryptophan	205.0972	12.85	31.57	-	-	11.34	-	20.42	-	-	23.46	9.08	8.78	-	-
Tyrosine	182.0812	10.35	23.58	-	-							-	1.57	1.79	-
SAM	399.1445	19.60	23.25	-	-	16.70	23.33	14.37	26.38	-	-	15.82	23.06	18.66	3.93
Thiamine	265.1118	15.46	-	13.76	-							18.27	26.13	-	-
Choline	104.1070	5.97	-	5.90	-	1.30	-	-		6.30	6.18	5.19	5.52	2.53	1.71
Acetyllysine	189.1234	9.69	-	12.91	-	-	-	-	-	-	-	-	-	-	-
Urocanate	139.0502	7.37	-	-	4.40	1.48	-	-	-	-	-	4.03	1.49	5.16	-
Asparagine	133.0768	5.27	-	-	59.99	5.98	7.13	5.62	3.90	-	6.03	-	-	-	-
Spermidine	146.1652	8.89	-	-	-	11.70	9.71	10.62	12.40	-	-	9.46	-	9.70	-
Putrescine	89.1073	4.50	-	-	-	1.92	-	-	-	-	-	5.95	-	22.30	-
γ-aminobutyrate	104.0706	4.88	-	-	-	2.14	4.42	4.14	5.13	4.84	4.73	-	-	-	-
Guanine	152.0567	7.34	-	-	-	4.51	7.24	6.10	2.80	6.56	6.87	5.05	5.12	4.97	4.35
Carnitine	162.1125	8.20	-	-	-	5.70	7.22	6.35	-	-	6.29	2.90	3.92	-	-
Creatine	132.0768	5.60	-	-	-	3.78	2.97	3.91	3.93	3.46	3.61	3.37	3.37	2.53	2.57
Argininosuccinate	291.1299	12.72	-	-	-	9.08	-	-	-	-	-	9.05	7.42	2.46	-
Valine	118.0863	5.98	-	-	-	3.04	-	9.59	-	-	-	3.98	4.50	1.14	-
Serine	106.0499	3.80	-	-	-	2.87	7.64	5.55	-	8.02	6.49	1.42	1.38	-	-
Threonine	120.0655	4.92	-	-	-	1.15	-	9.22	7.75	-	-	1.12	2.00	1.47	2.21
Methionine	150.0586	6.70							-	-	13.29	8.14	7.59	-	-
Hypoxanthine	137.0458	7.00	-	-	-	4.72	7.36	5.85				4.54	4.64	2.18	-
Proline	116.0706	5.96	-	-	-	6.08	-	5.11	-	3.85	4.77	4.31	4.98	3.30	1.72
Ser-Val	205.1183	9.73	-	-	-	11.12	-	2.24	-	-	-	14.30	14.86	16.64	21.28
Aspartate	134.0448	4.93	-	-	-	2.37	-	3.19	-	-	3.71	3.78	3.70	3.02	2.50
Glutathione, oxidized	307.0833	14.73	-	-	-	19.18	-	16.43	-	-	-	17.02	21.96	-	-
Glutathione	309.0911	13.13	-	-	-	12.70	-	4.89	-	-	0.28	11.29	11.37	11.77	-
Acetylcholine	146.1176	8.22	-	-	-	-	17.88	-	-	-	-	5.16	5.89	5.10	2.64
Phenylalanine	166.0863	10.30	-	-	-	-	-	-	-	-	-	6.23	6.16	1.39	-

Metabolite	m/z	Theor. %	64-cell											
			Dorsal with Thr*			Dorsal with Thr* + Met			Ventral Met*			Ventral with Met* + Thr		
			Bio Rep 1	Bio Rep 2	Bio Rep 3	Bio Rep 1	Bio Rep 2	Bio Rep 3	Bio Rep 1	Bio Rep 2	Bio Rep 3	Bio Rep 1	Bio Rep 2	Bio Rep 3
Thiamine	265.1118	15.46	10.68	-	-							29.15	12.54	43.48
Spermidine	146.1652	8.89	12.72	5.08	-	-	8.57	10.86	6.59	-	8.22	10.22	-	-
Putrescine	89.1073	4.50				2.34	-	-	2.12	-	-	5.76	-	4.48
Lysine	147.1128	7.50	6.46	7.40	6.81	6.26	6.11	6.44	5.84	7.55	6.91	6.40	5.92	6.42
Arginine	175.1190	8.20	7.92	7.86	12.13	6.68	7.11	7.25	8.41	9.59	4.74	6.45	6.78	6.52
Guanine	152.0567	7.30	0.51	4.31	-	5.10	5.87	6.14	20.51	8.75	2.13	5.01	5.04	4.88
Carnitine	162.1125	8.20	4.88	-	10.43	6.57	6.95	7.48	6.91	-	0.39	5.63	6.63	-
Acetylcarnitine	204.1230	10.50	6.76	5.79		7.81	10.84	10.62	16.67	13.36	3.99	8.05	6.98	7.63
Glutamine	147.0764	6.30	6.90	4.17	6.43	5.44	5.04	5.10	5.50	5.94	5.67	5.06	5.62	5.34
Glutamate	148.0604	6.00	3.20	-	10.46	4.39	4.33	4.11	5.68	-	3.26	4.75	4.88	3.87
Ser-Val	205.1183	9.73	37.59	-	-	10.50	-	-	-	3.01	-	11.62	12.16	14.73
Choline	104.1070	5.97	-	5.69	-	5.93	-	-	-	-	1.96	5.37	5.82	1.80
Ornithine	133.0972	6.36	-	2.90	-	4.40	9.45	-	-	-	18.88	4.70	-	-
Urocanate	139.0502	7.37	-	3.77	-				-	-	-	2.09	-	-
Tryptophan	205.1183	12.85	-	19.01	-	9.80	22.77	20.32	-	-	-	9.29	17.28	-
γ-aminobutyrate	104.0706	4.88	-	-	5.37	-	4.65	4.39	4.13	4.82	-	0.32	-	0.22
Serine	106.0499	3.82	-	-	6.06	1.94	5.85	5.92	-	-	-	2.19	1.46	-
Asparagine	133.0608	5.28	-	-	11.81	8.00	6.61	6.36	3.99	4.08	3.56	4.02	6.18	-
Threonine	120.0655	4.92	-	-	-	0.34	9.80	43.36	-	-	-	2.66	1.50	0.38
Glutathione, oxidized	307.0833		-	-	-	-	-	-	-	-	-	16.87	1.58	20.06
Glutathione	308.0911	13.14	-	-	13.85	11.06	-	-	-	-	-	10.78	7.38	11.47
SAM	399.1445	19.60	-	-	-	18.62	-	19.47	-	-	-	21.97	-	25.01
Ser-Arg	262.1510	11.94	-	-	-	9.52	-	-	-	-	-	12.91	-	-
Acetylcholine	146.1176	8.19	-	-	-	5.49	-	-	-	-	-	5.91	4.74	4.82
Methylaspartate	148.0604	6.04	-	-	-	2.61	-	-	-	-	-	0.49	3.09	-
Creatine	132.0768	5.60	-	-	-	4.01	3.47	3.87	-	-	-	3.68	4.14	3.05
Pro-Val	215.1390	11.87	-	-	-	9.62	-	-	-	-	-	-	19.62	-
Argininosuccinate	291.1299	12.72	-	-	-	12.16	-	-	-	-	-	12.73	4.92	16.44
Valine	118.0863	5.98	-	-	-	4.09	8.54	-	-	-	-	4.82	4.19	1.88
Phenylalanine	166.0863	10.30	-	-	-	8.09	-	6.05	-	-	-	7.66	7.23	6.18
Tyrosine	182.0812	10.35	-	-	-	7.67	-	-	-	-	-	4.49	6.78	-
Proline	116.0706	5.96	-	-	-	3.71	4.62	-	-	-	13.29	4.88	4.22	3.06
Aspartate	134.0448	4.93	-	-	-	3.57	3.17	4.00	-	-	-	3.75	3.82	3.51
Isoleucine	132.1019	7.09	-	-	-	-	15.00	12.3	-	-	-	4.82	1.90	0.60
Leucine	132.1019	7.09	-	-	-	-	11.23	10.5	-	-	-	4.90	-	2.57
Hypoxanthine	137.0458	7.00	-	-	-	-	5.80	5.91	-	-	-	-	4.70	4.01
Methionine	150.0583	6.70	-	-	-	-	-	0.80	-	-	-	9.55	10.46	1.27

Metabolite	m/z	Theor. %	Stage 8												
			Dorsal with Thr*			Dorsal with Thr* + Met			Ventral with Met*			Ventral with Met* + Thr			
			Bio Rep 1	Bio Rep 2	Bio Rep 3	Bio Rep 1	Bio Rep 2	Bio Rep 3	Bio Rep 1	Bio Rep 2	Bio Rep 3	Bio Rep 1	Bio Rep 2	Bio Rep 3	Bio Rep 4
Spermidine	146.1652	8.89	7.52	8.75	8.89	10.70	16.53	7.91	6.68	16.89	9.79	8.79	8.44	7.84	4.93
Putrescine	89.1073	4.50	3.81	-	-	-	-	0.18	2.56	-	-	5.31	5.57	5.74	5.91
Thiamine	265.1118	15.46	-	-	-	-	-	-	7.65	7.39	-	18.19	37.75	20.78	17.88
Choline	104.1070	5.97	4.89	-	-	-	-	2.00	1.64	2.26	5.91	5.51	6.33	2.56	4.59
SAM	399.1445	19.60	32.02	-	-	18.03	-	27.21	44.83	-	-	19.33	23.72	16.90	22.14
Ornithine	133.0972	6.36	6.31	-	-	10.01	-	-	-	-	-	6.15	6.29	6.88	9.05
Lysine	147.1128	7.47	6.24	6.22	7.36	6.50	7.66	7.16	17.53	5.53	8.81	5.99	6.49	6.58	6.33
Arginine	175.1190	8.16	6.41	7.39	8.26	7.31	3.29	5.29	5.83	5.63	5.86	6.32	6.07	6.33	6.83
γ-aminobutyrate	104.0706	4.88	0.85	-	4.85	3.92	-	-	6.04	6.20	6.36	0.29	0.46	-	-
Acetylcholine	146.1176	8.19	0.97	-	-				2.76	1.88	7.69	4.90	4.41	4.69	5.62
Guanine	152.0567	7.30	0.46	-	7.13	6.29	1.88	1.20	3.53	4.25	6.22	4.68	4.80	4.89	5.10
Carnitine	162.1125	8.20	3.18	4.50	10.24	9.42	-	-	6.63	5.60	12.98	5.38	-	-	3.15
Acetylcarnitine	204.1230	10.50	7.50	8.35	15.90	14.11	-	0.96	3.90	3.74	3.90	6.67	6.35	7.29	7.21
Creatine	132.0768	5.60	3.79	4.45	-	3.31	-	-	1.22	1.17	-	3.45	3.58	3.28	3.57
Valine	118.0863	5.98	1.40	-	-	16.08	-	2.95	7.32	8.76	7.19	3.38	3.21	1.30	3.61
Serine	106.0499	3.80	1.64	-	-				13.01	11.02	-	1.32	-	0.93	0.97
Isoleucine	132.1019	7.02	0.28	-	-				21.66	20.11	18.88	3.74	4.27	3.09	3.33
Leucine	132.1019	7.02	0.56	-	-				6.09	6.10	100.17	4.06	4.03	3.17	3.66
Asparagine	133.0608	5.27	8.18	-	-	-	-	5.44	4.93	5.87	118.97	1.88	0.98	-	-
Tryptophan	205.0972	12.85	14.94	-	-	21.22	-	-	7.09	7.46	5.12	8.44	8.61	74.63	-
Glutamine	147.0764	6.30	5.54	5.79	6.22	5.34	8.91	7.04	-	0.75	3.86	5.10	4.99	5.41	5.46
Glutamate	148.0604	6.00	3.21	2.97	-	4.34	1.82	2.97	-	-	5.73	4.34	4.35	3.96	4.06
Hypoxanthine	137.0458	7.00	3.59	3.78	6.55	6.17	-	4.03	-	-	7.37	4.51	4.15	4.08	4.37
Glutathione, ox.	307.0833	26.24	18.80	22.38	21.37	-	-	-	-	-	5.69	-	18.64	4.27	
Glutathione	308.0911	13.13	-	22.13	14.92	-	-	-	-	-	-	10.80	10.18	9.66	11.22
Proline	116.0706	5.96	-	-	-	-	-	-	-	-	-	3.49	3.35	3.26	4.59
Ser-Val	205.1183	9.73	-	-	-	-	-	-	-	-	-	13.23	13.17	14.46	17.13
Aspartate	134.0448	4.93	-	-	-	-	-	-	-	-	-	2.99	2.84	2.93	3.46
Arg-Ala	246.1561	11.90	-	-	-	-	-	-	-	-	-	9.50	14.25	27.26	20.74
Ser-Arg	262.151	11.94	-	-	-	-	-	-	-	-	-	12.31	11.03	16.44	16.56
Homolysine	161.1285	8.57	-	-	-	-	-	-	-	-	-	26.79	25.70	-	-
Argininosuccinate	291.1299	12.72	-	-	-	-	-	-	-	-	-	15.02	6.67	19.97	4.63
Methionine	150.0583	6.77	-	-	-	-	-	-	-	-	-	5.53	2.88	-	5.30
Phenylalanine	166.0863	10.30	-	-	-	-	-	-	-	-	-	7.38	6.08	5.08	4.10
Tyrosine	182.0812	10.35	-	-	-	-	-	-	-	-	-	4.58	5.15	5.17	1.84

Metabolite	m/z	Theor. %	Stage 9											
			Dorsal with Thr*			Dorsal with Thr* + Met			Ventral with Met*			Ventral with Met* + Thr		
			Bio Rep 1	Bio Rep 2	Bio Rep 3	Bio Rep 1	Bio Rep 2	Bio Rep 3	Bio Rep 1	Bio Rep 2	Bio Rep 3	Bio Rep 1	Bio Rep 2	Bio Rep 3
Spermidine	146.1652	8.89	7.68	7.64	9.26	12.41	8.17	9.34	7.38	7.71	2.73	8.89	8.55	7.89
Putrescine	89.1073	4.50	4.04	3.06	-	-	1.09	1.61	-	-	1.60	5.53	5.92	5.27
Thiamine	265.1118	5.97	-	-	-	-	-	-	8.53	8.50	4.26	22.10	40.31	156.69
SAM	399.1445	19.60	22.83	29.88	-	18.75	11.38	35.60	44.59	54.66	-	14.76	29.46	33.60
Ornithine	133.0972	6.36	5.90	8.27	-	9.34	9.33	-	16.33	21.24	18.65	8.78	8.45	4.99
Lysine	147.1128	7.50	6.36	6.36	6.32	6.19	6.13	7.03	5.92	6.20	6.57	6.44	6.20	6.59
Arginine	175.119	8.20	6.80	6.68	7.17	6.89	7.19	5.80	5.81	5.50	5.06	6.85	6.36	8.22
Homolysine	161.1285	8.57	10.51	-	-	-	-	-	-	-	-	-	-	-
γ-aminobutyrate	104.0706	4.88	2.37	1.76	4.86	4.34	4.05	0.19	-	-	0.37	0.25	-	-
Guanine	152.0567	7.30	4.03	-	6.24	8.58	-	0.41	2.17	2.11	3.01	4.83	4.53	4.57
Carnitine	162.1125	8.20	5.51	3.97	8.25	7.47	-	4.79	2.62	7.26	3.82	6.93	7.28	4.75
Acetylcarnitine	204.123	10.50	7.27	4.48	11.97	13.47	14.39	2.72	6.35	4.08	7.42	3.09	2.96	4.17
Creatine	132.0768	5.60	4.14	4.23	-	-	-	-	3.94	3.80	4.04	-	-	-
Serine	106.0499	3.80	2.26	2.20	-	8.37	6.65	8.33	1.04	0.65	1.46	-	0.30	-
Valine	118.0863	5.98	-	-	-	15.23	-	4.83	-	-	-	3.20	1.18	1.99
Asparagine	133.0608	5.27	5.55	-	9.83	-	-	-	7.04	10.01	10.42	-	-	-
Tryptophan	205.0972	12.85	56.95	-	-	-	-	-	12.48	-	55.63	-	-	-
Methionine	150.0583	6.70			-	-	-	-	16.83	6.62	22.85	-	-	-
Glutamine	147.0764	6.30	5.47	5.62	5.46	5.40	5.37	5.70	6.29	5.69	6.49	5.73	5.18	5.58
Glutamate	148.0604	6.00	4.06	2.32	6.66	5.05	4.64	2.40	4.42	5.06	5.44	3.76	3.69	3.10
Phenylalanine	166.0863	10.30	7.26	-	-				-	-	2.45	5.09	1.72	3.83
Hypoxanthine	137.0458	7.00	5.15	3.31	6.21	7.79	7.97	3.44	-	-	-	4.01	0.64	1.58
Proline	116.0706	5.96	11.73	-	10.24	-	4.92	19.12	7.62	7.99	9.92	4.42	1.63	-
Glutathione, oxidized	307.0833	14.73	21.65	-	-	-	-	-	21.03	-	-	12.74	-	-
Glutathione	308.0911	13.13	11.56	-	12.82	-	-	-	-	-	-	10.90	11.24	13.23
Choline	104.1070	5.97	3.62	-	-	-	-	-	3.52	1.93	1.73	5.59	4.58	4.89
Guanidinopropanoate	132.0768	5.61	-	-	3.94	-	-	-	-	-	-	-	-	-
Ser-Val	205.1183	9.73	-	-	14.14	-	-	-	-	-	-	27.13	-	-
Ser-Arg	262.151	11.94	-	-	-	-	-	-	-	7.42	-	15.99	14.44	9.55
Ala-Lys	218.1499	11.17	-	-	-	-	-	-	-	-	-	6.87	6.35	-
Acetylcholine	146.1176	8.19	-	-	-	-	-	-	-	-	-	4.79	3.44	

Appendix 4.3 KEGG pathway analysis (statistical *p*-value and pathway impact) of dorsal and ventral clones of the *X. laevis* embryo (see plot in Figure 4.3). Key: Thr*, $^{13}C_4$,^{15}N-L-threonine; Met*,$^{13}C_5$,^{15}N-L-methionine.

Dorsal clone with Thr*					
Label	**Name of metabolic pathway**	**Total**	**Hits**	**p**	**Impact**
1	Arginine and proline	43	4	1.69E-04	0.25
2	Glutathione	26	3	7.14E-04	0.05
3	Aminoacyl-tRNA biosynthesis	67	4	9.59E-04	0.10
4	Alanine,aspartate,glutamate	24	2	1.27E-02	0.11
5	Cysteine and methionine	29	2	1.83E-02	0.06
6	Cyanoamino acid	6	1	4.41E-02	0
7	Methane	9	1	6.54E-02	0.40
8	β-Alanine	16	1	1.14E-01	0
9	Sphingolipid	21	1	1.47E-01	0
10	Butanoate	22	1	1.53E-01	0.03
11	Glycine,serine and threonine	31	1	2.09E-01	0.23
12	Tryptophan	39	1	2.57E-01	0.15

Dorsal clones with Thr* and Met					
Label	**Name of metabolic pathway**	**Total**	**Hits**	**p**	**Impact**
1	Aminoacyl-tRNA biosynthesis	67	9	2.03E-08	0.10
2	Valine,leucine,isoleucine	13	4	1.19E-05	1.00
3	Arginine and proline	43	4	1.62E-03	0.24
4	Glutathione	26	3	3.69E-03	0.05
5	Valine,leucine,isoleucine	38	3	1.09E-02	0
6	Alanine,aspartate,glutamate	24	2	3.55E-02	0.15
7	Cysteine and methionine	29	2	5.04E-02	0.06
8	Glycine,serine and threonine	31	2	5.69E-02	0.26
9	D-Glutamine and D-glutamate	5	1	6.20E-02	0
10	Cyanoamino acid	6	1	7.39E-02	0
11	Nitrogen	9	1	1.09E-01	0
12	Methane	9	1	1.09E-01	0.4

Ventral clone with Met*					
Label	**Name of metabolic pathway**	**Total**	**Hits**	**p**	**Impact**
1	Aminoacyl-tRNA biosynthesis	67	8	1.26E-07	0.10
2	Arginine and proline	43	6	3.10E-06	0.33
3	Alanine, aspartate, glutamate	24	3	2.00E-03	0.31
4	Cysteine and methionine	29	3	3.49E-03	0.17
5	Glycine, serine and threonine	31	3	4.24E-03	0.26
6	β-Alanine	16	2	1.28E-02	0
7	Glutathione	26	2	3.26E-02	0.01
8	Cyanoamino acid	6	1	6.55E-02	0
9	Methane	9	1	9.67E-02	0.40
10	Valine,leucine,isoleucine	13	1	1.37E-01	0
11	Histidine	14	1	1.47E-01	0
12	Nicotinate and nicotinamide	14	1	1.47E-01	0

Ventral clone with Met* and Thr					
Label	**Name of metabolic pathway**	**Total**	**Hits**	**p**	**Impact**
1	Glutathione	26	4	3.37E-05	0.06
2	Arginine and proline	43	4	2.59E-04	0.30
3	Aminoacyl-tRNA biosynthesis	67	3	1.48E-02	0
4	Alanine,aspartate, glutamate	24	2	1.54E-02	0.02
5	Cysteine and methionine	29	2	2.21E-02	0.17
6	Thiamine metabolism	7	1	5.62E-02	0.40
7	β-Alanine	16	1	1.24E-01	0
8	Tryptophan	39	1	2.78E-01	0.15

Appendix 5.1 Metabolites identified in D11, D12, V11, and V12 cells of the *X. laevis* 16-cell embryo.

Metabolite	Formula	Time (min)	*m/z* measured	*m/z* theoretical	Δ *m/z* (mDa)	Δ *m/z* (ppm)
Spermidine (SPM)[**]	$C_7H_{19}N_3$	10.34	146.1654	146.1652	–0.2	–1.4
Putrescine[‡]	$C_4H_{12}N_2$	10.92	89.1073	89.1073	0.0	0.0
Methylhistamine[**]	$C_6H_{11}N_3$	11.43	126.1019	126.1026	0.7	5.6
Thiamine[**]	$C_{12}H_{16}N_4OS$	12.02	265.1117	265.1118	0.1	0.2
Choline (Cho)[*,**]	$C_5H_{13}NO$	16.51	104.1065	104.1070	0.5	4.8
Ala-Lys (AK)[**]	$C_9H_{19}N_3O_3$	16.74	218.1492	218.1491	–0.1	–0.5
Arg-Ala (RA) [**]	$C_9H_{19}N_5O_3$	17.08	246.1557	246.1561	0.4	1.5
Lys-Ser (KS)[**]	$C_9H_{19}N_3O_4$	17.15	234.1449	234.1448	–0.1	–0.3
Val-Lys (VK) [**]	$C_{11}H_{23}N_3O_3$	17.49	246.1820	246.1812	–0.8	–3.2
S-adenosyl-methionine (SAM)[**]	$C_{15}H_{22}N_6O_5S$	17.44	399.1461	399.1445	–1.6	–4.0
Ser-Arg (SR)[**]	$C_9H_{19}N_5O_4$	17.49	262.1516	262.1510	–0.6	–2.3
Ornithine (Orn) [**]	$C_5H_{12}N_2O_2$	17.7	133.0969	133.0972	0.3	2.3
Sarcosine[‡]	C3H7NO2	17.87	90.0557	90.0550	–0.7	–7.8
Lysine (Lys)[*,**]	$C_6H_{14}N_2O_2$	17.88	147.1131	147.1128	–0.3	–2.0
Arginine (Arg) [*,**]	$C_6H_{14}N_4O_2$	18.45	175.1193	175.1190	–0.3	–2.0
Homolysine[**]	$C_7H_{16}N_2O_2$	18.47	161.1295	161.1285	–1.0	–6.5
Tyr-Lys (YK)[**]	$C_{15}H_{23}N_3O_4$	18.55	310.1757	310.1761	0.4	1.4
γ-aminobutyric acid (GABA)	$C_4H_9NO_2$	18.67	104.0701	104.0706	0.5	4.9
N6,N6,N6-trimethyl-lysine (TML) [**]	$C_9H_{20}N_2O_2$	18.71	189.1599	189.1598	–0.1	–0.8
Histidine (His)[*,**]	$C_6H_9N_3O_2$	18.74	156.0775	156.0768	–0.7	–4.8
Methylhistidine[**]	$C_7H_{11}N_3O_2$	19.23	170.0945	170.0924	–2.1	–12.3
Guanidinopropanoate[**]	$C_4H_9N_3O_2$	19.47	132.0766	132.0768	0.2	1.2
Acetylcholine (AcCho)[*,**]	$C_7H_{15}NO_2$	19.7	146.1176	146.1176	0.0	–0.3
Trolamine (TEA)[‡]	$C_6H_{15}NO_3$	20.01	150.1123	150.1125	0.2	1.3
Leu-Ala (LA)[**]	$C_9H_{18}N_2O_3$	20.1	203.1381	203.1390	0.9	4.5
Cis-urocanate (cURA)[**]	$C_6H_6N_2O_2$	20.22	139.0495	139.0502	0.7	5.0
Guanine[**]	$C_5H_5N_5O$	20.37	152.0568	152.0567	–0.1	–0.7

Metabolite	Formula	Time (min)	*m/z* measured	*m/z* theoretical	Δ *m/z* (mDa)	Δ *m/z* (ppm)
Carnitine (Car) [*,**]	$C_7H_{15}NO_3$	20.85	162.1133	162.1125	–0.8	–5.1
Trans-Urocanate[**]	$C_6H_6N_2O_2$	20.99	139.0495	139.0502	0.7	5.0
Methylguanine[**]	$C_6H_7N_5O$	21.28	166.0722	166.0723	0.1	0.6
Pyridoxal[**]	$C_8H_9NO_3$	21.43	168.0662	168.0655	–0.7	–4.0
Cytosine[**]	$C_4H_5N_3O$	21.76	112.0496	112.0505	0.9	8.0
Acetylcarnitine (AcCar)[**]	$C_9H_{17}NO_4$	22.44	204.1228	204.1230	0.2	1.1
Propionylcarnitine[**]	$C_{10}H_{19}NO_4$	23.13	218.1386	218.1387	0.1	0.5
Methylaspartate[**]	$C_5H_9NO_4$	23.2	148.0607	148.0604	–0.3	–1.8
Glycine (Gly)[*]	$C_2H_5NO_2$	23.50	76.0386	76.0393	0.7	9.3
Niacinamide[*]	$C_6H_6N_2O$	23.31	123.0547	123.0553	0.6	4.8
Creatine (CR)[*,**]	$C_4H_9N_3O_2$	23.53	132.0765	132.0768	0.3	1.9
Pro-Val (PV)[**]	$C_{10}H_{18}N_2O_3$	24.03	215.1386	215.1390	0.4	1.9
Adenosine[**]	$C_{10}H_{13}N_5O_4$	24.32	268.1049	268.1040	–0.9	–3.4
Alanine (Ala)[*]	$C_3H_7NO_2$	23.53	90.0550	90.0550	0.0	–0.5
Argininosuccinate (ASA)[**]	$C_{10}H_{18}N_4O_6$	26.43	291.1310	291.1299	–1.1	–3.7
Valine (Val)[*,**]	$C_5H_{11}NO_2$	28.54	118.0860	118.0863	0.3	2.2
Serine (Ser)[*,**]	$C_3H_7NO_3$	28.59	106.0494	106.0499	0.5	4.4
Isoleucine (Ile) [*,‡]	$C_6H_{13}NO_2$	28.84	132.1015	132.1019	0.4	3.1
Leucine (Leu) [*,‡]	$C_6H_{13}NO_2$	29.1	132.1015	132.1019	0.4	3.1
Asparagine (Asn)[**]	$C_4H_8N_2O_3$	30.17	133.0607	133.0608	0.1	0.5
Threonine (Thr)[*,**]	$C_4H_9NO_3$	30.2	120.0651	120.0655	0.4	3.5
Tryptophan (Trp)[*,**]	$C_{11}H_{12}N_2O_2$	30.76	205.0965	205.0972	0.7	3.2
Methionine (Met)[*,**]	$C_5H_{11}NO_2S$	30.89	150.0586	150.0583	–0.3	–1.8
Glutamine (Gln)[*,**]	$C_5H_{10}N_2O_3$	30.96	147.0766	147.0764	–0.2	–1.2
2-Aminoadipic acid[**]	$C_6H_{11}NO_4$	31.08	162.0768	162.0761	–0.7	–4.4
Methylene glutamine[**]	$C_6H_{10}N_2O_3$	31.20	159.0769	159.0764	–0.5	–3.1
Citrulline (Cit)[**]	$C_6H_{13}N_3O_3$	31.39	176.1030	176.1030	0.0	–0.2
Homocitrulline[**]	$C_7H_{15}N_3O_3$	31.46	190.1171	190.1186	1.5	8.0
Glutamic acid (Glu)[*,**]	$C_5H_9NO_4$	31.43	148.0605	148.0604	–0.1	–0.4
Phenylalanine(Phe)[*,**]	$C_9H_{11}NO_2$	32.01	166.0868	166.0863	–0.5	–3.3

Metabolite	Formula	Time (min)	*m/z* measured	*m/z* theoretical	Δ *m/z* (mDa)	Δ *m/z* (ppm)
Acetyllysine‡	$C_8H_{16}N_2O_3$	32.33	189.1232	189.1234	0.2	0.9
Tyrosine (Tyr)*,**	$C_9H_{11}NO_3$	32.41	182.0809	182.0812	0.3	1.5
Hypoxanthine (HPX)*,**	$C_5H_4N_4O$	32.46	137.0458	137.0458	0.0	–0.1
Proline (Pro)*,**	$C_5H_9NO_2$	32.98	116.0702	116.0706	0.4	3.5
Ser-Val (SV)†	$C_8H_{16}N_2O_4$	33.38	205.1180	205.1183	0.3	1.4
Cysteine (Cys)*,**	$C_3H_7NO_2S$	33.5	122.0260	122.0270	1.0	8.4
Aspartic acid (Asp)*,**	$C_4H_7NO_4$	34.6	134.0446	134.0448	0.2	1.4
Glycine betaine (GB)*,‡	$C_5H_{11}NO_2$	35.23	118.0857	118.0863	0.6	4.7
Glutathione, oxidized (GSSG)**	$C_{20}H_{32}N_6O_{12}S_2$	35.92	307.0848	307.0833	–1.5	–5.0
Hydroxyproline (Hyp)**	$C_5H_9NO_3$	37.2	132.0648	132.0655	0.7	5.5
Glutathione (GSH)*,**	$C_{10}H_{17}N_3O_6S$	38.96	308.0924	308.0911	–1.3	–4.3

Note: Asterisk (*) signifies identification based on migration-time comparison to chemical standards. Double asterisk (**) denotes identification by tandem mass spectrometry experiments on related standards or comparison to data available in Metlin (hppt://metlin.scripps.edu), MzCloud (hppt://mzcloud.org), or HMDB (hppt://hmdb.ca). Dagger (†) indicates that tandem mass spectrum agrees with molecular fragmentation predicted in Mass Frontier 7.0 (Thermo Fisher). Double dagger (‡) indicates mass-match in Metlin.

Appendix 5.2 Results from GProX[174] cluster analysis of average metabolite ratios between dorsal and ventral cells in the 16-cell *X. laevis* embryo. Unidentified molecular features are listed as accurate mass (*m/z*) values.

Mol. Feature	Cluster	D12/D11	V12/D11	V11/D11
351.099	0	1.20	1.09	1.06
Putrescine	0	0.87	0.86	0.90
Choline	0	0.97	0.92	1.06
SAM	0	0.89	0.82	0.93
120.1022	0	0.99	1.47	1.22
Guanine	0	0.96	0.91	1.26
135.0287	0	0.94	0.80	1.30
Carnitine	0	0.86	0.83	0.78
150.0582	0	0.86	1.17	0.91
166.107	0	0.92	1.20	1.15
194.1533	0	0.88	0.80	1.28
188.0705	0	0.92	0.92	1.14
Phenylalanine	0	0.86	0.76	0.96
Hypoxanthine	0	1.03	0.96	1.15
255.0969	1	4.80	1.27	4.78
138.1022	1	0.92	0.72	1.01
152.118	1	0.94	0.56	0.75
180.1492	1	0.84	0.69	0.91
214.1332	1	1.12	0.59	0.95
116.0705	1	0.85	0.50	0.76
Ornithine	1	0.89	0.55	0.76
Lysine	1	0.77	0.52	0.73
Arginine	1	0.84	0.64	0.77
Histidine	1	0.88	0.60	0.96
232.9989	1	0.46	0.12	0.69
192.1378	1	0.60	0.12	0.81
278.1258	1	1.28	0.63	1.23
Valine	1	0.84	0.61	0.81
Isoleucine	1	0.98	0.52	0.83
Leucine	1	0.84	0.67	0.86
Threonine	1	0.87	0.55	0.78
159.0767	1	0.73	0.53	0.76
176.1032	1	0.86	0.63	0.95
Glutamate	1	0.91	0.64	0.82
237.9678	1	0.89	0.72	0.90

Mol. Feature	Cluster	D12/D11	V12/D11	V11/D11
Aspartate	1	0.91	0.66	0.88
Hydroxyproline	1	0.86	0.67	0.83
Glutathione	1	0.98	0.71	0.99
290.8472	2	0.96	0.71	0.43
GABA	2	134.35	0.56	0.60
TML	2	0.76	0.64	0.73
124.1118	2	0.90	0.37	0.14
Acetylcholine	2	0.83	0.77	0.73
144.1377	2	0.14	0.11	0.17
Methyl guanine	2	1.84	0.71	0.90
204.1233	2	0.84	0.66	0.75
144.1019	2	0.18	0.00	0.08
112.0499	2	1.06	0.78	0.59
198.1846	2	0.78	0.56	0.56
240.1226	2	0.73	0.18	0.32
Creatine	2	0.68	0.75	0.66
Methionine	2	0.85	0.71	0.66
Aspartate	2	0.93	0.53	0.68
Glutamate	2	0.82	0.54	0.68
Proline	2	0.62	0.26	0.26
Glycine betaine	2	0.81	0.61	0.62
102.9699	3	1.60	2.56	3.09
146.996	3	1.04	1.73	1.50
197.0326	3	2.35	2.73	2.14
218.9831	3	1.13	14.59	1.31
232.9989	3	0.89	12.57	1.03
119.0189	3	1.09	1.64	1.30
133.0315	3	1.19	1.70	1.44
101.0082	3	1.08	1.79	1.33
218.9831	3	2.33	3.73	1.41
135.0287	3	1.41	4.37	2.08
182.9801	3	1.23	2.15	1.68
246.1555	3	0.52	1.40	1.17
Ser-Arg	3	0.50	1.41	1.06
100.1119	3	2.58	3.00	1.61
130.1583	3	1.31	2.19	2.30
202.18	3	0.53	1.79	0.84
246.242	3	1.71	2.41	1.97
274.242	3	1.94	1.59	2.03

Mol. Feature	Cluster	D12/D11	V12/D11	V11/D11
338.1818	4	0.65	0.69	0.82
142.1226	4	0.73	0.66	0.92
150.1125	4	1.76	1.65	6.87
254.0191	4	0.51	0.78	1.54
210.1488	4	0.55	0.73	0.80
255.0969	4	0.76	0.66	0.98
134.0807	4	0.57	0.69	0.82
212.201	4	0.61	0.80	0.82
Serine	4	0.92	0.69	1.14
Tyrosine	4	0.73	0.76	1.07

Bibliography

1. Dunham, I.; Kundaje, A.; Aldred, S.; Collins, P.; Davis, C.; Doyle, F.; Consortium, E., An integrated encyclopedia of DNA elements in the human genome. *Nature* **2012,** *489* (7414), 57-74.
2. Kim, M. S.; Pinto, S. M.; Getnet, D.; Nirujogi, R. S.; Manda, S. S.; Chaerkady, R.; Madugundu, A. K.; Kelkar, D. S.; Isserlin, R.; Jain, S.; Thomas, J. K.; Muthusamy, B.; Leal-Rojas, P.; Kumar, P.; Sahasrabuddhe, N. A.; Balakrishnan, L.; Advani, J.; George, B.; Renuse, S.; Selvan, L. D.; Patil, A. H.; Nanjappa, V.; Radhakrishnan, A.; Prasad, S.; Subbannayya, T.; Raju, R.; Kumar, M.; Sreenivasamurthy, S. K.; Marimuthu, A.; Sathe, G. J.; Chavan, S.; Datta, K. K.; Subbannayya, Y.; Sahu, A.; Yelamanchi, S. D.; Jayaram, S.; Rajagopalan, P.; Sharma, J.; Murthy, K. R.; Syed, N.; Goel, R.; Khan, A. A.; Ahmad, S.; Dey, G.; Mudgal, K.; Chatterjee, A.; Huang, T. C.; Zhong, J.; Wu, X.; Shaw, P. G.; Freed, D.; Zahari, M. S.; Mukherjee, K. K.; Shankar, S.; Mahadevan, A.; Lam, H.; Mitchell, C. J.; Shankar, S. K.; Satishchandra, P.; Schroeder, J. T.; Sirdeshmukh, R.; Maitra, A.; Leach, S. D.; Drake, C. G.; Halushka, M. K.; Prasad, T. S.; Hruban, R. H.; Kerr, C. L.; Bader, G. D.; Iacobuzio-Donahue, C. A.; Gowda, H.; Pandey, A., A draft map of the human proteome. *Nature* **2014,** *509* (7502), 575-81.
3. Wishart, D. S.; Feunang, Y. D.; Marcu, A.; Guo, A. C.; Liang, K.; Vazquez-Fresno, R.; Sajed, T.; Johnson, D.; Li, C.; Karu, N.; Sayeeda, Z.; Lo, E.; Assempour, N.; Berjanskii, M.; Singhal, S.; Arndt, D.; Liang, Y.; Badran, H.; Grant, J.; Serra-Cayuela, A.; Liu, Y.; Mandal, R.; Neveu, V.; Pon, A.; Knox, C.; Wilson, M.; Manach, C.; Scalbert, A., HMDB 4.0: the human metabolome database for 2018. *Nucleic acids research* **2018,** *46* (D1), D608-d617.
4. Eberwine, J.; Sul, J.-Y.; Bartfai, T.; Kim, J., The promise of single-cell sequencing. *Nature methods* **2014,** *11* (1), 25-27.
5. Blainey, P. C.; Quake, S. R., Dissecting genomic diversity, one cell at a time. *Nature methods* **2014,** *11* (1), 19-21.
6. Yuan, G.-C.; Cai, L.; Elowitz, M.; Enver, T.; Fan, G.; Guo, G.; Irizarry, R.; Kharchenko, P.; Kim, J.; Orkin, S.; Quackenbush, J.; Saadatpour, A.; Schroeder, T.; Shivdasani, R.; Tirosh, I., Challenges and emerging directions in single-cell analysis. *Genome Biology* **2017,** *18* (1), 84.
7. Klein, Allon M.; Mazutis, L.; Akartuna, I.; Tallapragada, N.; Veres, A.; Li, V.; Peshkin, L.; Weitz, David A.; Kirschner, Marc W., Droplet barcoding for single-cell transcriptomics applied to embryonic stem cells. *Cell* **2015,** *161* (5), 1187-1201.
8. Briggs, J. A.; Weinreb, C.; Wagner, D. E.; Megason, S.; Peshkin, L.; Kirschner, M. W.; Klein, A. M., The dynamics of gene expression in vertebrate embryogenesis at single-cell resolution. *Science* **2018,** *360* (6392), eaar5780.
9. Lombard-Banek, C.; Moody, S. A.; Nemes, P., Single-cell mass spectrometry for discovery proteomics: Quantifying translational cell heterogeneity in the 16-cell frog (*Xenopus*) embryo. *Angewandte Chemie (International ed. in English)* **2016,** *55* (7), 2454-8.

10. Saha-Shah, A.; Esmaeili, M.; Sidoli, S.; Hwang, H.; Yang, J.; Klein, P. S.; Garcia, B. A., Single cell proteomics by data-independent acquisition to study embryonic asymmetry in *Xenopus laevis*. *Analytical Chemistry* **2019,** *91* (14), 8891-8899.
11. Harwood, M. M.; Christians, E. S.; Fazal, M. A.; Dovichi, N. J., Single-cell protein analysis of a single mouse embryo by two-dimensional capillary electrophoresis. *Journal of Chromatography A* **2006,** *1130* (2), 190-194.
12. Onjiko, R. M.; Moody, S. A.; Nemes, P., Single-cell mass spectrometry reveals small molecules that affect cell fates in the 16-cell embryo. *Proceedings of the National Academy of Sciences of the United States of America* **2015,** *112* (21), 6545-50.
13. Vastag, L.; Jorgensen, P.; Peshkin, L.; Wei, R.; Rabinowitz, J. D.; Kirschner, M. W., Remodeling of the metabolome during early frog fevelopment. *PLOS ONE* **2011,** *6* (2), e16881.
14. Nemes, P.; Knolhoff, A. M.; Rubakhin, S. S.; Sweedler, J. V., Metabolic differentiation of neuronal phenotypes by single-cell capillary electrophoresis-electrospray ionization-mass spectrometry. *Analytical Chemistry* **2011,** *83* (17), 6810-7.
15. Dey, S. S.; Kester, L.; Spanjaard, B.; Bienko, M.; van Oudenaarden, A., Integrated genome and transcriptome sequencing of the same cell. *Nature biotechnology* **2015,** *33* (3), 285-289.
16. Macosko, E. Z.; Basu, A.; Satija, R.; Nemesh, J.; Shekhar, K.; Goldman, M.; Tirosh, I.; Bialas, A. R.; Kamitaki, N.; Martersteck, E. M.; Trombetta, J. J.; Weitz, D. A.; Sanes, J. R.; Shalek, A. K.; Regev, A.; McCarroll, S. A., Highly parallel genome-wide expression profiling of individual cells using nanoliter droplets. *Cell* **2015,** *161* (5), 1202-1214.
17. Shapiro, E.; Biezuner, T.; Linnarsson, S., Single-cell sequencing-based technologies will revolutionize whole-organism science. *Nature Reviews Genetics* **2013,** *14* (9), 618-630.
18. Liu, Y.; Chen, X.; Zhang, Y.; Liu, J., Advancing single-cell proteomics and metabolomics with microfluidic technologies. *Analyst* **2019,** *144* (3), 846-858.
19. Lombard-Banek, C.; Moody, S. A.; Manzini, M. C.; Nemes, P., Microsampling capillary electrophoresis mass spectrometry enables single-cell proteomics in complex tissues: developing cell clones in live *Xenopus laevis* and zebrafish embryos. *Analytical Chemistry* **2019,** *91* (7), 4797-4805.
20. Budnik, B.; Levy, E.; Harmange, G.; Slavov, N., SCoPE-MS: mass spectrometry of single mammalian cells quantifies proteome heterogeneity during cell differentiation. *Genome Biology* **2018,** *19* (1), 161.
21. Thompson, A.; Schäfer, J.; Kuhn, K.; Kienle, S.; Schwarz, J.; Schmidt, G.; Neumann, T.; Hamon, C., Tandem mass tags: A novel quantification strategy for comparative analysis of complex protein mixtures by MS/MS. *Analytical Chemistry* **2003,** *75* (8), 1895-1904.
22. Sun, L.; Dubiak, K. M.; Peuchen, E. H.; Zhang, Z.; Zhu, G.; Huber, P. W.; Dovichi, N. J., Single cell proteomics using frog (*Xenopus laevis*) blastomeres isolated from early stage embryos, which form a geometric progression in protein content. *Analytical Chemistry* **2016,** *88* (13), 6653-6657.

23. Wühr, M.; Freeman, R. M., Jr.; Presler, M.; Horb, M. E.; Peshkin, L.; Gygi, S.; Kirschner, M. W., Deep proteomics of the *Xenopus laevis* egg using an mRNA-derived reference database. *Curr Biol* **2014,** *24* (13), 1467-1475.
24. Virant-Klun, I.; Leicht, S.; Hughes, C.; Krijgsveld, J., Identification of maturation-specific proteins by single-cell proteomics of human oocytes. *Mol Cell Proteomics* **2016,** *15* (8), 2616-27.
25. Zhu, H.; Zou, G.; Wang, N.; Zhuang, M.; Xiong, W.; Huang, G., Single-neuron identification of chemical constituents, physiological changes, and metabolism using mass spectrometry. *Proceedings of the National Academy of Sciences* **2017,** *114* (10), 2586-2591.
26. Sarver, S. A.; Schiavone, N. M.; Arceo, J.; Peuchen, E. H.; Zhang, Z.; Sun, L.; Dovichi, N. J., Capillary electrophoresis coupled to negative mode electrospray ionization-mass spectrometry using an electrokinetically-pumped nanospray interface with primary amines grafted to the interior of a glass emitter. *Talanta* **2017,** *165*, 522-525.
27. Wang, M.; Dubiak, K.; Zhang, Z.; Huber, P. W.; Chen, D. D. Y.; Dovichi, N. J., MALDI-imaging of early stage *Xenopus laevis* embryos. *Talanta* **2019,** *204*, 138-144.
28. Liu, R.; Pan, N.; Zhu, Y.; Yang, Z., T-Probe: An integrated microscale device for online in situ single cell analysis and metabolic profiling using mass spectrometry. *Anal Chem* **2018,** *90* (18), 11078-11085.
29. Zhang, L.; Foreman, D. P.; Grant, P. A.; Shrestha, B.; Moody, S. A.; Villiers, F.; Kwak, J. M.; Vertes, A., In situ metabolic analysis of single plant cells by capillary microsampling and electrospray ionization mass spectrometry with ion mobility separation. *Analyst* **2014,** *139* (20), 5079-5085.
30. Portero, E. P.; Nemes, P., Dual cationic–anionic profiling of metabolites in a single identified cell in a live *Xenopus laevis* embryo by microprobe CE-ESI-MS. *Analyst* **2019,** *144* (3), 892-900.
31. Comi, T. J.; Makurath, M. A.; Philip, M. C.; Rubakhin, S. S.; Sweedler, J. V., MALDI-MS guided liquid microjunction extraction for capillary electrophoresis-electrospray ionization MS analysis of single pancreatic islet cells. *Analytical Chemistry* **2017,** *89* (14), 7765-7772.
32. Li, J.; Shi, Y.; Sun, J.; Zhang, Y.; Mao, B., *Xenopu*s reduced folate carrier regulates neural crest development epigenetically. *PLOS ONE* **2011,** *6* (11), e27198.
33. Tsuchiya, Y.; Pham, U.; Hu, W.; Ohnuma, S.-I.; Gout, I., Changes in acetyl CoA levels during the early embryonic development of *Xenopus laevis*. *PloS one* **2014,** *9* (5), e97693-e97693.
34. Griffiths, W. J.; Koal, T.; Wang, Y.; Kohl, M.; Enot, D. P.; Deigner, H.-P., Targeted metabolomics for biomarker discovery. *Angewandte Chemie International Edition* **2010,** *49* (32), 5426-5445.
35. Fiehn, O.; Kopka, J.; Dörmann, P.; Altmann, T.; Trethewey, R. N.; Willmitzer, L., Metabolite profiling for plant functional genomics. *Nature biotechnology* **2000,** *18* (11), 1157-1161.

36. Tolstikov, V. V.; Lommen, A.; Nakanishi, K.; Tanaka, N.; Fiehn, O., Monolithic silica-based capillary reversed-phase liquid chromatography/electrospray mass spectrometry for plant metabolomics. *Analytical Chemistry* **2003,** *75* (23), 6737-6740.
37. Plumb, R. S.; Rainville, P.; Smith, B. W.; Johnson, K. A.; Castro-Perez, J.; Wilson, I. D.; Nicholson, J. K., Generation of ultrahigh peak capacity LC separations via elevated temperatures and high linear mobile-phase velocities. *Analytical Chemistry* **2006,** *78* (20), 7278-7283.
38. Hu, C.; van Dommelen, J.; van der Heijden, R.; Spijksma, G.; Reijmers, T. H.; Wang, M.; Slee, E.; Lu, X.; Xu, G.; van der Greef, J.; Hankemeier, T., RPLC-ion-trap-FTMS method for lipid profiling of plasma: method validation and application to p53 mutant mouse model. *Journal of proteome research* **2008,** *7* (11), 4982-91.
39. Fei, F.; Bowdish, D. M. E.; McCarry, B. E., Comprehensive and simultaneous coverage of lipid and polar metabolites for endogenous cellular metabolomics using HILIC-TOF-MS. *Analytical and Bioanalytical Chemistry* **2014,** *406* (15), 3723-3733.
40. Tang, D.-Q.; Zou, L.; Yin, X.-X.; Ong, C. N., HILIC-MS for metabolomics: An attractive and complementary approach to RPLC-MS. *Mass Spectrometry Reviews* **2016,** *35* (5), 574-600.
41. Onjiko, R. M.; Portero, E. P.; Nemes, P., CHAPTER 10 Single-cell metabolomics with capillary electrophoresis–mass spectrometry. In *Capillary Electrophoresis–Mass Spectrometry for Metabolomics*, The Royal Society of Chemistry: 2018; pp 209-224.
42. Sumner, L. W.; Amberg, A.; Barrett, D.; Beale, M. H.; Beger, R.; Daykin, C. A.; Fan, T. W. M.; Fiehn, O.; Goodacre, R.; Griffin, J. L.; Hankemeier, T.; Hardy, N.; Harnly, J.; Higashi, R.; Kopka, J.; Lane, A. N.; Lindon, J. C.; Marriott, P.; Nicholls, A. W.; Reily, M. D.; Thaden, J. J.; Viant, M. R., Proposed minimum reporting standards for chemical analysis chemical analysis working group (CAWG) metabolomics standards initiative (MSI). *Metabolomics : Official journal of the Metabolomic Society* **2007,** *3* (3), 211-221.
43. Guijas, C.; Montenegro-Burke, J. R.; Domingo-Almenara, X.; Palermo, A.; Warth, B.; Hermann, G.; Koellensperger, G.; Huan, T.; Uritboonthai, W.; Aisporna, A. E.; Wolan, D. W.; Spilker, M. E.; Benton, H. P.; Siuzdak, G., METLIN: A technology platform for identifying knowns and unknowns. *Analytical Chemistry* **2018,** *90* (5), 3156-3164.
44. Weston, D. J., Ambient ionization mass spectrometry: current understanding of mechanistic theory; analytical performance and application areas. *Analyst* **2010,** *135* (4), 661-668.
45. Alberici, R. M.; Simas, R. C.; Sanvido, G. B.; Romão, W.; Lalli, P. M.; Benassi, M.; Cunha, I. B. S.; Eberlin, M. N., Ambient mass spectrometry: bringing MS into the "real world". *Analytical and Bioanalytical Chemistry* **2010,** *398* (1), 265-294.

46. Ferreira, C. R.; Pirro, V.; Eberlin, L. S.; Hallett, J. E.; Cooks, R. G., Developmental phases of individual mouse preimplantation embryos characterized by lipid signatures using desorption electrospray ionization mass spectrometry. *Analytical and Bioanalytical Chemistry* **2012,** *404* (10), 2915-2926.
47. González-Serrano, A. F.; Pirro, V.; Ferreira, C. R.; Oliveri, P.; Eberlin, L. S.; Heinzmann, J.; Lucas-Hahn, A.; Niemann, H.; Cooks, R. G., Desorption electrospray ionization mass spectrometry reveals lipid metabolism of individual oocytes and embryos. *PLOS ONE* **2013,** *8* (9), e74981.
48. Kim, J.; Kim, J. S.; Jeon, Y. J.; Kim, D. W.; Yang, T. H.; Soh, Y.; Lee, H. K.; Choi, N. J.; Park, S. B.; Seo, K. S.; Chung, H. M.; Lee, D. S.; Chae, J. I., Identification of maturation and protein synthesis related proteins from porcine oocytes during in vitro maturation. *Proteome science* **2011,** *9*, 28.
49. Pirro, V.; Guffey, S. C.; Sepulveda, M. S.; Mahapatra, C. T.; Ferreira, C. R.; Jarmusch, A. K.; Cooks, R. G., Lipid dynamics in zebrafish embryonic development observed by DESI-MS imaging and nanoelectrospray-MS. *Molecular bioSystems* **2016,** *12* (7), 2069-79.
50. Shrestha, B.; Sripadi, P.; Reschke, B. R.; Henderson, H. D.; Powell, M. J.; Moody, S. A.; Vertes, A., Subcellular Metabolite and Lipid Analysis of Xenopus laevis Eggs by LAESI Mass Spectrometry. *PLOS ONE* **2014,** *9* (12), e115173.
51. Northen, T. R.; Yanes, O.; Northen, M. T.; Marrinucci, D.; Uritboonthai, W.; Apon, J.; Golledge, S. L.; Nordström, A.; Siuzdak, G., Clathrate nanostructures for mass spectrometry. *Nature* **2007,** *449* (7165), 1033-6.
52. Tian, H.; Fletcher, J. S.; Thuret, R.; Henderson, A.; Papalopulu, N.; Vickerman, J. C.; Lockyer, N. P., Spatiotemporal lipid profiling during early embryo development of *Xenopus laevis* using dynamic ToF-SIMS imaging. *J Lipid Res* **2014,** *55* (9), 1970-1980.
53. Lombard-Banek, C.; Portero, E. P.; Onjiko, R. M.; Nemes, P., New-generation mass spectrometry expands the toolbox of cell and developmental biology. *Genesis (New York, N.Y. : 2000)* **2017,** *55* (1-2).
54. Hench, J.; Bratić Hench, I.; Pujol, C.; Ipsen, S.; Brodesser, S.; Mourier, A.; Tolnay, M.; Frank, S.; Trifunović, A., A tissue-specific approach to the analysis of metabolic changes in *Caenorhabditis elegans*. *PLOS ONE* **2011,** *6* (12), e28417.
55. Onjiko, R. M.; Portero, E. P.; Moody, S. A.; Nemes, P., In situ microprobe single-cell capillary electrophoresis mass spectrometry: Metabolic reorganization in single differentiating cells in the live vertebrate (*Xenopus laevis*) embryo. *Analytical Chemistry* **2017,** *89* (13), 7069-7076.
56. Aerts, J. T.; Louis, K. R.; Crandall, S. R.; Govindaiah, G.; Cox, C. L.; Sweedler, J. V., Patch clamp electrophysiology and capillary electrophoresis–mass spectrometry metabolomics for single cell characterization. *Analytical Chemistry* **2014,** *86* (6), 3203-3208.
57. Onjiko, R. M.; Morris, S. E.; Moody, S. A.; Nemes, P., Single-cell mass spectrometry with multi-solvent extraction identifies metabolic differences between left and right blastomeres in the 8-cell frog (*Xenopus*) embryo. *Analyst* **2016,** *141* (12), 3648-56.

58. Moody, S. A., Fates of the blastomeres of the 16-cell stage *Xenopus* embryo. *Dev Biol* **1987,** *119* (2), 560-78.
59. Moody, S. A., Fates of the blastomeres of the 32-cell-stage *Xenopus* embryo. *Dev Biol* **1987,** *122* (2), 300-19.
60. Marina, M. L.; Ríos, A.; Valcárcel, M., *Analysis and detection by capillary electrophoresis*. 1 st ed.; Elsevier Science: 2005; Vol. 45.
61. Altria, K.D., Fundamentals of capillary electrophoresis theory. In *Capillary electrophoresis guidebook*, Humana Press: Totowa NJ, 1996; Vol. 52.
62. Harris, D. C., *Quantitative chemical analysis*. Eighth ed.; W. H. Freeman: 2010.
63. Van Deemter, J. J.; Zuiderweg, F. J.; Klinkenberg, A., Longitudinal diffusion and resistance to mass transfer as causes of nonideality in chromatography. *Chemical Engineering Science* **1995,** *50* (24), 3869-3882.
64. Zenobi, R., Single-cell metabolomics: analytical and biological perspectives. *Science* **2013,** *342* (6163), 1243259.
65. Lapainis, T.; Rubakhin, S. S.; Sweedler, J. V., Capillary electrophoresis with electrospray ionization mass spectrometric detection for single-cell metabolomics. *Analytical chemistry* **2009,** *81* (14), 5858-5864.
66. Fessenden, M., Metabolomics: small molecules, single cells. *Nature* **2016,** *540* (7631), 153-155.
67. Cohen, D.; Dickerson, J. A.; Whitmore, C. D.; Turner, E. H.; Palcic, M. M.; Hindsgaul, O.; Dovichi, N. J., Chemical cytometry: fluorescence-based single-cell analysis. *Annual review of analytical chemistry (Palo Alto, Calif.)* **2008,** *1*, 165-90.
68. Svatoš, A., Single-cell metabolomics comes of age: new developments in mass spectrometry profiling and imaging. *Analytical Chemistry* **2011,** *83* (13), 5037-5044.
69. Heinemann, M.; Zenobi, R., Single cell metabolomics. *Current opinion in biotechnology* **2011,** *22* (1), 26-31.
70. Comi, T. J.; Do, T. D.; Rubakhin, S. S.; Sweedler, J. V., Categorizing cells on the basis of their chemical profiles: progress in single-cell mass spectrometry. *Journal of the American Chemical Society* **2017,** *139* (11), 3920-3929.
71. Rubakhin, S. S.; Lanni, E. J.; Sweedler, J. V., Progress toward single cell metabolomics. *Current opinion in biotechnology* **2013,** *24* (1), 95-104.
72. Ong, T.-H.; Tillmaand, E. G.; Makurath, M.; Rubakhin, S. S.; Sweedler, J. V., Mass spectrometry-based characterization of endogenous peptides and metabolites in small volume samples. *Biochim Biophys Acta* **2015,** *1854* (7), 732-740.
73. Spiller, D. G.; Wood, C. D.; Rand, D. A.; White, M. R., Measurement of single-cell dynamics. *Nature* **2010,** *465* (7299), 736-45.
74. Onjiko, R. M.; Plotnick, D. O.; Moody, S. A.; Nemes, P., Metabolic comparison of dorsal versus ventral cells directly in the live 8-cell frog embryo by microprobe single-cell CE-ESI-MS. *Analytical Methods* **2017,** *9* (34), 4964-4970.
75. Gulersonmez, M. C.; Lock, S.; Hankemeier, T.; Ramautar, R., Sheathless capillary electrophoresis-mass spectrometry for anionic metabolic profiling. *Electrophoresis* **2016,** *37* (7-8), 1007-14.

76. Nemes, P.; Knolhoff, A. M.; Rubakhin, S. S.; Sweedler, J. V., Single-cell metabolomics: Changes in the metabolome of freshly isolated and cultured neurons. *ACS Chemical Neuroscience* **2012,** *3* (10), 782-792.
77. Jeanne Dit Fouque, K.; Garabedian, A.; Porter, J.; Baird, M.; Pang, X.; Williams, T. D.; Li, L.; Shvartsburg, A.; Fernandez-Lima, F., Fast and effective ion mobility-mass spectrometry separation of d-amino-acid-containing peptides. *Anal Chem* **2017,** *89* (21), 11787-11794.
78. Buchberger, A.; Yu, Q.; Li, L., Advances in mass spectrometric tools for probing neuropeptides. *Annual review of analytical chemistry (Palo Alto, Calif.)* **2015,** *8*, 485-509.
79. Neupert, S.; Rubakhin, S. S.; Sweedler, J. V., Targeted single-cell microchemical analysis: MS-based peptidomics of individual paraformaldehyde-fixed and immunolabeled neurons. *Chem Biol* **2012,** *19* (8), 1010-1019.
80. Dale, L.; Slack, J. M., Fate map for the 32-cell stage of *Xenopus laevis*. *Development (Cambridge, England)* **1987,** *99* (4), 527-51.
81. Heyland, A.; Vue, Z.; Voolstra, C. R.; Medina, M.; Moroz, L. L., Developmental transcriptome of *Aplysia californica*. *Journal of Experimental Zoology Part B: Molecular and Developmental Evolution* **2011,** *316B* (2), 113-134.
82. McCoy, J. P., Jr., Basic principles of flow cytometry. *Hematology/oncology clinics of North America* **2002,** *16* (2), 229-43.
83. Ibrahim, S. F.; van den Engh, G., High-speed cell sorting: fundamentals and recent advances. *Current opinion in biotechnology* **2003,** *14* (1), 5-12.
84. Makker, K.; Agarwal, A.; Sharma, R. K., Magnetic activated cell sorting (MACS): utility in assisted reproduction. *Indian journal of experimental biology* **2008,** *46* (7), 491-7.
85. Shields, C. W. t.; Reyes, C. D.; Lopez, G. P., Microfluidic cell sorting: a review of the advances in the separation of cells from debulking to rare cell isolation. *Lab on a chip* **2015,** *15* (5), 1230-49.
86. Lo, S.-J.; Yao, D.-J., Get to understand more from single-cells: current studies of microfluidic-based techniques for single-cell analysis. *International Journal of Molecular Sciences* **2015,** *16* (8), 16763-16777.
87. Wen, N.; Zhao, Z.; Fan, B.; Chen, D.; Men, D.; Wang, J.; Chen, J., Development of droplet microfluidics enabling high-throughput single-cell analysis. *Molecules* **2016,** *21* (7), 881.
88. Cecala, C.; Sweedler, J. V., Sampling techniques for single-cell electrophoresis. *Analyst* **2012,** *137* (13), 2922-2929.
89. Portero, E. P.; Onjiko, R. M.; Moody, S. A.; Nemes, P. In *Discovery Single-cell Mass Spectrometry Profiles Metabolic Gradients in the 16-cell Vertebrate (Frog) Embryo* 65th American Society for Mas Spectrometry Conference on Mass Spectrometry and Allied Topics Indianapolis, IN June; Indianapolis, IN 2017.
90. Lombard-Banek, C.; Reddy, S.; Moody, S. A.; Nemes, P., Label-free quantification of proteins in single embryonic cells with neural fate in the cleavage-stage frog (*Xenopus laevis*) embryo using capillary electrophoresis electrospray ionization high-resolution mass spectrometry (CE-ESI-HRMS). *Mol Cell Proteomics* **2016,** *15* (8), 2756-2768.

91. Hu, P.; Zhang, W.; Xin, H.; Deng, G., Single cell isolation and analysis. *Frontiers in cell and developmental biology* **2016,** *4*, 116.
92. Grant, P. A.; Herold, M. B.; Moody, S. A., Blastomere explants to test for cell fate commitment during embryonic development. *Journal of Visualized Experiments* **2013,** (71), 4458.
93. Nakashima, T.; Wada, H.; Morita, S.; Erra-Balsells, R.; Hiraoka, K.; Nonami, H., Single-cell metabolite profiling of stalk and glandular cells of intact trichomes with internal electrode capillary pressure probe electrospray ionization mass spectrometry. *Analytical Chemistry* **2016,** *88* (6), 3049-3057.
94. Saha-Shah, A.; Green, C. M.; Abraham, D. H.; Baker, L. A., Segmented flow sampling with push-pull theta pipettes. *Analyst* **2016,** *141* (6), 1958-65.
95. Guillaume-Gentil, O.; Rey, T.; Kiefer, P.; Ibanez, A. J.; Steinhoff, R.; Bronnimann, R.; Dorwling-Carter, L.; Zambelli, T.; Zenobi, R.; Vorholt, J. A., Single-eell mass spectrometry of metabolites extracted from live cells by fluidic force microscopy. *Anal Chem* **2017,** *89* (9), 5017-5023.
96. Kummari, E.; Guo-Ross, S.; Eells, J., Laser capture microdissection - A demonstration of the isolation of individual dopamine neurons and the entire ventral tegmental area. *Journal of Visualized Experiments* **2015,** *96*.
97. Chen, M.-m.; Li, A.-l.; Sun, M.-c.; Feng, Z.; Meng, X.-c.; Wang, Y., Optimization of the quenching method for metabolomics analysis of *Lactobacillus bulgaricus*. *J Zhejiang Univ Sci B* **2014,** *15* (4), 333-342.
98. Faijes, M.; Mars, A. E.; Smid, E. J., Comparison of quenching and extraction methodologies for metabolome analysis of *Lactobacillus plantarum*. *Microbial cell factories* **2007,** *6*, 27.
99. Canelas, A. B.; Ras, C.; ten Pierick, A.; van Dam, J. C.; Heijnen, J. J.; van Gulik, W. M., Leakage-free rapid quenching technique for yeast metabolomics. *Metabolomics* **2008,** *4* (3), 226-239.
100. Nemes, P.; Rubakhin, S. S.; Aerts, J. T.; Sweedler, J. V., Qualitative and quantitative metabolomic investigation of single neurons by capillary electrophoresis electrospray ionization mass spectrometry. *Nature protocols* **2013,** *8* (4), 783-99.
101. Onjiko, R. M.; Portero, E. P.; Moody, S. A.; Nemes, P., Microprobe capillary electrophoresis mass spectrometry for single-cell metabolomics in live frog (*Xenopus laevis*) embryos. *Journal of Visualized Experiments* **2017,** (130).
102. Krenkova, J.; Foret, F., On-line CE/ESI/MS interfacing: Recent developments and applications in proteomics. *PROTEOMICS* **2012,** *12* (19-20), 2978-2990.
103. Zhang, W.; Hankemeier, T.; Ramautar, R., Next-generation capillary electrophoresis-mass spectrometry approaches in metabolomics. *Current opinion in biotechnology* **2017,** *43*, 1-7.
104. Zhong, X.; Zhang, Z.; Jiang, S.; Li, L., Recent advances in coupling capillary electrophoresis-based separation techniques to ESI and MALDI-MS. *Electrophoresis* **2014,** *35* (9), 1214-1225.
105. Smith, R. D.; Olivares, J. A.; Nguyen, N. T.; Udseth, H. R., Capillary zone electrophoresis-mass spectrometry using an electrospray ionization interface. *Analytical Chemistry* **1988,** *60* (5), 436-441.

106. Nemes, P.; Marginean, I.; Vertes, A., Spraying mode effect on droplet formation and ion chemistry in electrosprays. *Analytical Chemistry* **2007,** *79* (8), 3105-3116.
107. Choi, S. B.; Zamarbide, M.; Manzini, M. C.; Nemes, P., Tapered-tip capillary electrophoresis nano-electrospray ionization mass spectrometry for ultrasensitive proteomics: the mouse cortex. *Journal of the American Society for Mass Spectrometry* **2017,** *28* (4), 597-607.
108. Sun, L.; Zhu, G.; Zhao, Y.; Yan, X.; Mou, S.; Dovichi, N. J., Ultrasensitive and fast bottom-up analysis of femtogram amounts of complex proteome digests. *Angewandte Chemie (International ed. in English)* **2013,** *52* (51), 13661-4.
109. Whitt, J. T.; Moini, M., Capillary electrophoresis to mass spectrometry interface using a porous junction. *Analytical Chemistry* **2003,** *75* (9), 2188-2191.
110. Grundmann, M.; Matysik, F.-M., Analyzing small samples with high efficiency: capillary batch injection–capillary electrophoresis–mass spectrometry. *Analytical and Bioanalytical Chemistry* **2012,** *404* (6), 1713-1721.
111. Šlampová, A.; Malá, Z.; Gebauer, P.; Boček, P., Recent progress of sample stacking in capillary electrophoresis (2014–2016). *Electrophoresis* **2017,** *38* (1), 20-32.
112. Liu, J.-X.; Aerts, J. T.; Rubakhin, S. S.; Zhang, X.-X.; Sweedler, J. V., Analysis of endogenous nucleotides by single cell capillary electrophoresis-mass spectrometry. *Analyst* **2014,** *139* (22), 5835-5842.
113. Kuehnbaum, N. L.; Kormendi, A.; Britz-McKibbin, P., Multisegment injection-capillary electrophoresis-mass spectrometry: a high-throughput platform for metabolomics with high data fidelity. *Anal Chem* **2013,** *85* (22), 10664-9.
114. Barbula, G. K.; Safi, S.; Chingin, K.; Perry, R. H.; Zare, R. N., Interfacing capillary-based separations to mass spectrometry using desorption electrospray ionization. *Analytical chemistry* **2011,** *83* (6), 1955-1959.
115. Jansson, E. T.; Comi, T. J.; Rubakhin, S. S.; Sweedler, J. V., Single cell peptide heterogeneity of rat islets of *Langerhans*. *ACS Chemical Biology* **2016,** *11* (9), 2588-2595.
116. Smith, C. A.; O'Maille, G.; Want, E. J.; Qin, C.; Trauger, S. A.; Brandon, T. R.; Custodio, D. E.; Abagyan, R.; Siuzdak, G., METLIN: a metabolite mass spectral database. *Therapeutic drug monitoring* **2005,** *27* (6), 747-51.
117. Tautenhahn, R.; Patti, G. J.; Rinehart, D.; Siuzdak, G., XCMS Online: a web-based platform to process untargeted metabolomic data. *Analytical chemistry* **2012,** *84* (11), 5035-5039.
118. Lommen, A., MetAlign: Interface-driven, versatile metabolomics tool for hyphenated full-scan mass spectrometry data preprocessing. *Analytical Chemistry* **2009,** *81* (8), 3079-3086.
119. Tsugawa, H.; Cajka, T.; Kind, T.; Ma, Y.; Higgins, B.; Ikeda, K.; Kanazawa, M.; VanderGheynst, J.; Fiehn, O.; Arita, M., MS-DIAL: data-independent MS/MS deconvolution for comprehensive metabolome analysis. *Nature methods* **2015,** *12* (6), 523-6.

120. Chong, J.; Soufan, O.; Li, C.; Caraus, I.; Li, S.; Bourque, G.; Wishart, D. S.; Xia, J., MetaboAnalyst 4.0: towards more transparent and integrative metabolomics analysis. *Nucleic acids research* **2018,** *46* (W1), W486-W494.
121. Katajamaa, M.; Miettinen, J.; Oresic, M., MZmine: toolbox for processing and visualization of mass spectrometry based molecular profile data. *Bioinformatics (Oxford, England)* **2006,** *22* (5), 634-6.
122. Wang, M.; Carver, J. J.; Phelan, V. V.; Sanchez, L. M.; Garg, N.; Peng, Y.; Nguyen, D. D.; Watrous, J.; Kapono, C. A.; Luzzatto-Knaan, T.; Porto, C.; Bouslimani, A.; Melnik, A. V.; Meehan, M. J.; Liu, W. T.; Crusemann, M.; Boudreau, P. D.; Esquenazi, E.; Sandoval-Calderon, M.; Kersten, R. D.; Pace, L. A.; Quinn, R. A.; Duncan, K. R.; Hsu, C. C.; Floros, D. J.; Gavilan, R. G.; Kleigrewe, K.; Northen, T.; Dutton, R. J.; Parrot, D.; Carlson, E. E.; Aigle, B.; Michelsen, C. F.; Jelsbak, L.; Sohlenkamp, C.; Pevzner, P.; Edlund, A.; McLean, J.; Piel, J.; Murphy, B. T.; Gerwick, L.; Liaw, C. C.; Yang, Y. L.; Humpf, H. U.; Maansson, M.; Keyzers, R. A.; Sims, A. C.; Johnson, A. R.; Sidebottom, A. M.; Sedio, B. E.; Klitgaard, A.; Larson, C. B.; P, C. A. B.; Torres-Mendoza, D.; Gonzalez, D. J.; Silva, D. B.; Marques, L. M.; Demarque, D. P.; Pociute, E.; O'Neill, E. C.; Briand, E.; Helfrich, E. J. N.; Granatosky, E. A.; Glukhov, E.; Ryffel, F.; Houson, H.; Mohimani, H.; Kharbush, J. J.; Zeng, Y.; Vorholt, J. A.; Kurita, K. L.; Charusanti, P.; McPhail, K. L.; Nielsen, K. F.; Vuong, L.; Elfeki, M.; Traxler, M. F.; Engene, N.; Koyama, N.; Vining, O. B.; Baric, R.; Silva, R. R.; Mascuch, S. J.; Tomasi, S.; Jenkins, S.; Macherla, V.; Hoffman, T.; Agarwal, V.; Williams, P. G.; Dai, J.; Neupane, R.; Gurr, J.; Rodriguez, A. M. C.; Lamsa, A.; Zhang, C.; Dorrestein, K.; Duggan, B. M.; Almaliti, J.; Allard, P. M.; Phapale, P.; Nothias, L. F.; Alexandrov, T.; Litaudon, M.; Wolfender, J. L.; Kyle, J. E.; Metz, T. O.; Peryea, T.; Nguyen, D. T.; VanLeer, D.; Shinn, P.; Jadhav, A.; Muller, R.; Waters, K. M.; Shi, W.; Liu, X.; Zhang, L.; Knight, R.; Jensen, P. R.; Palsson, B. O.; Pogliano, K.; Linington, R. G.; Gutierrez, M.; Lopes, N. P.; Gerwick, W. H.; Moore, B. S.; Dorrestein, P. C.; Bandeira, N., Sharing and community curation of mass spectrometry data with global natural products social molecular networking. *Nature biotechnology* **2016,** *34* (8), 828-837.
123. Romanova, E. V.; Aerts, J. T.; Croushore, C. A.; Sweedler, J. V., Small-volume analysis of cell-cell signaling molecules in the brain. *Neuropsychopharmacology : official publication of the American College of Neuropsychopharmacology* **2014,** *39* (1), 50-64.
124. Mellors, J. S.; Jorabchi, K.; Smith, L. M.; Ramsey, J. M., Integrated microfluidic device for automated single cell analysis using electrophoretic separation and electrospray ionization mass spectrometry. *Analytical chemistry* **2010,** *82* (3), 967-973.
125. Li, X.; Zhao, S.; Hu, H.; Liu, Y.-M., A microchip electrophoresis-mass spectrometric platform with double cell lysis nano-electrodes for automated single cell analysis. *Journal of Chromatography A* **2016,** *1451*, 156-163.

126. Sive, H. L.; Grainger, R. M.; Harland, R. M., *Early development of Xenopus laevis: a laboratory manual*. Cold Spring Harbor Laboratory Press: Cold Spring Harbor, N.Y., 2000; p ix, 338 p.
127. Ramautar, R.; Somsen, G. W.; de Jong, G. J., CE-MS for metabolomics: Developments and applications in the period 2010-2012. *Electrophoresis* **2013,** *34* (1), 86-98.
128. Ramautar, R.; Somsen, G. W.; de Jong, G. J., CE-MS for metabolomics: Developments and applications in the period 2014-2016. *Electrophoresis* **2017,** *38* (1), 190-202.
129. Ramautar, R.; Somsen, G. W.; de Jong, G. J., CE-MS for metabolomics: Developments and applications in the period 2012–2014. *Electrophoresis* **2015,** *36* (1), 212-224.
130. Voeten, R. L. C.; Ventouri, I. K.; Haselberg, R.; Somsen, G. W., Capillary electrophoresis: Trends and recent advances. *Anal Chem* **2018,** *90* (3), 1464-1481.
131. Soga, T.; Igarashi, K.; Ito, C.; Mizobuchi, K.; Zimmermann, H. P.; Tomita, M., Metabolomic profiling of anionic metabolites by capillary electrophoresis mass spectrometry. *Anal Chem* **2009,** *81* (15), 6165-74.
132. Lin, L.; Liu, X.; Zhang, F.; Chi, L.; Amster, I. J.; Leach, F. E., 3rd; Xia, Q.; Linhardt, R. J., Analysis of heparin oligosaccharides by capillary electrophoresis-negative-ion electrospray ionization mass spectrometry. *Anal Bioanal Chem* **2017,** *409* (2), 411-420.
133. Moody, S. A., Cell lineage analysis in *Xenopus* embryos. *Methods in Molecular Biology* **2000,** *135*, 331-47.
134. Klein, S. L., The 1st cleavage furrow demarcates the dorsal ventral axis in *Xenopus* embryos. *Dev Biol* **1987,** *120* (1), 299-304.
135. Moody, S. A.; Kline, M. J., Segregation of fate during cleavage of frog (*Xenopus laevis*) blastomeres. *Anatomy and Embryology* **1990,** *182* (4), 347-62.
136. Straub, R. F.; Voyksner, R. D., Negative ion formation in electrospray mass spectrometry. *Journal of the American Society for Mass Spectrometry* **1993,** *4* (7), 578-587.
137. Ikonomou, M. G.; Blades, A. T.; Kebarle, P., Electrospray mass spectrometry of methanol and water solutions suppression of electric discharge with SF6 gas. *Journal of the American Society for Mass Spectrometry* **1991,** *2* (6), 497-505.
138. Cole, R. B.; Harrata, A. K., Solvent effect on analyte charge state, signal intensity, and stability in negative ion electrospray mass spectrometry; implications for the mechanism of negative ion formation. *Journal of the American Society for Mass Spectrometry* **1993,** *4* (7), 546-556.
139. McClory, P. J.; Hakansson, K., Corona discharge suppression in negative ion mode nanoelectrospray ionization via trifluoroethanol addition. *Anal Chem* **2017,** *89* (19), 10188-10193.
140. Wu, Z.; Gao, W.; Phelps, M. A.; Wu, D.; Miller, D. D.; Dalton, J. T., Favorable effects of weak acids on negative-ion electrospray ionization mass spectrometry. *Anal Chem* **2004,** *76* (3), 839-47.

141. Knolhoff, A. M.; Nautiyal, K. M.; Nemes, P.; Kalachikov, S.; Morozova, I.; Silver, R.; Sweedler, J. V., Combining small-volume metabolomic and transcriptomic approaches for assessing brain chemistry. *Analytical chemistry* **2013,** *85* (6), 3136-3143.
142. Marginean, I.; Nemes, P.; Vertes, A., Astable regime in electrosprays. *Physical Review E* **2007,** *76* (2), 026320.
143. Wang, D.; Bodovitz, S., Single cell analysis: the new frontier in 'omics'. *Trends in biotechnology* **2010,** *28* (6), 281-90.
144. Yanes, O.; Clark, J.; Wong, D. M.; Patti, G. J.; Sanchez-Ruiz, A.; Benton, H. P.; Trauger, S. A.; Desponts, C.; Ding, S.; Siuzdak, G., Metabolic oxidation regulates embryonic stem cell differentiation. *Nature chemical biology* **2010,** *6* (6), 411-7.
145. Moussaieff, A.; Rouleau, M.; Kitsberg, D.; Cohen, M.; Levy, G.; Barasch, D.; Nemirovski, A.; Shen-Orr, S.; Laevsky, I.; Amit, M.; Bomze, D.; Elena-Herrmann, B.; Scherf, T.; Nissim-Rafinia, M.; Kempa, S.; Itskovitz-Eldor, J.; Meshorer, E.; Aberdam, D.; Nahmias, Y., Glycolysis-mediated changes in acetyl-CoA and histone acetylation control the early differentiation of embryonic stem cells. *Cell metabolism* **2015,** *21* (3), 392-402.
146. Folmes, C. D. L.; Dzeja, P. P.; Nelson, T. J.; Terzic, A., Metabolic plasticity in stem cell homeostasis and differentiation. *Cell Stem Cell* **2012,** *11* (5), 596-606.
147. Liu, B.; Winkler, F.; Herde, M.; Witte, C.-P.; Großhans, J., A link between deoxyribonucleotide metabolites and embryonic cell-cycle control. *Current Biology* **2019,** *29* (7), 1187-1192.e3.
148. Massé, K.; Dale, N., Purines as potential morphogens during embryonic development. *Purinergic Signal* **2012,** *8* (3), 503-521.
149. O'Brien, P. J.; Lee, M.; Spilker, M. E.; Zhang, C. C.; Yan, Z.; Nichols, T. C.; Li, W.; Johnson, C. H.; Patti, G. J.; Siuzdak, G., Monitoring metabolic responses to chemotherapy in single cells and tumors using nanostructure-initiator mass spectrometry (NIMS) imaging. *Cancer Metab* **2013,** *1* (1), 4.
150. Duncan, K. D.; Fyrestam, J.; Lanekoff, I., Advances in mass spectrometry based single-cell metabolomics. *Analyst* **2019,** *144* (3), 782-793.
151. Chokkathukalam, A.; Kim, D. H.; Barrett, M. P.; Breitling, R.; Creek, D. J., Stable isotope-labeling studies in metabolomics: new insights into structure and dynamics of metabolic networks. *Bioanalysis* **2014,** *6* (4), 511-24.
152. Klein, S.; Heinzle, E., Isotope labeling experiments in metabolomics and fluxomics. *Wiley interdisciplinary reviews. Systems biology and medicine* **2012,** *4* (3), 261-72.
153. Jang, C.; Chen, L.; Rabinowitz, J. D., Metabolomics and isotope tracing. *Cell* **2018,** *173* (4), 822-837.
154. Sowers, M. L.; Herring, J.; Zhang, W.; Tang, H.; Ou, Y.; Gu, W.; Zhang, K., Analysis of glucose-derived amino acids involved in one-carbon and cancer metabolism by stable-isotope tracing gas chromatography mass spectrometry. *Analytical biochemistry* **2019,** *566*, 1-9.

155. Date, Y.; Nakanishi, Y.; Fukuda, S.; Kato, T.; Tsuneda, S.; Ohno, H.; Kikuchi, J., New monitoring approach for metabolic dynamics in microbial ecosystems using stable-isotope-labeling technologies. *Journal of bioscience and bioengineering* **2010,** *110* (1), 87-93.
156. Nieuwkoop, P. D.; Faber, J., Normal table of *Xenopus laevis*: A systematical and chronological survey of the development from the fertilized egg till the end of metamorphosis. **1994**.
157. Moody, S. A., Microinjection of mRNAs and oligonucleotides. *Cold Spring Harbor protocols* **2018,** *2018* (12).
158. Kanehisa, M.; Furumichi, M.; Tanabe, M.; Sato, Y.; Morishima, K., KEGG: new perspectives on genomes, pathways, diseases and drugs. *Nucleic acids research* **2017,** *45* (D1), D353-d361.
159. Hackett, S. R.; Zanotelli, V. R.; Xu, W.; Goya, J.; Park, J. O.; Perlman, D. H.; Gibney, P. A.; Botstein, D.; Storey, J. D.; Rabinowitz, J. D., Systems-level analysis of mechanisms regulating yeast metabolic flux. *Science* **2016,** *354* (6311).
160. Park, J. O.; Rubin, S. A.; Xu, Y. F.; Amador-Noguez, D.; Fan, J.; Shlomi, T.; Rabinowitz, J. D., Metabolite concentrations, fluxes and free energies imply efficient enzyme usage. *Nature chemical biology* **2016,** *12* (7), 482-9.
161. Karimi, K.; Fortriede, J. D.; Lotay, V. S.; Burns, K. A.; Wang, D. Z.; Fisher, M. E.; Pells, T. J.; James-Zorn, C.; Wang, Y.; Ponferrada, V. G.; Chu, S.; Chaturvedi, P.; Zorn, A. M.; Vize, P. D., Xenbase: a genomic, epigenomic and transcriptomic model organism database. *Nucleic acids research* **2018,** *46* (D1), D861-d868.
162. Masui, Y.; Wang, P., Cell cycle transition in early embryonic development of *Xenopus laevis*. *Biology of the cell* **1998,** *90* (8), 537-48.
163. Zhang, S.; Zeng, X.; Ren, M.; Mao, X.; Qiao, S., Novel metabolic and physiological functions of branched chain amino acids: a review. *Journal of animal science and biotechnology* **2017,** *8*, 10.
164. Laplante, M.; Sabatini, D. M., mTOR signaling at a glance. *Journal of Cell Science* **2009,** *122* (20), 3589-3594.
165. Meng, D.; Frank, A. R.; Jewell, J. L., mTOR signaling in stem and progenitor cells. *Development (Cambridge, England)* **2018,** *145* (1).
166. Kim, J.; Kim, E., Rag GTPase in amino acid signaling. *Amino acids* **2016,** *48* (4), 915-928.
167. Pan, N.; Rao, W.; Kothapalli, N. R.; Liu, R.; Burgett, A. W. G.; Yang, Z., The single-probe: A miniaturized multifunctional device for single cell mass spectrometry analysis. *Analytical Chemistry* **2014,** *86* (19), 9376-9380.
168. Mizuno, H.; Tsuyama, N.; Harada, T.; Masujima, T., Live single-cell video-mass spectrometry for cellular and subcellular molecular detection and cell classification. *Journal of Mass Spectrometry* **2008,** *43* (12), 1692-1700.
169. Krejci, A.; Tennessen, J. M., Metabolism in time and space – exploring the frontier of developmental biology. *Development (Cambridge, England)* **2017,** *144* (18), 3193-3198.

170. Levin, M.; Mercola, M., Gap junction-mediated transfer of left-right patterning signals in the early chick blastoderm is upstream of Shh asymmetry in the node. *Development (Cambridge, England)* **1999,** *126* (21), 4703-14.
171. Goldberg, G. S.; Lampe, P. D.; Nicholson, B. J., Selective transfer of endogenous metabolites through gap junctions composed of different connexins. *Nature Cell Biology* **1999,** *1* (7), 457-459.
172. Levin, M., Gap junctional communication in morphogenesis. *Progress in biophysics and molecular biology* **2007,** *94* (1-2), 186-206.
173. Landesman, Y.; Postma, F. R.; Goodenough, D. A.; Paul, D. L., Multiple connexins contribute to intercellular communication in the *Xenopus* embryo. *Journal of Cell Science* **2003,** *116* (1), 29.
174. Rigbolt, K. T.; Vanselow, J. T.; Blagoev, B., GProX, a user-friendly platform for bioinformatics analysis and visualization of quantitative proteomics data. *Mol Cell Proteomics* **2011,** *10* (8), O110.007450.
175. Viczian, A. S.; Zuber, M. E., A simple behavioral assay for testing visual function in *Xenopus laevis*. *JoVE* **2014,** (88), e51726.
176. Goodenough, D. A.; Paul, D. L., Gap junctions. *Cold Spring Harbor perspectives in biology* **2009,** *1* (1), a002576.
177. Guthrie, S. C., Patterns of junctional communication in the early amphibian embryo. *Nature* **1984,** *311* (5982), 149-151.
178. Guthrie, S. C.; Gilula, N. B., Gap junctional communication and development. *Trends in neurosciences* **1989,** *12* (1), 12-6.
179. Levin, M.; Mercola, M., Gap junctions are involved in the early generation of left-right asymmetry. *Dev Biol* **1998,** *203* (1), 90-105.
180. Connors, B. W., Tales of a dirty drug: carbenoxolone, gap junctions, and seizures. *Epilepsy Curr* **2012,** *12* (2), 66-68.
181. Ubeda, A.; Trillo, M. A.; House, D. E.; Blackman, C. F., Melatonin enhances junctional transfer in normal C3H/10T1/2 cells. *Cancer Letters* **1995,** *91* (2), 241-245.
182. Warner, A., Gap junctions in development-a perspective. *Seminars in cell biology* **1992,** *3* (1), 81-91.
183. Viczian, A. S.; Solessio, E. C.; Lyou, Y.; Zuber, M. E., Generation of functional eyes from pluripotent cells. *PLoS biology* **2009,** *7* (8), e1000174.
184. Ibáñez, A. J.; Fagerer, S. R.; Schmidt, A. M.; Urban, P. L.; Jefimovs, K.; Geiger, P.; Dechant, R.; Heinemann, M.; Zenobi, R., Mass spectrometry-based metabolomics of single yeast cells. *Proceedings of the National Academy of Sciences* **2013,** *110* (22), 8790.
185. Shrestha, B.; Patt, J. M.; Vertes, A., In situ cell-by-cell imaging and analysis of small cell populations by mass spectrometry. *Anal Chem* **2011,** *83* (8), 2947-55.
186. Hirayama, A.; Abe, H.; Yamaguchi, N.; Tabata, S.; Tomita, M.; Soga, T., Development of a sheathless CE-ESI-MS interface. *Electrophoresis* **2018,** *39* (11), 1382-1389.
187. Cahill, J. F.; Riba, J.; Kertesz, V., Rapid, untargeted chemical profiling of single cells in their native environment. *Analytical Chemistry* **2019,** *91* (9), 6118-6126.

188. Zhang, X.-C.; Wei, Z.-W.; Gong, X.-Y.; Si, X.-Y.; Zhao, Y.-Y.; Yang, C.-D.; Zhang, S.-C.; Zhang, X.-R., Integrated droplet-based microextraction with ESI-MS for removal of matrix interference in single-cell analysis. *Scientific Reports* **2016,** *6* (1), 24730.
189. Joensson, H. N.; Andersson Svahn, H., Droplet microfluidics—A tool for single-cell analysis. *Angewandte Chemie International Edition* **2012,** *51* (49), 12176-12192.
190. Chen, Q.; Wu, J.; Zhang, Y.; Lin, J.-M., Qualitative and quantitative analysis of tumor cell metabolism via stable isotope labeling assisted microfluidic chip electrospray ionization mass spectrometry. *Analytical Chemistry* **2012,** *84* (3), 1695-1701.
191. Liu, Z.; Portero, E. P.; Jian, Y.; Zhao, Y.; Onjiko, R. M.; Zeng, C.; Nemes, P., Trace, machine learning of signal images for trace-sensitive mass spectrometry: A case study from single-cell metabolomics. *Analytical Chemistry* **2019,** *91* (9), 5768-5776.
192. González-Ruiz, V.; Gagnebin, Y.; Drouin, N.; Codesido, S.; Rudaz, S.; Schappler, J., ROMANCE: A new software tool to improve data robustness and feature identification in CE-MS metabolomics. *Electrophoresis* **2018,** *39* (9-10), 1222-1232.
193. Drouin, N.; van Mever, M.; Zhang, W.; Tobolkina, E.; Ferre, S.; Servais, A.-C.; Gou, M.-J.; Nyssen, L.; Fillet, M.; Lageveen-Kammeijer, G. S. M.; Nouta, J.; Chetwynd, A. J.; Lynch, I.; Thorn, J. A.; Meixner, J.; Lößner, C.; Taverna, M.; Liu, S.; Tran, N. T.; Francois, Y.; Lechner, A.; Nehmé, R.; Al Hamoui Dit Banni, G.; Nasreddine, R.; Colas, C.; Lindner, H. H.; Faserl, K.; Neusüß, C.; Nelke, M.; Lämmerer, S.; Perrin, C.; Bich-Muracciole, C.; Barbas, C.; Gonzálvez, Á. L.; Guttman, A.; Szigeti, M.; Britz-McKibbin, P.; Kroezen, Z.; Shanmuganathan, M.; Nemes, P.; Portero, E. P.; Hankemeier, T.; Codesido, S.; González-Ruiz, V.; Rudaz, S.; Ramautar, R., Capillary electrophoresis-mass spectrometry at trial by Metabo-ring: effective electrophoretic mobility for reproducible and robust compound annotation. *Analytical Chemistry* **2020,** 92, 14103-14112.